Switching Dynamics in Ferroelectric $Hf_{0.5}Zr_{0.5}O_2$ Devices: Experiments and Models

by

Taekyong Kim

B.S., Hanyang University (2011)
S.M., Korea Advanced Institute of Science and Technology (2013)

Submitted to the Department of Electrical Engineering and Computer Science
in partial fulfillment of the requirements for the degree of

Doctor of Philosophy
at the
Massachusetts Institute of Technology

September 2023

Authored by: Taekyong Kim
Department of Electrical Engineering and Computer Science
August 21, 2023

Certified by: Jesús A. del Alamo
Professor of Electrical Engineering and Computer Science
Thesis Supervisor

Certified by: Dimitri A. Antoniadis
Professor of Electrical Engineering and Computer Science
Thesis Supervisor

Accepted by: Leslie A. Kolodziejski
Professor of Electrical Engineering and Computer Science
Chair, Department Committee on Graduate Students

To my wife Song-I
and my children Leon and Lumin

Switching Dynamics in Ferroelectric $Hf_{0.5}Zr_{0.5}O_2$ Devices: Experiments and Models

by

Taekyong Kim

Submitted to the Department of Electrical Engineering and Computer Science
on Aug 21, 2023, in Partial Fulfillment of the Requirements for the Degree of
Doctor of Philosophy in Electrical Engineering and Computer Science

ABSTRACT

Ferroelectric $Hf_{0.5}Zr_{0.5}O_2$ (FE-HZO) has breathed new life into the field of ferroelectric research, boasting exceptional physical properties, such as compatibility with existing semiconductor processes, highly scalable thickness, and prominent FE properties. As a result, this intriguing material has gathered extensive attention for applications in ultra-scaled Si MOSFETs, memory devices, energy-efficient hardware for convolutional computation, and RF devices. However, despite intense research, there is still controversy about the FE switching dynamics, a crucial factor in designing ferroelectric device applications.

This thesis pursues fundamental understanding of the switching dynamics in FE-HZO structures founded on accurate dynamic measurements with meticulous experimental design considerations. Towards this, low-parasitic FE-HZO structures have been fabricated and characterized over a broad range of frequencies using large-signal and small-signal analysis. In large-signal analysis, a Finite-Difference implementation of the Nucleation Limited Switching model (FD-NLS) is introduced, which accurately predicts the FE circuit dynamics across a wide range of time scales. Additionally, a thorough analysis of the imprint effect, a critical reliability issue in FE devices is provided. In small-signal analysis, a physically meaningful small-signal equivalent circuit model is developed that describes impedance measurements well over a full bias range and 7 orders of magnitude of frequency all the way into the GHz regime. Moreover, this work sheds light on the underlying physics of the circuit elements.

The findings in this thesis will contribute to the design and modeling of diverse FE-HZO devices for a wide range of applications, adding valuable knowledge to the field of FE-HZO research.

Thesis Supervisor: Jesús A. del Alamo
Title: Professor of Electrical Engineering and Computer Science
Thesis Supervisor: Dimitri A. Antoniadis
Title: Professor of Electrical Engineering and Computer Science

Acknowledgments

This thesis would not have been possible without the unwavering support and encouragement of numerous individuals.

Above all, I want to express my deepest gratitude to my two exceptional thesis advisors, Prof. Jesús A. del Alamo and Prof. Dimitri A. Antoniadis. Their guidance, expertise, and constant motivation have played a crucial role in shaping my research. Particularly, their patience and enthusiasm for device physics have enabled me to relish every moment of my doctoral study. Their guidance extended to every aspect, encompassing valuable lessons in effective writing and presentation skills, thoroughness and integrity in research, productive project management, and the soft skills and qualities of a great engineer. I am truly fortunate and honored to have had the privilege of being their student. Undoubtedly, I would choose to be their student again if I could go back to the time when I joined MIT.

My gratitude also goes to my thesis committee member, Prof. Akinwande. His valuable insights, critical feedback, and guidance have played an important role in shaping the direction and quality of this research.

I am also thankful for Xtreme Transistor Group members: Prof. Jesús Grajal, Alon Vardi, Wenjie Lu, Xiaowei Cai, Xin Zhao, Aviram Massuda, Ethan Lee, Murat Onen, Yanjie Shao, Jinseok Kim, Noah Kim, Elham Borujeny, and Dean Shen and friends in Bldg 39: Ahmad Zubair, Nadim Chowdhury, Qingyun Xie, Pao-Chuan Shih, Joshua Perozek, John Niroula, Winston Chern, and Andrew Yu, who have shared their insights, engaged in stimulating discussions, and spent great time together.

I extend my appreciation to the dedicated MTL staff: Robert Bicchieri, Kurt Broderick, Donal Jamieson, Eric Lim, Dave Terry, Dennis Ward, Bill Maloney, Mike Hobbs, Elizabeth Kubicki, Elizabeth Green, Jami Mitchell. They always helped me to go through everything related to my research smoothly and made me feel like a family. Fantastic research and a great mood at MTL are possible because of their support and dedication.

I am grateful to my incredible friends who truly enriched my life in Boston, Hanyang Boardgame Group, KGSA Basketball Team, Site 4 Families and EECS students.

I also received invaluable support for this thesis from the fantastic mentors at the SRC companies. I want to express my special gratitude to Gilber Dewey, Uygar E. Avci (at Inter Corp.), and Rebecca Park (at Samsung). Their valuable insights and suggestions motivated and guided me in conducting more sophisticated and refined research.

To my loving wife, Song-I, your unwavering support, patience, and understanding during this journey are deeply appreciated. Also, to my two little shining stars, Leon and Lumin, your smiles always fill me with happiness.

This research was sponsored by Semiconductor Research Corporation and Samsung Electronics.

Contents

List of Figures

List of Tables

Chapter 1 Introduction

1.1 Ferroelectric Materials

Ferroelectric (FE) materials, in addition to electron polarization, exhibit an additional polarization mechanism: FE domain switching polarization that arises from its unique crystallographic structure [1]. This domain switching polarization results in hysteretic charge-voltage characteristics for FE materials, in contrast to linear dielectrics. The presence of FE polarization enables these materials to exhibit a significant amount of non-volatile spontaneous polarization. Fig. 1-1 illustrates the charge-voltage characteristics of a ferroelectric and a linear dielectric. Also, it shows evolution of FE domain switching as a function of applied voltage.

Two essential parameters that represent the FE properties are remanent polarization (P_r) and coercive voltage (V_C). P_r is defined as the non-volatile remanent charge on the metal electrodes when the voltage is zero (V = 0), and V_C corresponds to the voltage at which the charge becomes zero. In general, strong FE properties are accompanied by high P_r and small V_C.

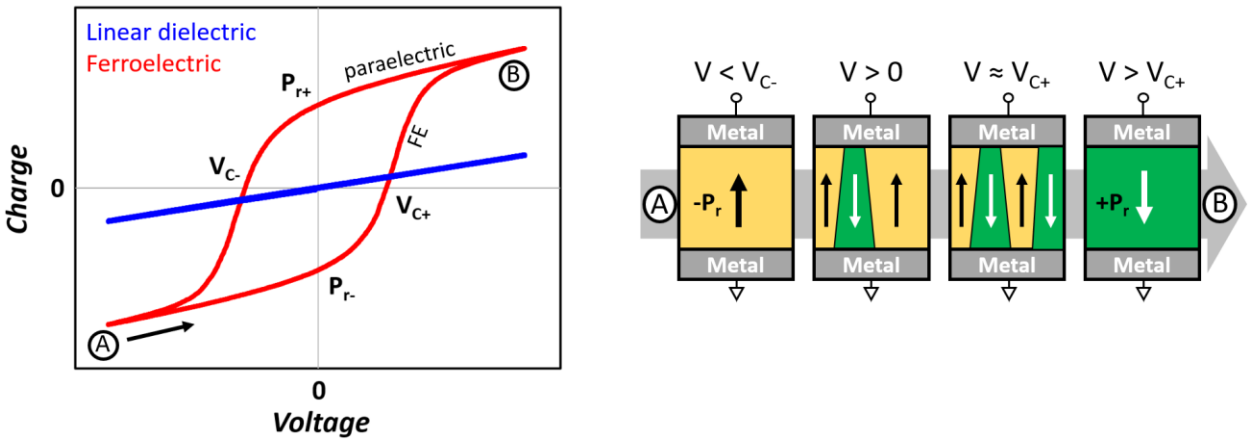

Fig. 1-1. Comparison of Q-V characteristics between linear dielectrics and FE materials (left) and schematic of FE domain switching according to voltage change from A to B (right).

1.2 CMOS-Compatible Ferroelectric $Hf_{0.5}Zr_{0.5}O_2$ (FE-HZO)

Since the first proposal of FE-based semiconductor devices in the 1950s, FE materials have provided immense benefits to modern microelectronics due to the nonvolatile nature of FE polarization switching [2, 3]. However, as devices scaled down, it became difficult to develop new devices with conventional materials, such as $BaTiO_3$ (BTO) and $Pb[Zr_xTi_{1-x}]O_3$ (PZT), due to obstacles in CMOS process incompatibility and thickness scaling. As a result, research on FE devices dwindled until the emergence of ferroelectricity in hafnium oxide thin films in 2011, as shown in Fig. 1-2 [4]. Among various dopants doped HfO_2 films, $Hf_{0.5}Zr_{0.5}O_2$ (HZO) has revitalized the research field with its excellent physical properties, including compatibility with existing semiconductor processes, highly scalable thickness, and prominent FE properties [5]. Consequently, semiconductor devices incorporating FE-HZO have recently attracted enormous interest as a material for ultra-scaled Si MOSFETs [6], memory devices [7, 8], energy-efficient analog computing hardware [9, 10, 11], and even RF devices [12].

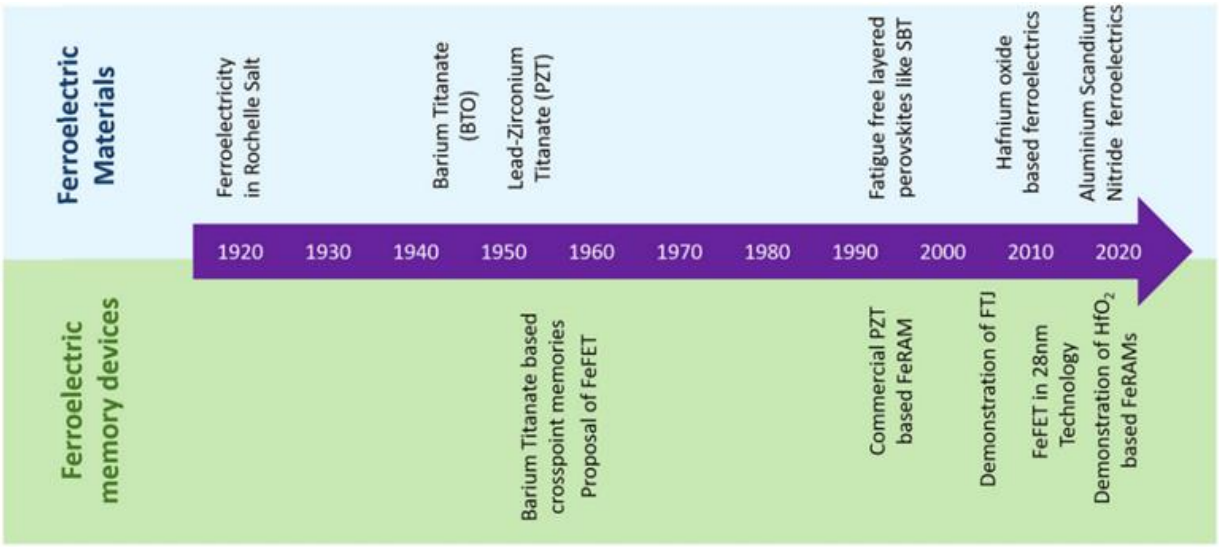

Fig. 1-2. Timeline of FE materials and FE semiconductor devices [13].

Despite extensive research, the understanding of switching dynamics in FE-HZO structures, essential foundation for developing various applications, remains controversial. This is due to the limited understanding of physics that is originated from not only its complex material system but also its polycrystalline and thin film properties, which is distinct from traditional FE materials. Additionally, experimental observations without thorough consideration of the measurement setup can lead to limited or incorrect comprehension of its dynamics. Thus, to resolve this controversy, this thesis demonstrates the characterization and modeling of FE-HZO switching dynamics based on observations from rigorously designed experiments. Notably, our study will also include small-signal analysis, which has not been much explored in contrast to the large-signal dynamic operation.

1.3 FE Polarization Switching Dynamics in Large-Signal Analysis

The process of polarization reversal in FE materials has been extensively studied for decades. It is widely accepted that the kinetics of this process are governed by the nucleation, growth, and coalescence of reversed polarization domains. All models are based on the work of the Ishibashi group [14], which adapted the classical phase-transition theory of Kolmogorov [15] and Avrami [16]. While the resulting K-A-I model was founded on the idea that kinetics are determined by the rate of domain wall propagation, Tagantsev et al. [17] later observed that in polycrystalline film capacitors, which are of particular practical interest here, the limiting mechanism appears to be the rate of nucleation. They proposed the Nucleation-Limited Switching (NLS) model which has been shown to explain most experimental results that explore the switching rate dependence on the magnitude of the applied electric field across the FE film. Fig. 1-3 shows a detailed study from

[18] that suggests that the NLS model provides a better description of polarization switching in a polycrystalline HfO_2 FE oxide thin film.

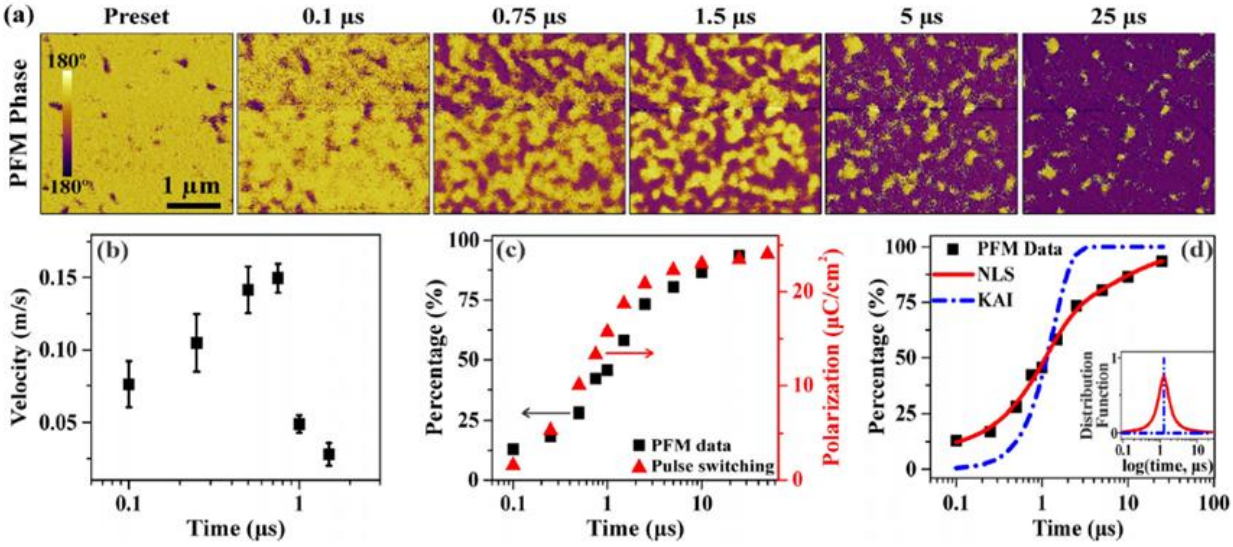

Fig. 1-3. The result shows NLS model works well with polycrystalline La:HfO_2 FE oxide. (a) PFM phase images of instantaneous domain configurations at different polarization reversal under application of 4.0V pulses. (b) Time-dependent variations in domain wall velocity. (c) Comparison of experimental PFM data showing switched capacitor area. (d) Fitting of the piezoresponse force microscopy (PFM) switching data by the KAI and NLS models. [18]

While most publications have presented mathematical solutions of the NLS model that are only applicable to a simple step pulse of the electric field [17, 19, 20, 21], these models are not applicable to arbitrary waveforms of the electric field encountered in realistic circuits under fast dynamics. Recent papers have attempted to address this issue, but they are either mathematically flawed [22, 23] or physically sound but unsuitable for incorporation in circuit simulation due to their use of the Monte Carlo method [24].

Toward practical FE-HZO circuit simulations, the NLS model should be rigorously derived from a basic formulation and must be implemented with the use of efficient numerical solution method.

Thus, this thesis will display the implementation of a mathematically correct NLS model simulation established based on accurately measured data. In terms of the measurements, we will carefully design the experimental work to capture the intrinsic FE switching dynamics which will serve as the basis for the new model.

FE switching dynamics becomes even more complicated when considering the imprint effect, which is a common phenomenon that can change the nucleation rate of polarization reversal depending on the polarization direction, time duration and voltage of the immediately preceding state. From previous publications [25, 26], the imprint effect refers to the nucleation incubation time becoming longer with the time elapsed from the point at which the final polarization is established. This results in a shift of charge-voltage loop, as shown in Fig. 1-4. This can cause the misinterpretation of the stored charge or storing different amount of polarization due to the undesirable change of FE dynamics, which leads to significant drop of device yield in the case of FE-based memory devices. Therefore, the imprint effect is regarded as a major issue for memory operation.

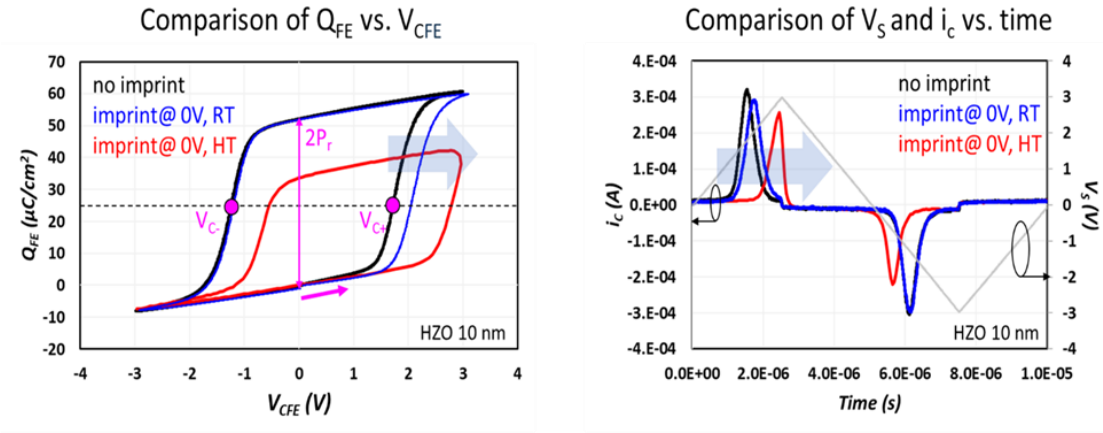

Fig. 1-4. The impact of the imprint effect in FE-HZO on FE switching dynamics. (left) Q_{FE}-V_{CFE} loop changes after 0V imprint at different temperatures and (right) their time-domain current responses. As temperature increases, the imprint effect (loop shift) becomes severe.

Although several studies have investigated the imprint effect of HfO_2-based ferroelectric capacitors, the root cause of imprint is still disputed. The suggested models can be categorized by following three different stimuli of the imprint effect: 1) redistribution of mobile charges [25, 26, 27, 28, 29, 30, 31], 2) defect dipole polarization [32], and 3) charge trapping and de-trapping at a non-FE interfacial layer between oxide and metal [33, 34, 35]. Furthermore, these models have not been quantitatively scrutinized to check their physical validity.

Thus, our work pursues a comprehensive understanding of the imprint effect in FE-HZO structures based on observations from various voltage pulse measurements.

1.4 FE Small-Signal Dynamics

In the small-signal analysis of FE-HZO, the unique hysteretic butterfly-shaped capacitance-voltage (C-V) curve of FE materials is observed from measured impedance (Z) characteristics. However, the Z characteristics has not been explored in the GHz regime, where the butterfly shape may disappear if simply extrapolated from data measured by an LCR meter, as shown in Fig. 1-5.

Although previous reports have investigated this topic in traditional FE materials [36, 37], their results are debatable due to the lack of deliberately designed device structures and accurate de-embedding processes necessary for small-signal analysis in the GHz regime. To address this, a systematic examination of FE-HZO structures over a broad range of frequencies should be implemented involving the following steps:

1) designing a Z-matched coplanar waveguide (CPW) transmission line structure with very low parasitics

2) validating the layout with electromagnetic circuit simulation

3) precisely calibrating all measurement setups

4) implementing an accurate de-embedding process with evaluation of Open, Short and Thru patterns

The small-signal characteristics can be modeled with an equivalent circuit model. Some existing models have been suggested for FE-HZO MFM structures [38, 39]. However, the circuit models rely on the use of a *Constant Phase Element* (CPE) to fit the frequency dependence of measured Z data. While CPE is commonly used in electrochemical impedance analysis, the underlying physics are still unclear. Therefore, it becomes crucial to develop a physically meaningful small-signal equivalent circuit model based on accurately de-embedded data that can faithfully reproduce the FE-HZO properties across the full frequency range.

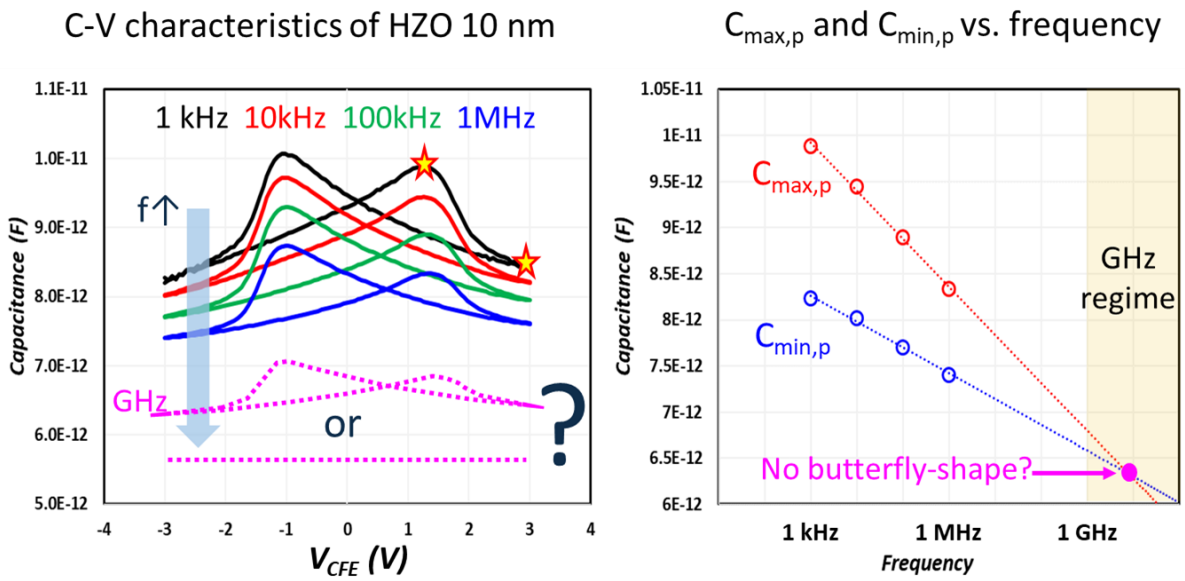

Fig. 1-5. The butterfly-shaped C-V curves at different frequencies (left). No butterfly-shaped C-V curve is expected from the extrapolated estimation (right).

1.5 Thesis Overview

This thesis focuses on developing a fundamental understanding of the switching dynamics in FE-HZO structures. The research is based on accurate dynamic measurements and meticulous experimental design considerations. In the subsequent chapters, we delve into the switching dynamics through both large-signal analysis and small-signal analysis, constructing models that precisely reproduce our measurements.

Before presenting the experimental results, Chapter 2 introduces our low-parasitic samples and thoroughly calibrated setups. This chapter explains the process of designing samples and calibrating all parasitics in the measurement setups to obtain the intrinsic FE dynamics.

In the large-signal analysis, we resolve the ongoing controversy surrounding the existence of negative capacitance (NC) in Resistor-MFM (R-MFM) circuits and demonstrate the intrinsic FE dynamics. Based on these results, we propose a new FE switching model. Additionally, we conduct extensive investigations into the imprint effect, which is one of the most significant degradation effects in FE materials.

Moving on to small-signal analysis, we reveal comprehensive AC impedance measurements of FE-HZO MFM structures across a broad frequency range spanning 7 orders of magnitude. Subsequently, we develop a physically meaningful small-signal equivalent circuit model that accurately describes the data over the entire frequency span and bias range, providing valuable insights into the physics of the circuit elements. Moreover, our research sheds light on the origin of a butterfly-shaped C-V curve.

Through our meticulous experimental approach and thorough analysis, this thesis contributes to the deeper understanding of FE dynamics in HZO structures and lays the groundwork for further advancements in this field.

Chapter 2 FE Device Fabrication and Measurement Setup

The device structure and measurement setup are crucial in extracting the intrinsic FE dynamics of MFM structures. This chapter elucidates the design and fabrication of the FE samples investigated in this work. It also describes the measurement setups used and their calibration.

2.1 Device Fabrication

This section discusses MFM capacitor and FE coplanar waveguide structures used in our experimental study. For large-signal analysis, we fabricated the two types of MFM capacitors depending on the ALD process, with TiN (results discussed in Chapter 3) or W electrodes (results discussed in Chapter 4). Furthermore, we introduce a coplanar waveguide structure as discussed in Chapter 5, which incorporates a W/HZO/W MFM capacitor. This structure enables precise characterization of small-signal measurements within the GHz regime.

2.1.1 Metal-FE-HZO-Metal (MFM) Capacitor

Fig. 2-1 illustrates a cross-sectional schematic of the fabricated TiN/HZO/TiN MFM capacitors on a sapphire substrate, which are examined in Chapter 3. The sapphire wafer is used as a substrate to minimize parasitic effects, and the W layer under the bottom TiN electrode is introduced to decrease the access resistance between the two Au/Ti pads, resulting in a smaller RC time constant. The FE property of the HZO layer is activated by a thermal step with the TiN electrodes in place which can promote a FE orthorhombic phase.

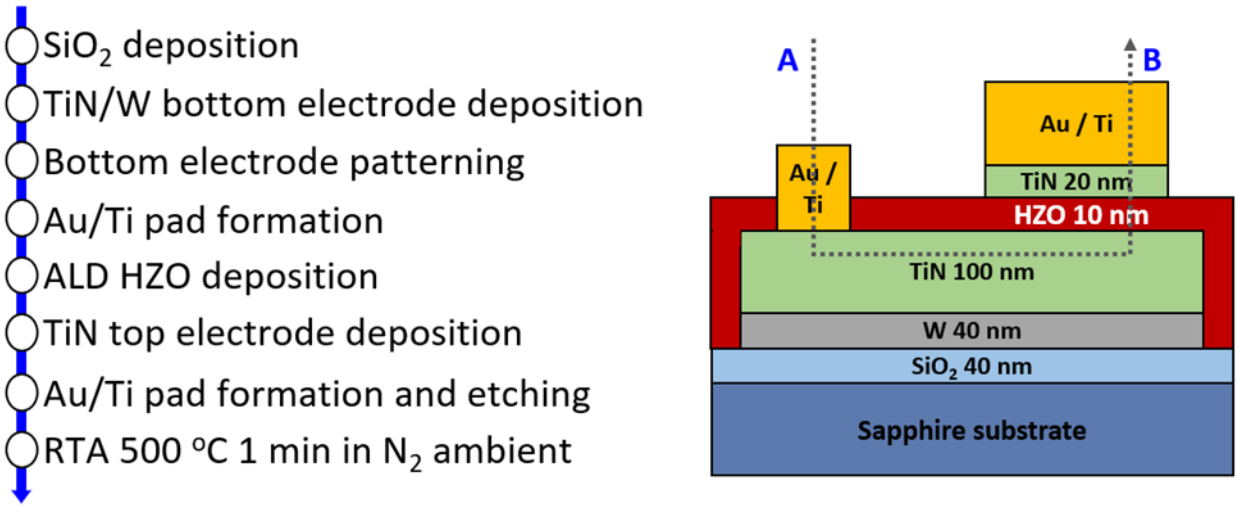

Fig. 2-1. Fabrication process flow and cross-sectional schematic of TiN/HZO/TiN MFM capacitor with low parasitics that incorporates 10-nm FE-HZO. Current flows from A to B during measurements.

The fabrication consists of a three-mask process (Fig. 2-1). A 40-nm SiO_2 film was deposited on a sapphire substrate by plasma-assisted chemical vapor deposition at 300 ℃. Then, 40-nm W followed by 100-nm TiN layers were deposited by sputtering and served as the bottom electrode which was defined in a first lithography step using reactive ion etching (RIE). A Au/Ti pad was formed on top of the bottom electrode by metal evaporation and lift-off. A 10-nm HZO film was subsequently grown by thermal atomic-layer deposition (ALD) at 250 ℃ using tetrakis-ethylmethylamino hafnium (TEMA-Hf) and tetrakis-ethylmethylamino zirconium (TEMA-Zr) as precursors and water vapor as oxidant. During the ALD process, no reaction of precursors occurs on the Au surface, which remains uncovered. After ALD, a 20-nm TiN top electrode was sputtered, and this was followed by lift-off of an evaporated Au/Ti bilayer. The Au/Ti pattern was then used to define the TiN top electrode by RIE. The process was completed with a thermal step performed by rapid thermal annealing (RTA) at 500 ℃ in N_2 ambient for 1 min to activate the FE phase of HZO. Capacitors with active areas between 400 and 40000 μm^2 were fabricated.

In addition to the TiN/HZO/TiN MFM structures, we also fabricated MFM structures with W electrodes, as shown in Fig. 2-2. These structures have smaller active areas, ranging from 20 to 2500 μm^2. The fabrication for the structures consists of a four-mask process. The fabrication starts with sputtering of a 40-nm W film to serve as a bottom electrode, which was defined in a first lithography step using RIE. Then, a Au/Ti pad was formed on top of the bottom electrode through evaporation and lift-off. A 10-nm HZO film was deposited by plasma-enhanced ALD (PE-ALD) at 250 ℃ with inductively coupled plasma of 600 W.[1] Unlike the thermal ALD process described above, tetrakis-dimethylamino hafnium (TDMA-Hf) and tetrakis-dimethylamino zirconium (TDMA-Zr) were used as precursors with oxygen plasma as oxidant during the deposition. Similar to the previous process, there was no reaction on the Au surface during the PE-ALD process. The HZO film was patterned by RIE before deposition of a top sputtered W electrode. An evaporated Au/Ti bilayer was then lifted-off to define the W top electrode using RIE. Finally, the fabrication was completed with the identical thermal step of RTA at 500 ℃, as described previously.

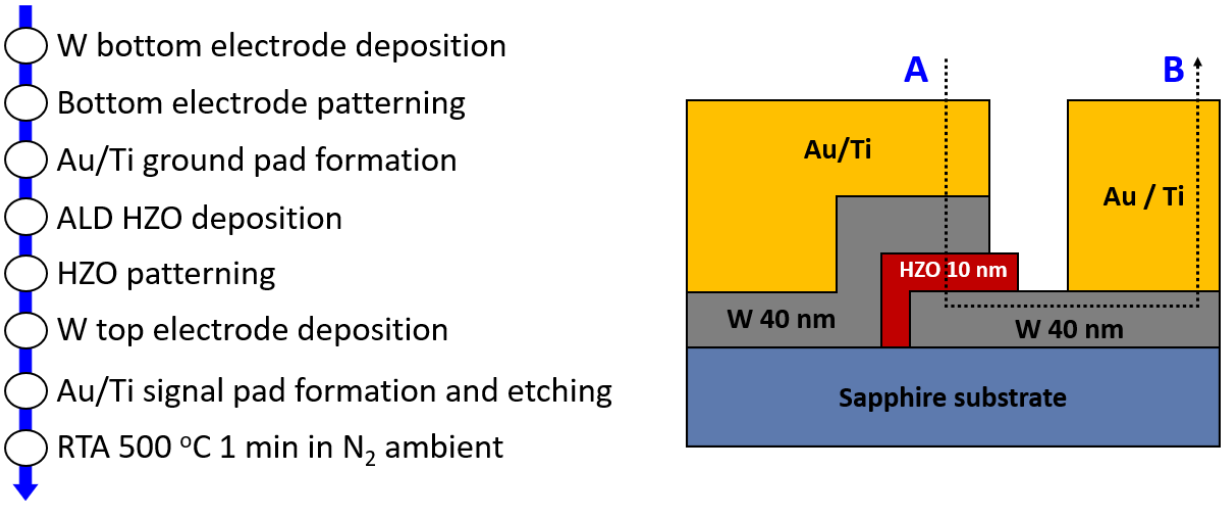

Fig. 2-2. Fabrication process flow and cross-sectional schematic of W/HZO/W MFM capacitor with low parasitics. 10-nm FE-HZO was deposited by PE-ALD. Current flows from A to B during measurements.

[1] The PE-ALD process was carried out by Dr. Elham Borujeny in Professor Ken Cadien group at University of Alberta.

In addition to the MFM devices, both samples include several calibration test structures, Open and Short, integrated on the same chip to enable accurate parasitics calibration, as discussed in Section 2.2.2.

2.1.2 Coplanar Waveguide MFM Structure

As mentioned in Section 1.4, an impedance-matched layout is an essential requirement to obtain accurate small-signal characteristics in the GHz range. Accordingly, MFM structures were carefully designed by adopting a ground-signal-ground (GSG) coplanar waveguide configuration to minimize reflected signals during RF measurements.

Fig. 2-3 displays the coplanar waveguide device designed based on a calculation to maintain a characteristic impedance of 50 Ω along the space between the signal and ground lines on a sapphire substrate. The 10-nm FE-HZO MFM structure is located at the center of the device between the signal and ground lines to form an equivalent circuit with a parallel capacitor connection in a transmission line configuration.

To validate the layout, electromagnetic simulations were carried out using the Momentum tool within Keysight ADS software[2] based on the specific layout information that will be described in Chapter 5. Fig. 2-4 shows the comparison of the simulated S-parameter data between the designed coplanar waveguide (line) and ideal capacitor (dash). The simulation of the coplanar waveguide incorporating a 24-μm^2 area MFM capacitor is implemented with an assumption that the FE-HZO

[2] The electromagnetic simulation of the layout was executed by Ignacio Meirás and Professor Jesús Grajal at Universidad Politécnica de Madrid.

is characterized by a voltage-independent and frequency-independent dielectric constant (εr) of 27. As a result, the S-parameter data comprises responses not only from the MFM capacitor but also from any parasitic elements present in the device itself. On the other hand, the ideal capacitor data represents the device characteristics of the same MFM structure as the coplanar waveguide but without any parasitic elements. The excellent match between both sets of S-parameter calculations in both magnitude and phase up to 50 GHz confirms the accurate design of the coplanar waveguide structure. This suggests that the designed layout is valid for extracting the intrinsic MFM response from measured data in actual coplanar GSG devices.

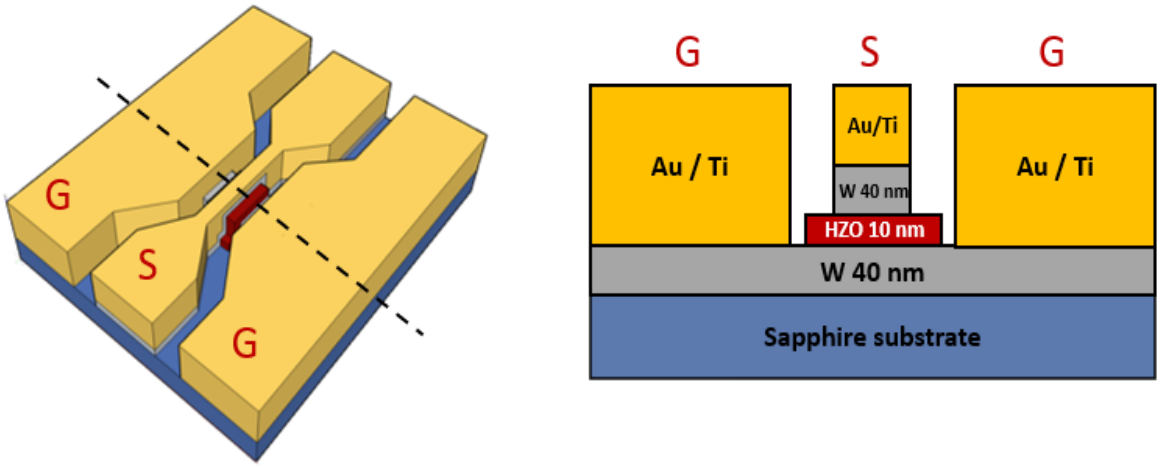

Fig. 2-3. 3D schematic (left) and cross-sectional schematic of Z-matched coplanar waveguide configuration incorporating a 10-nm thick FE-HZO MFM structure.

After confirming the layout validity, the devices were fabricated following the W-electrode MFM capacitor fabrication process described in the previous section. To execute the de-embedding process precisely, calibration test structures, Open, Short, and Thru patterns, were also integrated on the same chip.

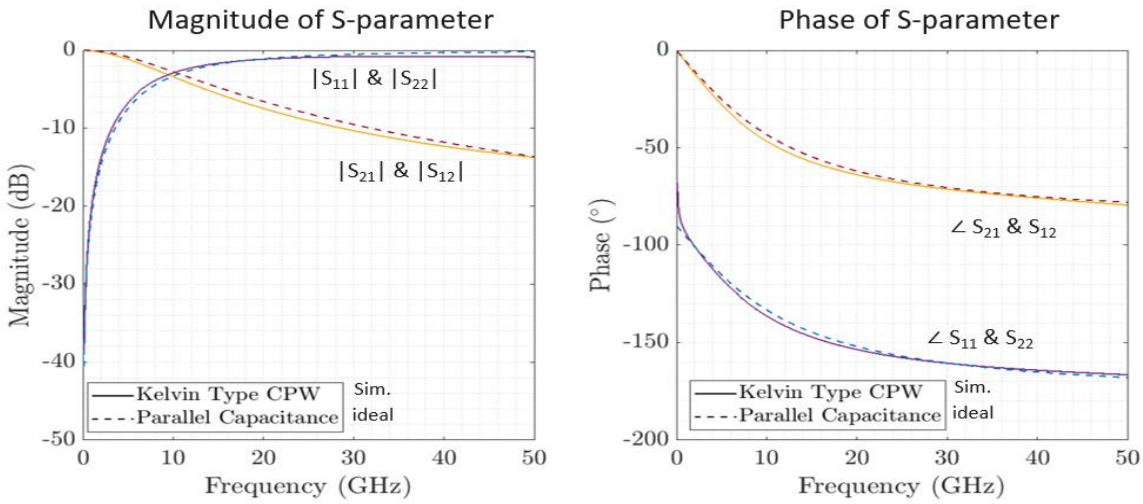

Fig. 2-4. Comparison of electromagnetic simulation results between designed coplanar waveguide structure (line) and ideal capacitor (dash) up to 50 GHz.

2.1.3 Ferroelectric Property

To confirm the ferroelectric nature of the two MFM structures, TiN/HZO/TiN and W/HZO/W both with 10-nm HZO thickness, large-signal triangular waveforms and small-signal capacitance-voltage (C-V) characteristics were obtained. The capacitors were woken-up prior to conducting the measurements by optimized electric field cycling that was customized separately for TiN- or W-electrode samples.

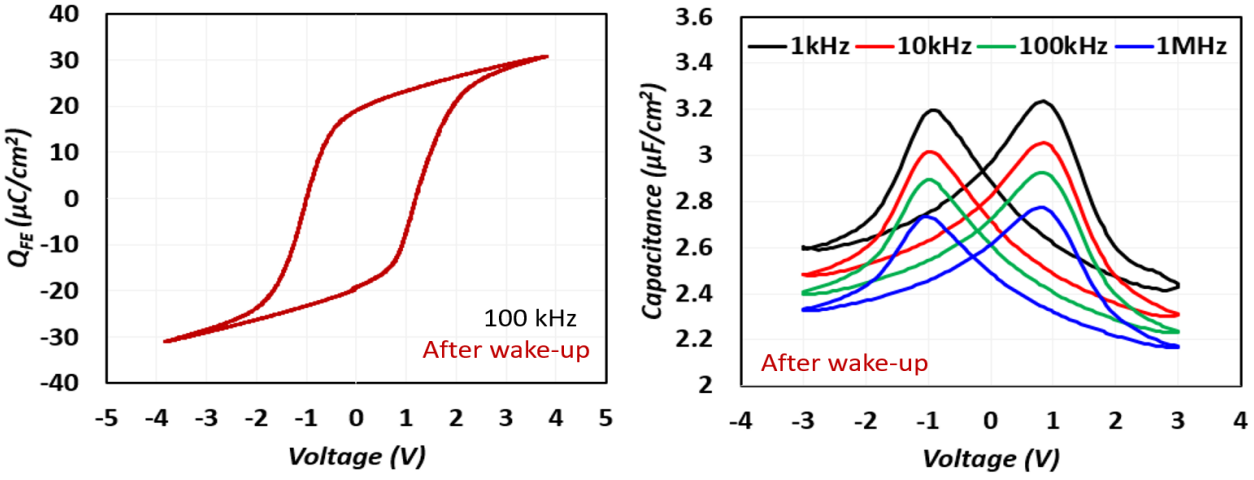

Fig. 2-5. Charge-Voltage loop (left) and small-signal C-V (right) characteristics of 2500-μm^2 TiN/HZO/TiN MFM structure. HZO thickness is 10 nm.

The TiN/HZO/TiN MFM capacitors were woken-up by means of 3×10^4 cycles of a ±4.0 V triangular voltage signal at 10 kHz, and the cycling was finished with a negative triangular half waveform. The charge-voltage (Q-V) characteristics were measured by applying a bipolar ±4.0 V triangular waveform at 100 kHz, and the C-V characteristics were evaluated by sweeping voltage back and forth from -3 V to 3 V with ac signals of 30 mV amplitude at various frequencies. Typical results are shown in Fig. 2-5. A typical Q-V hysteresis loop is observed showing a coercive voltage of 1.1 V and a remanent polarization (P_r) of 19 μC/cm^2. Also, typical butterfly shapes of the C-V characteristics and their frequency dispersion were observed in the same capacitor structure.

The W/HZO/W MFM capacitors were also characterized using a similar manner. The capacitors were woken up by means of 3×10^4 cycles of a ±3.0 V trapezoidal voltage pulse with a pulse width of 500 ns and 40 ns rise/fall time. The Q-V characteristics were evaluated using a bipolar ±3.0 V triangular waveform at a frequency of 100 kHz. The same C-V measurement method as for theTiN/HZO/TiN MFM capacitors was employed. In Fig. 2-6, a typical Q-V hysteresis loop is shown that exhibits a coercive voltage of 1.5 V and a remanent polarization (P_r) of 26 μC/cm^2. Also, typical butterfly shapes are observed in the C-V characteristics.

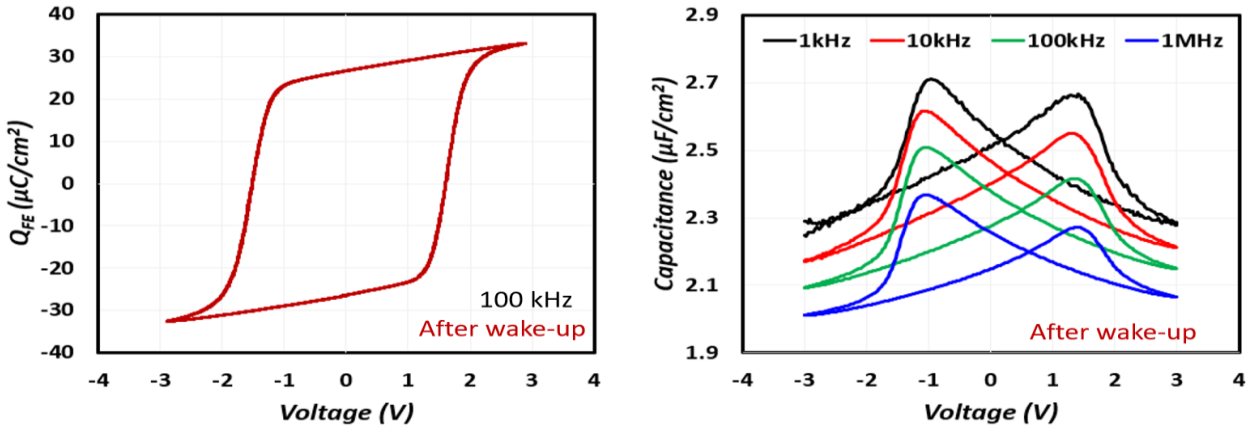

Fig. 2-6. Charge-Voltage loop (left) and small-signal C-V (right) characteristics of 370-μm^2 W/HZO/W MFM structure. HZO thickness is 10 nm.

Although the characteristics of the coplanar waveguide structures are not presented in this section, a comparable result to the W-electrode MFM data displayed in Fig. 2-6 is observed since the samples have an identical MFM structure.

2.2 Electrical Measurement Setup for Large-Signal Analysis

In this section, we will introduce two different measurement setups designed to minimize parasitic effects. These setups are specifically used for large-signal analysis. The first setup, in which external resistors of different values are inserted in series with the MFM capacitor is called resistor-MFM (R-MFM), and the second setup, with no external resistor, is referred to simply as MFM.

After presenting these setups, we will explain their calibration procedures in detail. The purpose of calibration is to ensure accurate measurement by accounting for all parasitic elements present in the setups. We will provide a thorough explanation of the calibration procedures, which are crucial for minimizing errors and obtaining precise results.

2.2.1 Measurement Setup

FE switching dynamics of MFM capacitors with large-signal have been investigated using low-parasitic measurement setups that were carefully calibrated. We built two configurations. Setup 1 (Fig. 2-7(a)) was designed to observe any plausible existence of transient negative capacitance (NC) effects in a R-MFM circuit with TiN/HZO/TiN structures, as discussed in Section 3.2.1. Setup 2 (Fig. 2-7(b)) was configured to isolate the intrinsic dynamics of the TiN-electrode MFM structure under small RC time constant conditions and to compare with the data obtained from Setup 1, as discussed in Section 3.2.2. Additionally, Setup 2 provided accurate dynamics of the

MFM structures that have been instrumental in building a new FE switching model (TiN/HZO/TiN), as presented in Section 3.3 as well as in studying the imprint effect (W/HZO/W) in Chapter 4. Table 2-1 presents an overview of all large-signal experiments. Both setups consist of a pulse generator (Keysight B1525A HV-SPGU) and an oscilloscope (Agilent DSO6054A with 500-MHz bandwidth in Chapter 3, or CX3324A with 200-MHz bandwidth in Chapter 4) without any additional instruments. The bandwidth of these instruments is high enough to cover the frequency range of the measurements in this work.

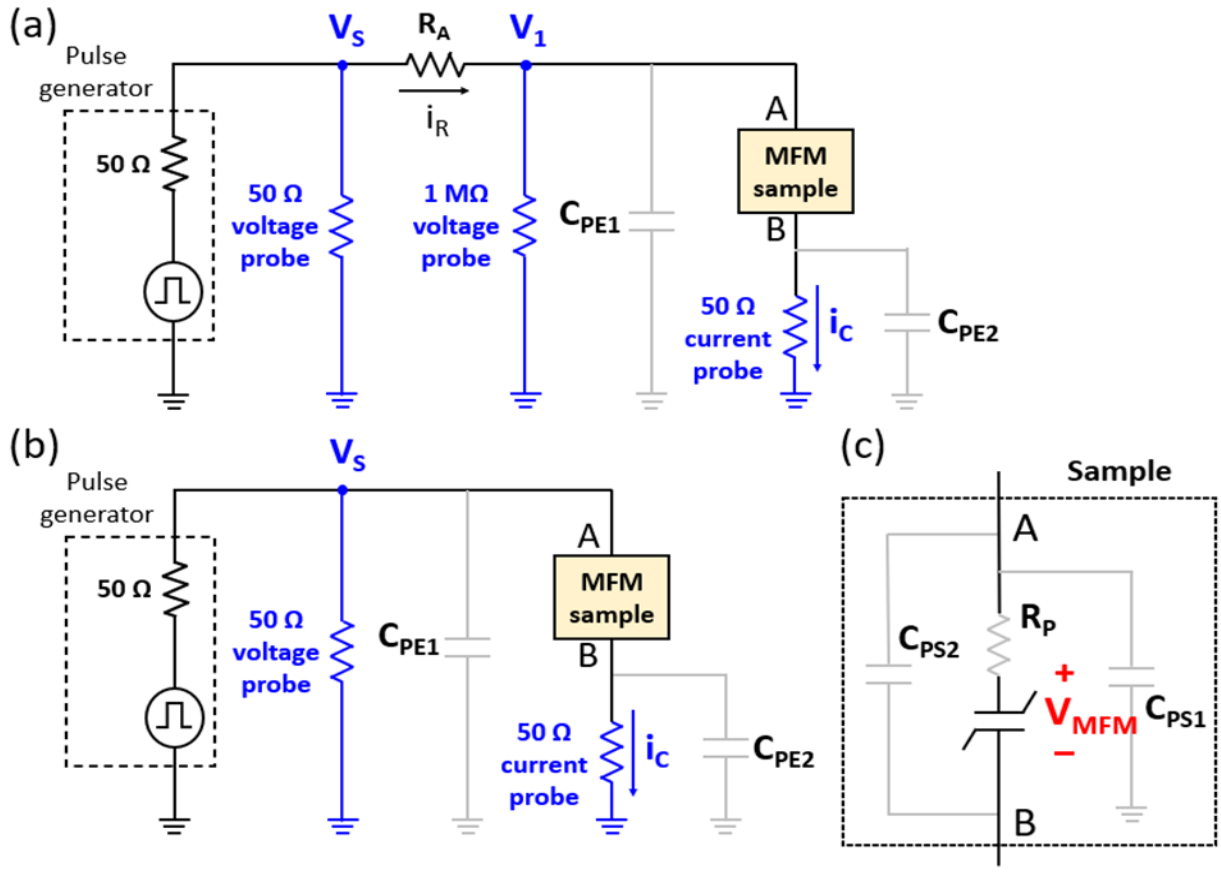

Fig. 2-7. Circuit diagrams of two measurement setups used in large-signal analysis. (a) Setup 1: a three-probe configuration to study dynamic behavior in R-MFM circuit and (b) Setup 2: a two-probe configuration to study intrinsic dynamic MFM behavior and imprint effect. (c) Equivalent circuit of MFM sample. A and B in figures correspond to the probed electrodes as shown in Fig. 2-1 and Fig. 2-2.

To obtain reliable FE behavior, all measurements in this thesis work were performed on woken-up MFM devices by the methods in section 2.1.3. The devices underwent a proper initialization process using electric field cycling to erase the FE switching history that could lead to inaccurate results due to the imprint effect. The cycling condition depends on the MFM structures, (a) TiN/HZO/TiN: 3000 cycles of a ±4.0 V bipolar trapezoidal pulse 2 μs wide and rise/fall times of 40 ns and (b) W/HZO/W: 3000 cycles of a ±3.0 V bipolar trapezoidal pulse 500 ns wide and rise/fall times of 40 ns.

Experiments	**Structures**	**Setup / Oscilloscope**
Transient NC effect (Section 3.2)	TiN/HZO/TiN	Setup 1 and Setup 2 / DSO 6054A
New FE switching model (Section 3.3)	TiN/HZO/TiN	Setup 2 / DSO 6054A
Imprint effect (Chapter 4)	W/HZO/W	Setup 2 / CX3324A

Table 2-1. Summary of setups and samples for different experiments.

2.2.2 Calibration

Accurate calibration and minimization of parasitics are essential for observing the intrinsic FE dynamics in large-signal analysis. In this section, a calibration procedure is described with a TiN-electrode MFM sample first, then calibration results are shown for both TiN- and W-electrode MFM samples.

In Fig. 2-7, Setup 1 is a three-probe configuration, whereby Setup 2 is a two-probe configuration without an external resistor. The gray components represent the relevant parasitics of the setups [Fig. 2-7(a) and (b)] and the device [Fig. 2-7(c)]. C_{PE1} and C_{PE2} represent the capacitance from cables, probes, and scopes associated with each terminal of the device. C_{PS1} represents the parasitic

pad capacitance of the device to the grounded chuck, while C_{PS2} represents the pad-to-pad capacitance of the device. R_P represents the parasitic resistance of the sample. In both setups, the voltage from the pulse generator, V_S, and the current through the sample, i_C, are monitored by 50-Ω oscilloscope probes. In addition to eliminating pulse signal reflections and additional capacitance from the oscilloscope, this low impedance allows us to ignore any parasitic capacitance located in parallel with the probes since the current flowing through it is comparatively negligible. Thus, C_{PE2} in Setup 1 and C_{PE1}, C_{PE2}, and C_{PS1} in Setup 2 can be ignored. On the other hand, accurate measurement of V_1 in Setup 1 demands the use of a 1-MΩ impedance probe. This makes C_{PE1} relevant in Setup 1. Therefore, the parasitic capacitances that should be calibrated are C_{PE1} and C_{PS1} in Setup1 and C_{PS2} in both setups.

C_{PE1} of Setup 1 was determined by carrying-out pulsed measurements without a sample on the stage. Different sets of rise/fall time of the trapezoidal pulse and R_A values were used. The measured transient response of V_1 was fitted to $V_1(t) = V_S\left(1 - e^{-t/R_A C_{PE1}}\right)$ with the appropriate values of R_A and V_S. This yielded C_{PE1} = 87 pF.

Similarly, the parasitic capacitances of the sample, C_{PS1} and C_{PS2}, were determined using an open calibration structure (no bottom electrode between two Au pads based on Fig. 2-1 and Fig. 2-2) on an identical sample. By connecting probes to both pads of the open structure, various trapezoidal pulses were applied to Setup 1 with different R_A values. After fitting to the above equation, the measurements yielded a parasitic capacitance of 97 pF. This is the total parasitic capacitance of the entire measurement Setup 1, which consists of C_{PE1}, C_{PS1}, and C_{PS2}. Then, to separate C_{PS1} and C_{PS2}, the open structures were evaluated once more with the probe landing only on pad "A" in Fig. 2-1 (Fig. 2-2 for W-electrode sample). This excludes C_{PS2}, but C_{PS1} remains electrically connected. This also yielded a parasitic capacitance of 97 pF, identical to the previous result. This allows us

to conclude that C_{PS1} = 10 pF, while C_{PS2} is negligible (<1 pF). As C_{PE2} and C_{PS2} are found to be negligible, C_{PT} (effective total capacitance) of Setup 1 is effectively the sum of C_{PE1} and C_{PS1}, and Setup 2 has no effective parasitic capacitance.

Using a shorted Metal-Metal calibration structure, i.e., one that does not include the HZO layer, so that pad B lands directly on the bottom TiN electrode, a parasitic series resistance, R_p = 60 Ω was extracted. By following the same procedure described above, a W-electrode MFM sample was also evaluated, and the summary is shown in Table 2-2.

Setup	Structures	C_{PE1}	C_{PE2}	C_{PS1}	C_{PS2}	C_{PT}	R_P
Setup 1	TiN/HZO/TiN	87 pF	ignored (50 pF)	10 pF	< 1pF	97 pF	60 Ω
Setup 2	TiN/HZO/TiN	ignored (87 pF)	ignored (50 pF)	ignored (10 pF)	< 1pF	ignored (97 pF)	60 Ω
Setup 2	W/HZO/W	ignored (87 pF)	ignored (50 pF)	ignored (7 pF)	< 1pF	ignored (94 pF)	6.8 Ω

Table 2-2. Parasitics of setups and samples with respect to experiments. Only the parasitics indicated by red are relevant (see text).

Following Ohm's law, the voltage across the capacitor can be simply calculated by $V_C = V_1 - i_C(R_P + 50\ \Omega)$ in Setup 1, with a similar expression in which V_S is substituted for V_1 for Setup 2. Importantly, because the voltage applied to the sample (V_1 in Setup 1 and V_S in Setup 2) and the current flowing through the sample, i_C, are essentially measured directly (since the effect of C_{PE2} is negligible as discussed above), in our approach, any error-prone integral or derivative calculations are avoided in the extraction of the dynamics of the MFM structure. Therefore, in both configurations, the transient response, V_{MFM}–i_C, of the FE capacitor is immune to any parasitic capacitance and calculation errors; only R_P plays a role. Nevertheless, in our studies, we

determined the parasitic capacitances as described above in order to understand their role in the interpretation of the results in other configurations used in the literature, as we will discuss in Section 3.2.1.

2.3 Electrical Measurement Setup for Small-Signal Analysis

2.3.1 Measurement Setup

The 24-μm^2 area coplanar waveguide W/HZO/W MFM structure validated through electromagnetic simulation in Section 2.1.2, was investigated by small-signal analysis over a broad range of frequencies. Towards this, three instruments were employed, a parametric analyzer (1 kHz to 1 MHz), an impedance analyzer (1 MHz to 100 MHz), and a vector network analyzer (VNA) (100 MHz to 50 GHz), as shown in Fig. 2-8. The instruments measured the frequency response of the coplanar waveguide at different DC bias points by sweeping voltage back and forth from -3 V to 3 V. To ensure consistency between the tools, the same ac level of 32 mV was applied.

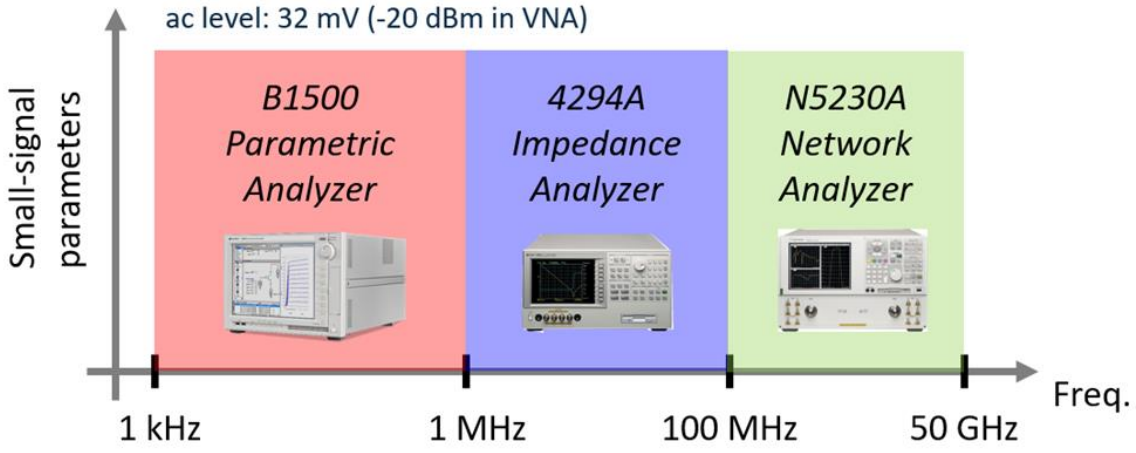

Fig. 2-8. Three different instruments used in small-signal characterization over a broad frequency range from 1 kHz to 50 GHz.

2.3.2 Calibration and De-embedding Process

Similar to the large-signal analysis in Section 2.2.2, all the setup and device parasitics must be carefully calibrated for accurate small-signal analysis. In addition, as the device structure parasitics become relevant in the GHz regime, an exact de-embedding process is necessary for extracting the intrinsic MFM response.

Before starting actual measurements, the three instruments were calibrated by following a procedure recommended in the manual of each tool. The parametric analyzer (Keysight B1500) was calibrated with an open circuit (without sample) using Phase, Open, and Short Compensation provided by Keysight EasyEXPERT software. The impedance analyzer (Agilent 4292A) was calibrated using Phase, Open, Short, and Load Compensation by connecting the company provided calibration kit to the end of the 42941A Impedance Probe. The calibration for VNA (Agilent N5230A) was conducted using Open, Short, Match, and Gamma Term Compensation in WinCal XE 4.5 software by connecting to the corresponded test structures (Open, Short, Load, and Thru) in a Standard Impedance Contact Substrate (P/N 101-190 S/N 272383).

Following the instrument calibration, fabricated test patterns (Open, Short, and Thru) were evaluated by VNA in the GHz range to extract coplanar waveguide device parasitics. As described in Section 2.1.2, the patterns are integrated on the same chip, and they are associated with the parasitics in the coplanar waveguide incorporating a 24-μm^2 area MFM structure that we will focus primarily on. Fig. 2-9 illustrates a schematic of the parasitics in the specific device (Top) and its equivalent circuit (Bottom). The top figure shows that the parasitic elements consist of C_{pad} and C_{line} between the signal and ground lines, and L_{line} and R_{line} on the signal line. These parasitic

elements are attached to the intrinsic MFM structure as shown in the bottom figure, and it demonstrates the necessity of performing a de-embedding process to extract the intrinsic MFM response from the measured S-parameter data. Based on the equivalent circuit, values of the parasitics were extracted by implementing an optimization process in Keysight ADS software with the measured S-parameter data of the test patterns. This yielded C_{pad} = 25 fF, C_{line} =0.924 fF, L_{line} = 83.8 pH, and R_{line} = 8.7 Ω. The equivalent circuit with this set of parasitics was applied to small-signal parameters measured over the entire frequency range. Therefore, accurate small-signal parameters of the intrinsic device can be extracted by eliminating the parasitic components from the measured data using the de-embedding process.

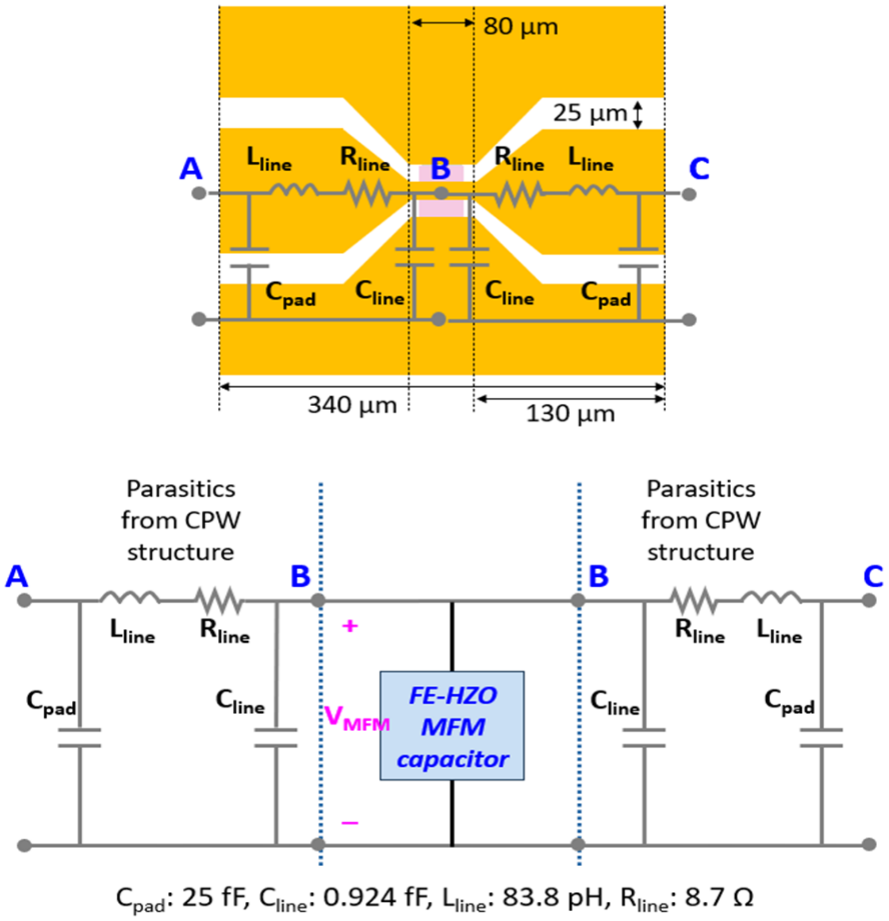

Fig. 2-9. Parasitic elements in specific coplanar waveguide device (Top) and its equivalent circuit (Bottom).

2.4 Summary

This chapter discusses the design of low-parasitic samples and their fabrication as well as the measurement setups used for their characterization. We emphasize the importance of minimizing circuit and setup parasitics and their accurate consideration in order to extract the intrinsic MFM dynamics. Low-parasitic sample design and accurate calibration of the setup and the device parasitics are essential for precise analysis. We have described three different device structures, a TiN/HZO/TiN MFM capacitor, a W/HZO/W MFM capacitor, and a coplanar waveguide integrated W/HZO/W MFM capacitor. These devices were fabricated on a sapphire substrate to minimize parasitics, and suitable test patterns were integrated on the same chip to accurately evaluate the intrinsic device parasitic elements. Careful calibration of the instruments was also carried out. Furthermore, a precise de-embedding process was employed in small-signal analysis to remove parasitic elements from the measured data.

Chapter 3 Modeling of FE-HZO Switching Dynamics in Large-Signal Analysis

3.1 Introduction

As the first step to successfully develop an accurate dynamic model for FE circuits, it is crucial to gain a clear observation of the intrinsic FE dynamics. To achieve this, it is necessary to resolve the ongoing controversy surrounding the existence of negative capacitance (NC) in Resistor-MFM (R-MFM) circuits. In this chapter, therefore, we have carried out detailed experimental dynamic studies of FE-HZO MFM devices using the two accurately calibrated setups described in Section 2.2.

First, with the goal of capturing evidence of NC existence in R-MFM circuits, various pulse measurements under a wide range of conditions are demonstrated and the results are compared to the intrinsic MFM dynamics obtained in a simple resistor-free MFM circuit. Our investigation leads us to conclude that there is no evidence of transient NC effects in our R-MFM circuits under the studied conditions.

Later in this chapter, we introduce a rigorous formulation of the nucleation-limited switching (NLS) model that lends itself to an efficient numerical solution that is suitable for arbitrarily varying electric fields and could form the basis of an efficient compact model for FE stand-alone capacitors and other devices that incorporate FE films, such as memory devices. Particular attention is directed towards correctly capturing the incubation time of embryonic reversed polarity nuclei that forms the basis of the NLS model. This is essential for a proper consideration of the

accumulated (partial) polarization reversal under pulsed voltage drives with arbitrary duty cycles of great importance, for example, in neuromorphic device applications [40]. Simulations employing our formulation are consistent with a diverse set of experimental studies.

3.2 Results of Switching Dynamics Measurements in MFM Circuits

In this section, we demonstrate the results of switching dynamics of MFM structures using Setup1 and Setup2 described in Section 2.2.

3.2.1 R-MFM Experimental Results

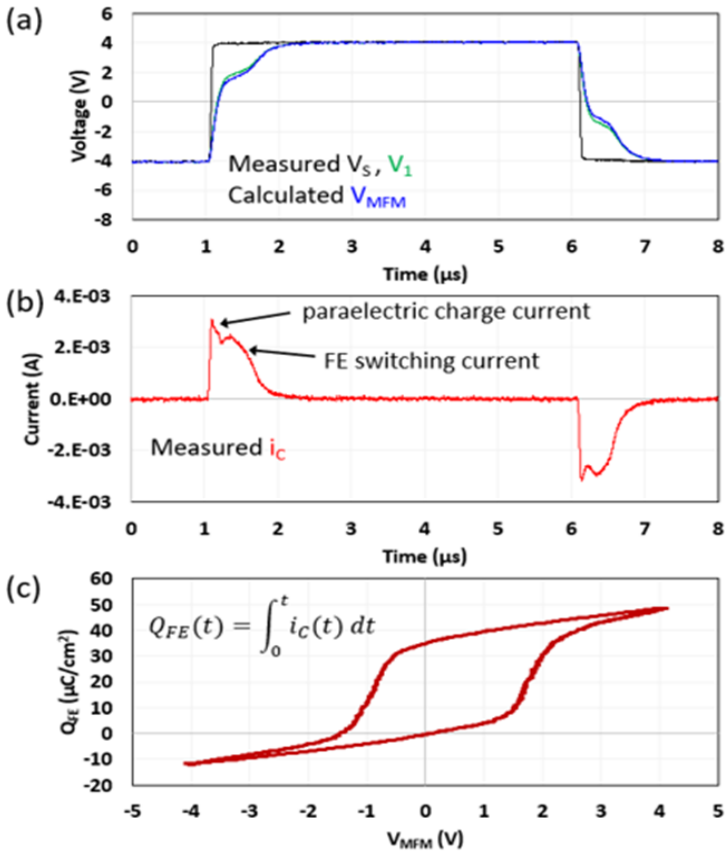

Fig. 3-1. Bipolar switching response of MFM capacitor (2500 µm^2) using Setup 1 with R_A = 814 Ω. (a) V_S, V_1 and V_{MFM}, (b) i_C response with time. (c) Q_{FE}-V_{MFM} characteristics from (a) and (b). No transient NC appears in contrast with other works in similar setups.

Fig. 3-1 shows typical ±4 V bipolar pulse switching response of a 2500-μm^2 area capacitor after wake-up in an R-MFM circuit (Setup 1) with R_A = 814 Ω. A sufficiently long pulse width is used in this case (5 μs) so that the transient response completely settles. The pulse edges have a 5 ns/V ramp rate. Measured V_S and V_1 are shown in Fig. 3-1 (a) with measured i_C shown in Fig. 3-1 (b). From these measurements, V_{MFM} is extracted and is also shown in Fig. 3-1 (a). The notation used here is described in Section 2.2. Fig. 3-1 (c) plots the instantaneous Q_{FE} vs. V_{MFM} characteristics where Q_{FE} is obtained by integrating i_C, as indicated in the legend of Fig. 3-1 (c). All measured Q_{FE}-V_{MFM} loops in Section 3.2 are constructed by integrating i_C assuming that Q_{FE} = 0 when V_{MFM} = 0. As a result, they are not centered along the y-axis.

Similar to other publications [41, 42, 43, 44, 45], a non-monotonic current waveform is obtained which consists of the paraelectric response at the leading and trailing edge of the pulse followed by the FE switching response [Fig. 3-1 (b)]. However, no negative slope in the V_{MFM} vs. t waveform of Fig. 3 (a), believed to be evidence of NC in [42, 43, 44, 45], is observed. NC-like behavior is also absent in the Q_{FE}-V_{MFM} characteristics of Fig. 3-1 (c) which show a standard quasi-static hysteresis loop without any negative slopes, in contrast with other works [42, 43, 44, 45].

To investigate further the possible existence of transient NC behavior in the R-MFM circuit configuration, MFM capacitors were characterized under a variety of bipolar switching pulse schemes and circuit elements using the same, accurately calibrated Setup 1 in Section 2.2.1.

Fig. 3-2 shows two sets of pulse measurement data with different pulse schemes of 5 μs long pulses with R_A=814 Ω. In Fig. 3-2 (a) and (b) we examine transients driven by different voltage amplitude

waveforms of ±0.5 V to ±4.0 V and a ramp rate of 5 ns/V. In Fig. 3-2 (c) and (d), we study the response of a ±4 V voltage waveform with ramp rates of 5 ns/V to 625 ns/V, i.e., different frequency content in the pulse edges. Both Figs. 3-2(a) and (c) show V_{MFM}-t responses exhibiting positive slopes without any NC evidence. Accordingly, negative slopes are also absent in the Q_{FE}-V_{MFM} characteristics. As shown in Fig. 3-2 (b), typical major and minor loops are clearly captured at different voltage amplitudes in contrast with the results in [44]. In Fig. 3-2 (c) and (d), V_{MFM}-time exhibits significantly different dynamics, whereas Q_{FE}-V_{MFM} loops show only a small ramp rate dispersion. This is because the MFM structure has fast enough intrinsic FE switching speed to respond to the applied voltage in the scale of the ramp rate. The small frequency dispersion, i.e., loop width increases with frequency, in Fig. 3-2 (d) originates from the nature of FE switching dynamics, as is well-known [46].

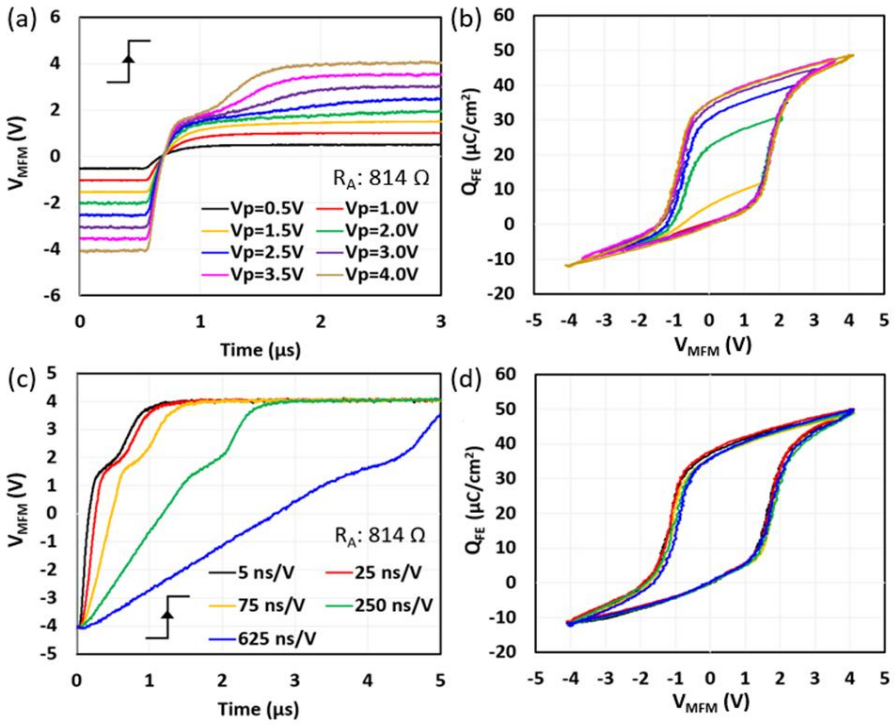

Fig. 3-2. Extracted V_{MFM}-time and Q_{FE}-V_{MFM} of MFM capacitor (2500 μm^2) using Setup 1. (a), (b) Voltage amplitude dependence and (c), (d) ramp rate dependence. Loops show only quasi-static major and minor hysteresis loops without negative slopes.

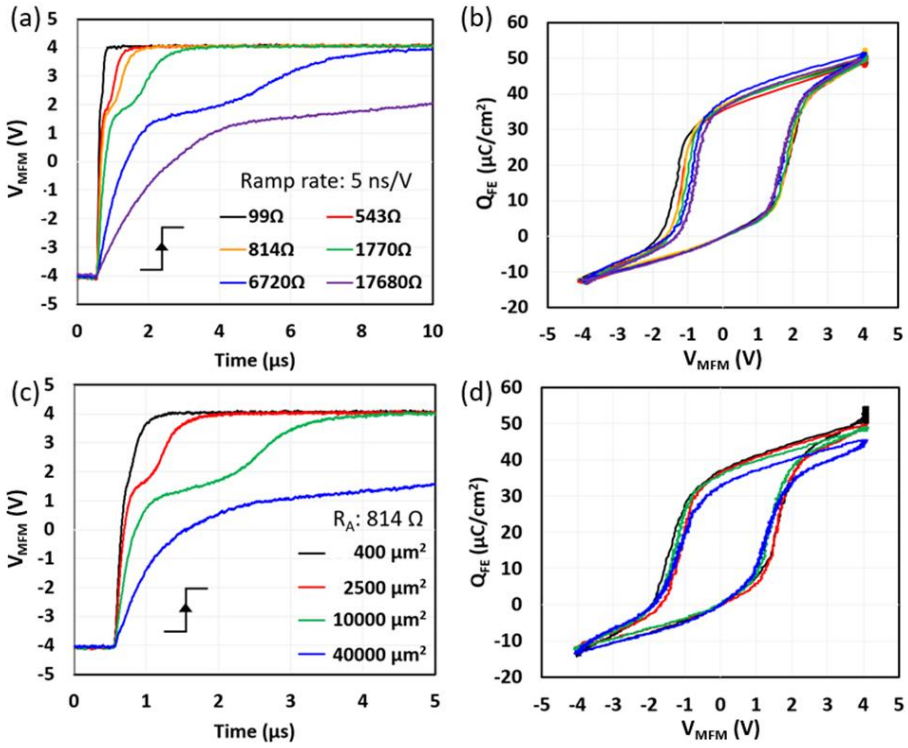

Fig. 3-3. Calculated V_{MFM}-time and Q_{FE}-V_{MFM} of MFM capacitor (2500 µm^2) using Setup 1. (a), (b) R_A dependence and (c), (d) Area of capacitor dependence after calibrating all elements of measurement. Pulse width was 30 µs to compensate for a long RC time constant of each setup. Loops show only typical hysteresis without negative curvature.

We have additionally carried out pulse measurements with different values of the external resistor [Fig. 3-3 (a) and (b)] and with samples of different areas [Fig. 3-3 (c) and (d)] spanning two orders of magnitude in each case. Likewise, the V_{MFM}-t responses and the extracted Q_{FE}-V_{MFM} loops only exhibit positive slopes, and they match closely the quasi-static hysteresis loop, regardless of conditions. The slight change between the loops can also be explained by the nature of the FE dynamics, as in Fig. 3-3 (d). In Fig. 3-3 (b), the negative coercive voltage shifts as R_A increases. This is in contrast with the positive coercive voltage which remains largely unchanged. Although the exact physics is unclear, it is likely that it is due to the imprint behavior of FE-HZO, as discussed in Chapter 4. Nevertheless, this asymmetric behavior does not affect the validity of our conclusions regarding NC operation. The slight P_r decrease with area in Fig. 3-3 (d) is attributed

to the FE switching dynamics in that the magnitude of the polarization at V_{MFM} = 4 V ends up being smaller due to the shorter time that the sample sits at this voltage as the RC time constant increases [18]. The reason that the maximum charge increase is only observed at a positive voltage is that the loops were calculated with zero initial charge assumption, as mentioned above.

To summarize, within the broad range of conditions that we have examined, we have not observed the negative dip in the V_{MFM}-t response and the resulting negative slope in Q_{FE}-V_{MFM} loops that are believed to be characteristic of intrinsic NC behavior in FE-HZO capacitors [42, 43, 44, 45]. Although not shown here, the absence of a negative slope in the Q_{FE}-V_{MFM} loops has also been verified in FE-HZO capacitors with 20 nm thick HZO.

The next section focuses on the intrinsic dynamic characterization of MFM capacitors using Setup 2 (MFM) that is configured for small RC time constant measurements. We then compare the results to those of Setup 1 (R-MFM).

3.2.2 Intrinsic MFM Dynamics

In this section, we have characterized smaller MFM capacitors using Setup 2 in an effort to observe the intrinsic FE dynamics on a nanosecond scale [Fig. 2-7 (b)]. Bipolar pulses with voltage amplitudes from ±1.0 V to ±4.0 V, 40 ns rise time and 200 ns pulse width were applied to 400 μm^2 area capacitors. Extracted V_{MFM} vs. t waveforms are shown in Fig. 3-4 (a). Due to minimized setup parasitics and the small sample area, a low RC time constant of order 2 ns is achieved. This enables a fast-transient response and FE switching of the MFM structure in the nanosecond range. For low voltage amplitudes, in this case 1 V, this yields a clear trapezoidal paraelectric current waveform

[Fig. 3-4 (b)] something that was not observed in Setup 1 due to its relatively higher RC time constant [Fig. 3-1 (b)]. For high voltage amplitudes, a clear peak corresponding to FE switching current is observed.

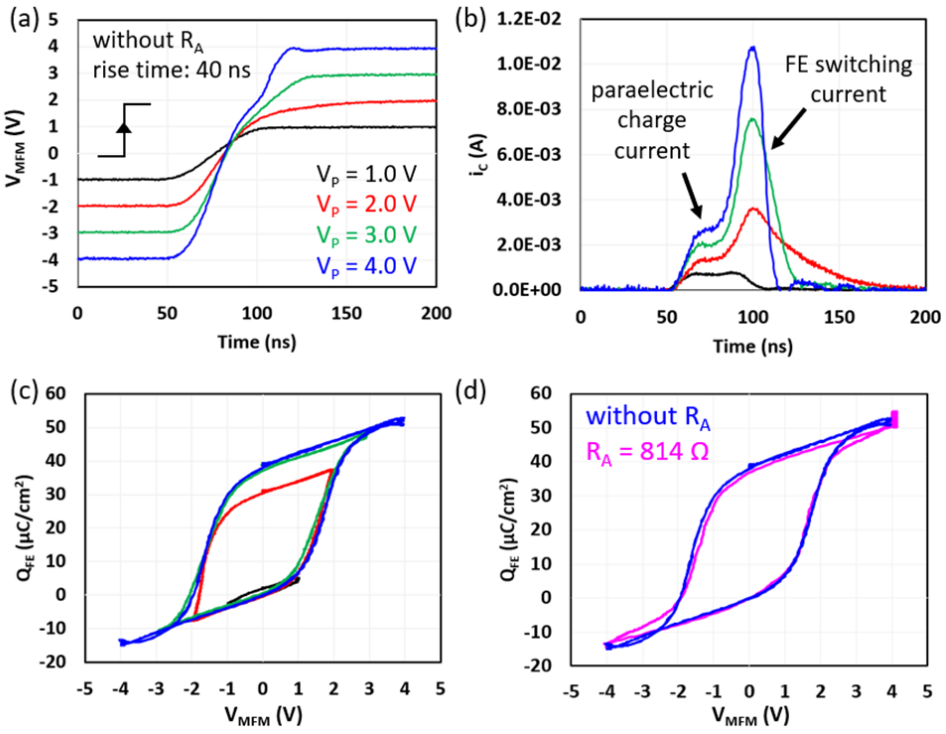

Fig. 3-4. (a) V_{MFM}-time, (b) i_C-time, and (c) Q_{FE}-V_{MFM} of 400 μm^2 area MFM capacitor using well-calibrated Setup 2 with different voltage amplitudes (1.0 V to 4.0 V). A trapezoidal paraelectric charge current waveform is observed in (b) due to the low RC time constant of Setup 2. (d) Comparison of Q_{FE}-V_{MFM} of 400 μm^2 area MFM capacitor when R_A = 0 in Setup 2 (blue) and R_A = 814 Ω (magenta) in Setup 1 (black in Fig. 3-3 (d)). Both loops match well regardless of the presence of R_A.

As shown in Fig. 3-4 (c), Q_{FE}-V_{MFM} characteristics extracted from the measured data show typical major and minor FE loops with the expected behavior depending on the applied voltage amplitude. Based on these data, a FE switching time constant of order 3 ns was extracted using a new FE dynamic model that will be presented in Section 3.3. Furthermore, as shown in Fig. 3-4 (d), the Q_{FE}-V_{MFM} loop obtained with the ±4.0 V amplitude voltage waveform (blue) shows a good

agreement with the data obtained from the R-MFM circuit using setup 1 on the same sample (magenta). This result gives confidence on the experimental methodology developed here that relies on minimizing and carefully calibrating parasitics.

In summary, we have found no evidence of transient NC effects in the switching characteristics of R-MFM circuits; instead, the dynamics are consistent with those of a simple resistor-free MFM circuit. This consistency of the observed intrinsic FE dynamics, regardless of the circuit environment, allowed us to move on to modeling work.

3.3 Finite-Difference Nucleation Limited Switching (FD-NLS) Model

In the previous section, we have observed the intrinsic FE switching dynamics using Setup 2. Here, we suggest a new NLS model called the finite-difference NLS (FD-NLS) model, which is rigorously derived from the elementary NLS equation, and we show its implementation using the finite difference method. We will then discuss the performance of the new model by comparing it against experimental intrinsic FE dynamics. We introduce the key concept of incubation time.

3.3.1 NLS Model – Constant Electric Field

Polarization reversal of a ferroelectric material is initiated by the reversal of the electric field in the material and consists of incubation of reversed polarity domain nuclei within elementary regions followed by expansion of the reversed domains and eventual coalescence of domains into a stable configuration. The NLS model begins with the elementary equation [47, 14, 15, 16]:

$$p(t,\tau) = 1 - e^{-\left(\frac{t}{\tau}\right)^{\beta}} \tag{3-1}$$

where p is the cumulative fraction of reversed polarization at time t in an elementary volume of a FE material system following transition initiation at t=0. τ is the *critical time for polarity reversal and beta is an exponent*. Clearly, since $p(t,\tau)$ is cumulative and not instantaneous, equation (3-1) is valid only if τ and β are constants independent of time, i.e., polarization reversal takes place under a constant excitation (electric field).

According to the original K-A-I theory, the critical time, τ, depends on the density of reversed domain nucleation sites, the mobility of domain walls and the magnitude of the electric field acting on the domain walls. β roughly depends on the material dimensionality; so for 2D films which are the subject of this work β is approximately 2 [47, 14, 17]. However, there is good evidence that particularly in polycrystalline materials, where the elementary volume can be considered confined by crystalline grain boundaries [17] [19], those parameters are actually determined by the rate of nucleation of reversed polarity sites within the elementary volume. In other words, domain wall propagation and domain coalescence rates are considered significantly faster than the incubation rate of reversed polarity nuclei. Therefore, in the NLS model, τ is the *critical time for reversed-polarity nucleation* and it is determined by the domain nucleation rate which is constant under constant excitation.

Defining the film areal polarization density as, $P=(2p-1)P_S$, where P_S is the saturated polarization density (also known as remanent polarization), application of equation (3-1) leads to the transient of the polarization areal density reversal in response to a step E-field drive, $E(t)=E_1+E_2u(t)$, where $E_1 \leq 0$ and $E_2>0$, and $u(t)$ is the unit step function as follows:

$$P(t) = -P_S + 2P_S\left(1 - e^{-\left(\frac{t}{\tau}\right)^{\beta}}\right) \tag{3-2}$$

It is assumed here that the film was poled uniformly to its saturated polarization density, $-P_S$, at $t=0^-$ and that it consists of uniform grains with identical τ which is constant in time. Note that unless otherwise stated, all discussions here refer to negative-to-positive polarization reversal.

In the NLS theory τ is assumed to depend on the magnitude of the electric field and a well-accepted empirical expression [20], [24] is as follows:

$$\tau(E) = \tau_0 e^{\left(\frac{E_a}{|E|}\right)^{\alpha}} \tag{3-3}$$

where τ_0 is a constant (the shortest possible critical time at $E=\infty$) and E_a denotes an activation electric field. Therefore, nothing happens for E at or very close to zero because τ is at or near ∞, and for $|E|>0$, τ depends inverse exponentially on the relative magnitude of E to E_a with a power-law parameter α.

It is easy to see that the mathematical origin of equation (3-1) is from the indefinite integration of the standard rate-equation:

$$\frac{dp}{dt} = \frac{1-p}{\tau_{gs}} \tag{3-4}$$

where,

$$\tau_{gs} = \frac{\tau(E)^{\beta}}{\beta t^{\beta-1}} \tag{3-5}$$

Thus, τ_{gs}, is the instantaneous, rate-limiting *grain switching critical time*. Note that for $\beta\neq1$, τ_{gs} depends on elapsed time, t. and it can be much longer or shorter than $\tau(E)$. The elapsed time, t, in the denominator of Equation (3-5) is actually the *accumulated incubation time*, also referred to as *wait time*, for reversed-polarization nuclei formation [e.g., [17]], T_{inc}. While here $T_{inc}=t$, it is

important to distinguish, in general, between incubation time, T_{inc}, and elapsed time, t, for reasons that will become clear in the discussion of variable $E(t)$ that follows. We do so by identifying $T_{inc}(t)$, as an explicit function of t. With this notation, we rewrite equation (3-5) below:

$$\tau_{gs} = \frac{\tau(E)^{\beta}}{\beta T_{inc}(t)^{\beta-1}} \tag{3-6}$$

As already discussed, in a uniform FE film the areal polarization density is $P=s(2p-1)P_S$, where we have introduced s as the sign function of the instantaneous E-field that determines the ultimate limit $P(t=\infty)$ to account for either a positive or negative E-field step. Then, using equation (3-6), equation (3-4) can be rewritten as:

$$\frac{dP}{dt} = \frac{sP_S - P}{\tau_{gs}(E, T_{inc}(t))} \tag{3-7}$$

Then, Equation (3-2), for a positive step of E at t=0, results from the definite integration of equation (3-7) in the time interval 0 to t, with s=1, $T_{inc}(t)=t$, and accounting for the initial condition $P(t=0)=-P_S$.

Equations (3-2) and (3-3) result in a saturating exponential increase of $P(t)$ with t^{β}. However, in typical polycrystalline films the transient appears to be of the form of a "stretched" exponential in time [17, 19, 20]. This has required adjustments to the theory by introducing the notion of non-uniformity among grains requiring variation of the local E or E_a among grains due to various lattice defects. Different authors have explored various forms of statistical distribution of the local electric field [17, 19, 20, 24].

A simple implementation is to assume that the local field in the grain is simply the applied field, E, scaled by a positive random scalar, κ, such that $E_{local}=\kappa E$, where $0<\kappa<\infty$ with a probability density function (PDF), $g(\kappa)$. Mathematically this is equivalent to a similar scaling of the local E_a,

by a positive random scalar η such that $E_{a,local} = \eta E_a$, with a different PDF, $f(\eta)$ [24]. We adopt here the latter approach and we introduce an offset E-field, E_{off}, to allow for possible interfacial charges, to modify equation (3-3) as follows:

$$\tau(E,\eta) = \tau_0 e^{\left(\frac{\eta E_a}{|E-E_{off}|}\right)^{\alpha}} \tag{3-8}$$

Therefore, for an ensemble of grains with a statistical distribution of $\tau(E,\eta)$ and introducing equation (3-8) in (3-5), equation (3-2) becomes:

$$P(t) = -P_S + 2\int_0^{\infty} P_g\left(t,\tau_{gs}\right) f(\eta) d\eta \tag{3-9}$$

Here, $P_g = P_S p(t,\tau_{gs})$ is the local grain polarization areal density, and $f(\eta)$ is a probability density function (PDF) defined in $0<\eta<\infty$ [24]. We have found that different functional forms of $f(\eta)$, e.g., beta-distribution [21], double-sided Gaussian, Lorentzian, or high modulus Weibull PDF, can be fitted reasonably well to measured data. We note that for $f(\eta)$ given by a delta-function, $\delta(1)$, the model reverts to the K-A-I formulation.

3.3.2 NLS Model – Variable Electric Field

Similar to equation (3-2), (3-9) is obtained from integration of (3-7) over time t only if τ, given by equation (3-8), is constant during the integration period. This is indeed the case in many single, constant amplitude voltage step or pulse experiments that are used to verify and parametrize the equations [e.g. [17, 19, 20], [21]] and in which the electric field E is presumably constant after switching. However, when E is a function of time, as in the case of more realistic voltage drives or of significant circuit RC delays, the problem must be solved by looking at the instantaneous incremental change of $P(t)$. This has been done well by a Monte Carlo method in [24]. However, the finite difference approach in [22] is mathematically incorrect because it starts from equation

(3-9) which is invalid for non-constant $E(t)$, as already discussed. On the other hand, the approach in [23], while effectively starting correctly from a form of equation (3-7), it uses the instantaneous $\tau(E(t),\eta)$ instead of τ_{gs} and therefore fails to account properly for the incubation time in pulse waveforms that do not change polarity, as in the case of pulse trains discussed below.[3]

While the Monte Carlo method is appropriate for exploring the statistical nature of the NLS model, it is not suitably efficient for circuit simulation, and therefore the model formulation described below, which lends itself to numerical solution by finite-difference method (see Appendix A) is preferable. We start with the localized polarization density in each individual grain, which is characterized by a specific value of η, denoted as $P_g(t,\eta)$. Then, equation (3-7) becomes:

$$\frac{dP_g(t,E(t),\eta)}{dt} = \frac{sP_s - P_g(t,E(t),\eta)}{\tau_{gs}} \tag{3-10}$$

where,

$$\tau_{gs} = \frac{\tau(E(t),\eta)^{\beta}}{\beta T_{inc}(t)^{\beta-1}} \tag{3-11}$$

Integrating equation (3-10), the total film polarization density including the inter-grain statistical variation of local E_a is now expressed as follows:

$$P(t) = P(0) + \int_0^{\infty} f(\eta) \int_0^{t} \frac{sP_s - P_g(t',E,\eta)}{\tau_{gs}} dt' d\eta \tag{3-12}$$

where $P(0)$ is the known initial value of P, e.g. $-P_S$. It is clear that the second integral in equation (3-12), i.e., equation (3-10), cannot be carried out analytically because now with time-varying $E(t)$, τ_{gs} is time-dependent. However, equation (3-10) can be integrated numerically to compute $P_g(t,\eta)$ with no restriction that τ be constant with time. Equation (3-12) can then be computed numerically

[3]There also appears to be an inconsistency with K-A-I theory in [23], in that the power of β should apply to the $1/\tau$ term inside the integral of eq. (3) of that paper and not to the whole integral.

to provide a discrete time approximation to $P(t)$, and this is the basis of the efficient full-circuit simulation of switching FE capacitors implemented here.

Note that, since typically $\beta \neq 1$, the exact relation of the incubation time, T_{inc}, to elapsed time t, $T_{inc}(t)$, is critical for establishing the correct value of τ_{gs} at any one time. As already discussed, for a single step E-field at $t=0$ T_{inc} accumulates continuously, with $T_{inc}=t$, and the (numerical) solution is straightforward. However, depending on the driving waveform, T_{inc} is known to partially relax towards zero prior to any particular segment of the driving waveform [e.g., [24]], which in turn affects τ_{gs} in that segment.

To illustrate the issues involved in the dynamic behavior of the incubation time, consider a classic experiment, as in [24], in which an FE capacitor is driven by a train of sequential voltage pulses of equal duration and amplitude between $V_{min}=0$ and some positive value, $V_{max}>0$. Assuming starting from negative poling at $-P_S$, the polarization density increases during each pulse, but pauses between pulses. The evolution of accumulated incubation time during the paused-polarization-change interval determines the value of τ_{gs} at the beginning of the next pulse. It might be tempting to assume that T_{inc} is equal to the elapsed time since the beginning of the pulse train, but this is rather unphysical. For the typical $\beta>1$ case, this would make the grain switching critical time, τ_{gs} according to the equation (3-6), increasingly shorter as time progresses and potentially approaching zero as the paused polarization-change intervals increase. However, it is possible that T_{inc} relaxes towards zero soon as a pause is initiated. In some experiments, it is found that the accumulated polarization after sequential pulses is independent of the inter-pulse interval [48] but in other experiments [24] it is found to be dependent on this time interval. A rapid relaxation of

T_{inc} to zero in a time scale shorter than the pause interval would explain the first, while a relatively slow relaxation would explain the latter.

In order to capture this phenomenon, we introduce a *paused incubation-time relaxation* model. Defining t_p as the *pausing time*, i.e., the real time at which the incremental polarization paused, and the incubation time at $t=t_p$ as $T_{inc,p}= T_{inc}(t_p)$, we model the accumulated incubation time for $t>t_p$ as:

$$T_{inc}(t-t_p) = \gamma(t-t_p)T_{inc,p} \tag{3-13}$$

where $0 \leq \gamma(t-t_p) \leq 1$. While the physics behind the behavior of this incubation-time relaxation parameter is not clear, intuitive inspection of available experimental data suggests that $\gamma(t)$ must be a function relaxing from 1 at $t=t_p$ to 0 at $t=\infty$, with a relaxation time, τ_p, that very likely depends strongly on the specifics of the FE capacitor fabrication. We have introduced a simple empirical model for $\gamma(t-t_p)$ as follows:

$$d\gamma/dt = -\gamma/\tau_p \tag{3-14}$$

Detailed comparison with the experimental data in ref. [24] suggests that, at least in that case, τ_p itself is a function of time. The data are best fitted by using the following empirical expression:

$$\tau_p = \tau_{p,0}(1 - e^{-(t-t_p)/k_p}) \tag{3-15}$$

It is clear that in order to fit experiments that show accumulated polarization independent of the inter-pulse time interval [e.g., [48]], $\tau_{p,0}$ must be made significantly shorter than that interval.

Equations (3-8), (3-10), (3-11), and (3-12) constitute the core ensemble-NLS model with equations (3-13), (3-14), and (3-15) controlling the incubation time evolution. A sketch of the finite-

difference solution in discrete time of the equations that describe the FD-NLS morel implemented here, is shown in Appendix A.

3.3.3 FD-NLS Model vs. Measurements

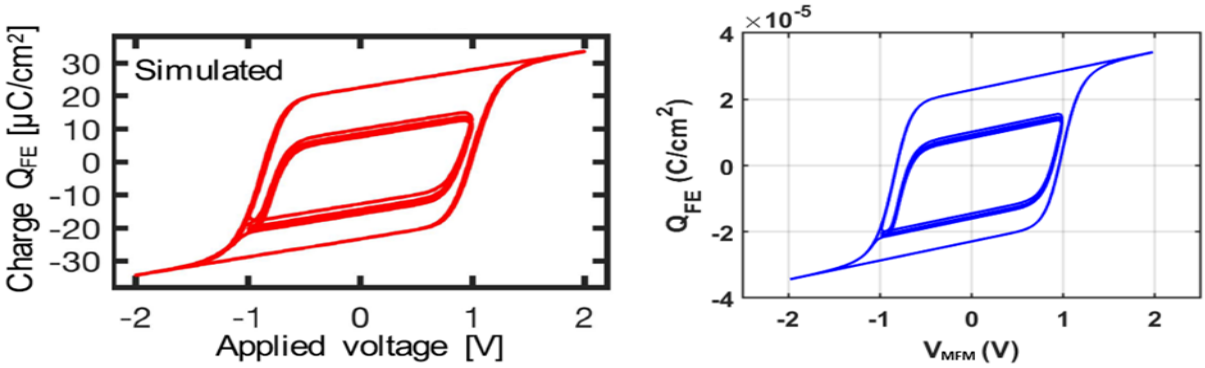

Fig. 3-5. FD-NLS model (right) calculated Q-V loops resulting from a t_{FE}=8.3 nm HZO capacitor subjected to triangular waveform drive against Fig. 4a of ref. [24] (left). Model parameters very similar to those in [16]: P_S=22.9 $\mu C/cm^2$, τ_0=387 ns, α=4.11, β=2.07, E_a=1.73 MV/cm, V_{off}=E_{off}/t_{FE}= 0.07 V. GB2 function parameters [24]: a=12.1, b=1, p=0.633, q=0.690. Incubation time model parameters $\tau_{p,0}$=25.5 μs, and k_p=1,6 μs.

In what follows we present applications of the new Finite Difference NLS (FD-NLS) model implementation in two instances. Formal optimization of the NLS model parameters is discussed in Appendix B.

First, we compare results from the FD-NLS model against those from the discrete-grain Monte Carlo implementation (MC-NLS) of [24], which correctly implements the NLS model for time-dependent E-field cases.

Using model parameters very close to those of that paper, the FD-NLS calculated major and minor Q-V loops in Fig. 3-5 match very closely the measured and simulated Q-V loops shown in Fig. 4b of [24].

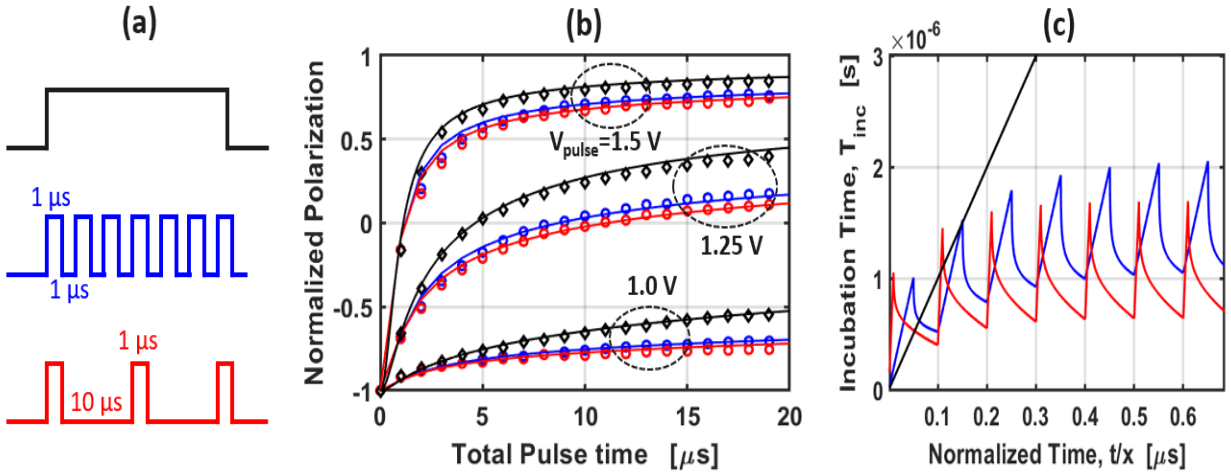

Fig. 3-6. (a) Pulse scheme of each measurement. Single voltage step at t=0 (black), pulse train of twenty 1 µs pulses with 1 µs separation (blue), and train of twenty 1 µs pulses with 10 us separation (red). (b) Normalized polarization, $P(t)/|P_S|$ waveforms vs. total accumulated poling time at three voltage amplitudes, 1, 1.25, and 1.5 V. Colors correspond to the applied pulse schemes in (a). FD-NLS model (lines) and experimental data points from [24]. The parameters for the incubation relaxation model, $\gamma(t\text{-}t_p)$, in equations (3-13) and (3-14), are: $\tau_{p,0}$=25.5 µs, and k_p=1.6 µs. (c) Incubation time vs. normalized elapsed time for selected early part of the waveforms corresponding to simulations shown in (b). Time normalization constant, x = 1 (black), 2 (blue) and 11 (red).

Furthermore, Fig. 3-6 (b) shows the FD-NLS simulated normalized polarization of the experiment in Fig. 5 of [24] with a set of poling pulses with three different voltage amplitudes and equal accumulated poling time (x-axis) but with different paused-poling intervals as sketched in Fig. 3-6 (a). We have studied this experiment because it exercises the proposed incubation-time relaxation model. The FD-NLS model matches the experimental data as well as the MC-NLS model, but this is accomplished with a single dynamic model of $\gamma(t)$ for all experiments, as opposed to [24] where an equivalent *history parameter* is independently adjusted for the different driving voltage waveforms. Fig. 3-6 (c) shows the evolution of the incubation time, T_{inc}, for the three different voltage drives. For a single voltage step at t=0, T_{inc} increases linearly with time. For the pulse-train drive waveforms, the partial relaxation of T_{inc} according to the model for $\gamma(t\text{-}t_p)$ can be clearly seen.

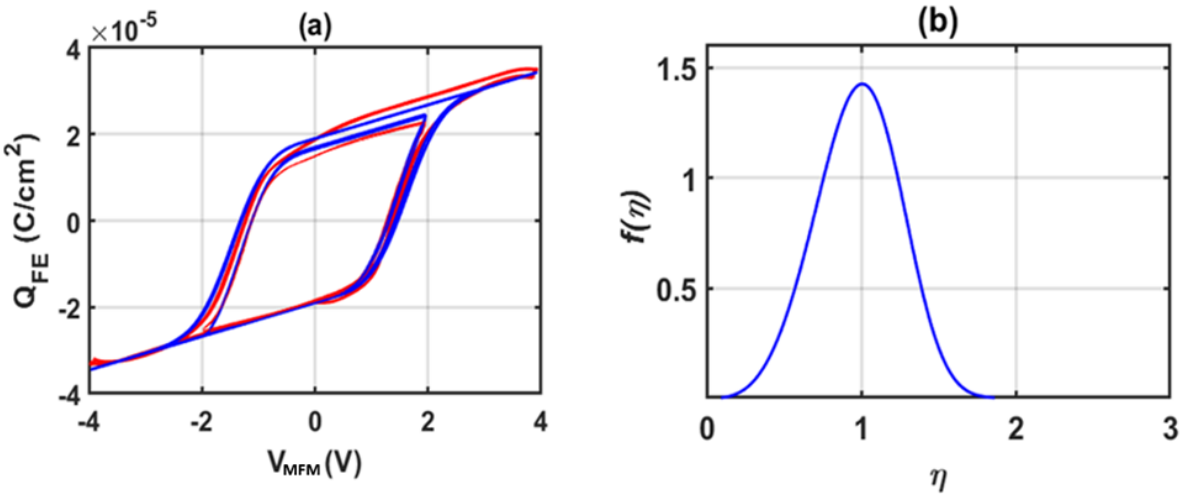

Fig. 3-7. (a) Comparison of measured (red) and modeled (blue) Q_{FE}-V_{MFM} for triangular waveforms with amplitude and frequencies of 4 V, 12.5 MHz (large loop) and 2 V, 500 kHz (small loop). (b) Extracted $f(\eta)$ is represented by a Weibull PDF with shape parameter 4.05, and scale parameter 1.08. Model parameters: P_S=*19* μC/cm^2, τ_0=3 ns, α=8, β=2, E_a=1.7 MV/cm, $\tau_{p,0}$=30 μs, and k_p=1 μs. The FE capacitor consisted of 400 μm^2, TiN-electrode, 10 nm HZO MFM capacitor.

We have further applied the FD-NLS model to our own experimental data obtained from TiN-electrode MFM devices using Setup 2. We drive the simulator with the measured ramped bipolar pulse driving voltage waveform at different frequencies as obtained in our well-calibrated test circuit described in Section 2.2. We also fit triangular waveform Q_{FE}-V_{MFM} hysteresis loops to calibrate the model parameters and $f(\eta)$.

Although hand-optimized in this case, multiple trials have verified that the resulting optimization solution was unique. Fig. 3-7 (a) shows two examples of good agreement between simulated and extracted Q_{FE} -V_{MFM} loops at the extreme ends of voltage and frequency range of this experiment. Fig. 3-7 (b) shows the extracted $f(\eta)$ and the caption gives the optimized model parameters. Fig. 3-8 shows, as expected, excellent agreement between simulated and directly measured current in these experiments down to a scale of 10 ns.

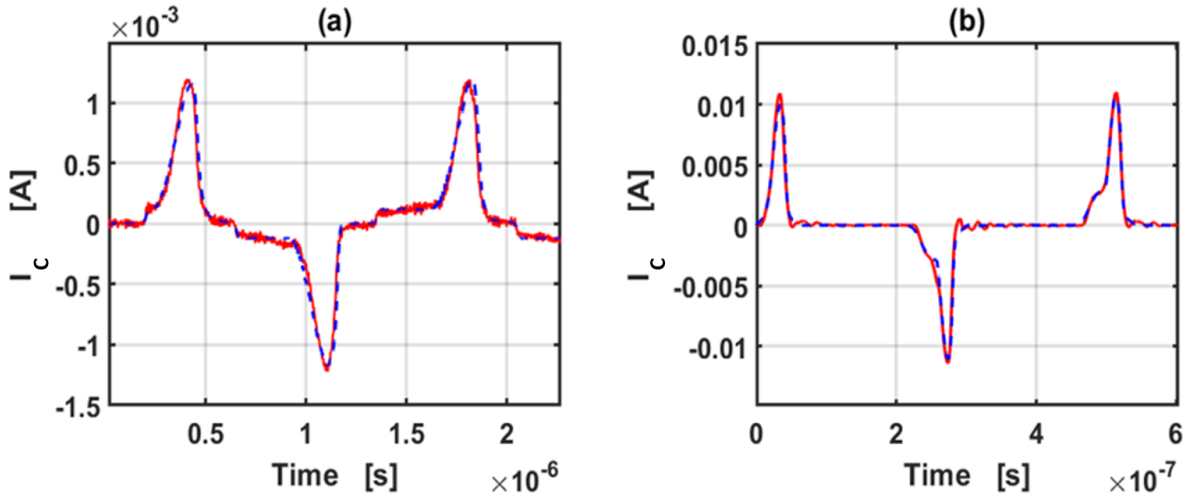

Fig. 3-8. Directly measured (solid lines) and simulated (dashes) currents for bipolar voltage pulses of, (a) amplitude 2 V with ramp rate 62.5 ns/V, and (b) amplitude 4 V with ramp rate 5 ns/V. Same FE capacitor as in Fig. 3-7.

3.3.4 Importance of Accurate Incubation Time

Now, we will demonstrate the significance of accurate incubation time by comparing simulation data obtained under different assumptions regarding the incubation time. In Fig. 3-6, we present the results of our proposed incubation-time relaxation model, which precisely replicates the experimental data across various paused-poling intervals. Although the model is defined by equations (3-12), (3-13), and (3-14), it is worth exploring more intuitive approaches to simulate FE dynamics. Here are two additional cases that can be considered:

Case A: $T_{inc} = t$

Case B: Assumed T_{inc} fully reset to 0 when P(t) pauses.

By applying the above considerations for T_{inc} in the FD-NLS model, we investigate the degree to which an accurate incubation time is crucial in implementing a FE dynamic model.

Fig. 3-9 displays the comparison of normalized P vs. total pulse time (left) between measurement data and modeled data with the incubation time function of Case A. Contrary to measurements the modeled polarization response in this case increases with increasing inter-pulse time interval. As shown in T_{inc} vs. normalized time (right), T_{inc} increases linearly with elapsed time and it results in *underestimation* of τ_{gs} according to equation (3-10). Consequently, the smaller τ_{gs} leads to overestimation of cumulative polarization through equation (3-11). As a result, the longer separation between pulses causes a faster switching rate vs. total pulse time, which is the opposite of what is observed in the actual measurements, as depicted in Fig. 3-9.

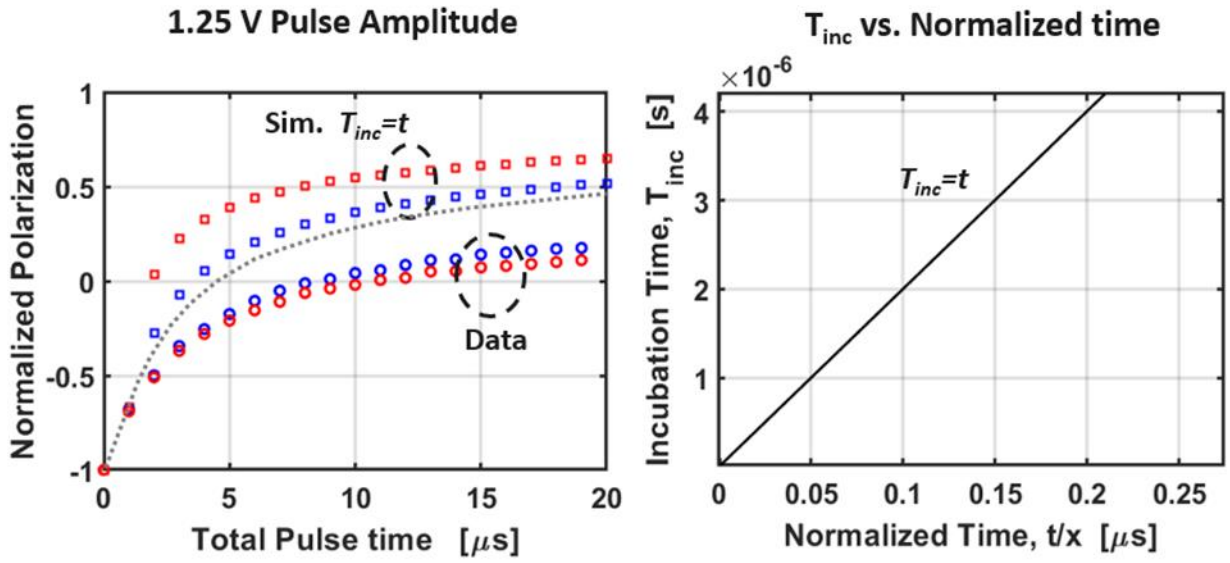

Fig. 3-9. Comparison of normalized polarization vs. total accumulated poling time at 1.25V between measured data (circles, from Fig. 3-6) and modeled data with T_{inc} = t (squares) (left). Colors indicate different pulse separations, as described in Fig. 3-6. Gray dashed line corresponds to measured data with 0 s separation. With an assumption of T_{inc} = t, T_{inc} keeps increasing with elapsed time (right).

We also evaluated the simulation of FE dynamics using Case B, as depicted in Fig. 3-10. In this case, T_{inc} is reset to 0 abruptly when V(t) reaches 0 (right). However, this resetting of T_{inc} causes an *overestimation* of τ_{gs}, leading to an underestimation of cumulative polarization. As a result, the

simulated data shows lower polarization switching reversal compared to the measured data (Fig. 3-10, left).

Furthermore, with Case B, τ_{gs} always becomes infinite after a single pulse, which disregards the effect of the length of pulse separation. Consequently, contrary to measurements, the simulation results exhibit identical FE switching dynamics vs. total pulse length regardless of the pulse interval (left). This failure to account for the difference in inter-pulse time interval leads to inaccurate prediction of FE device dynamics.

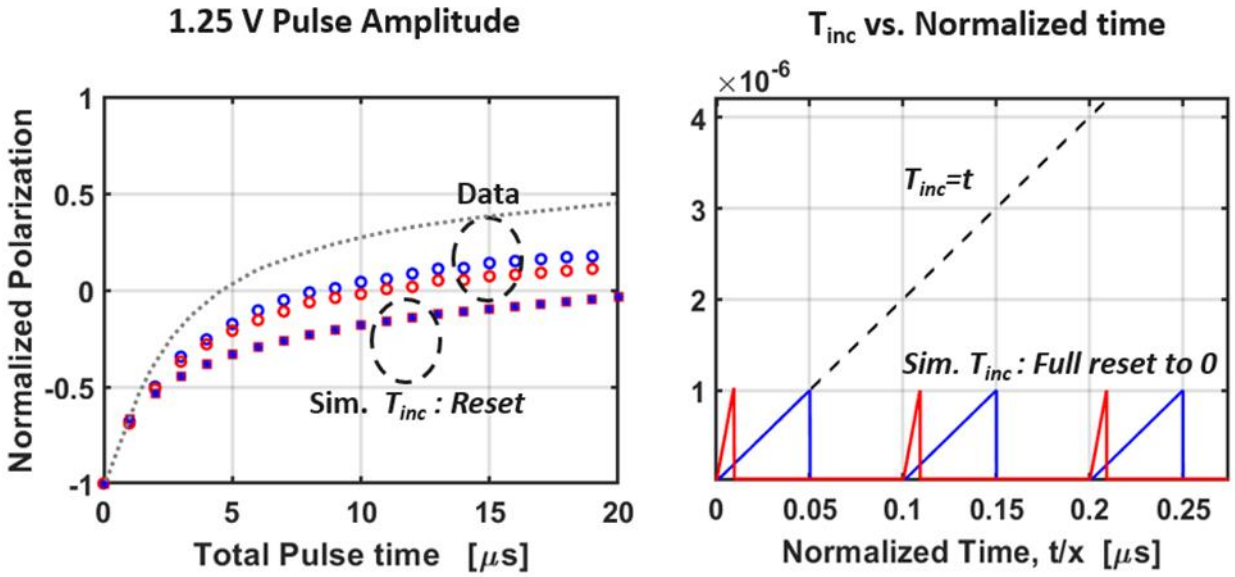

Fig. 3-10. Comparison of normalized polarization vs. total accumulated poling time at 1.25V between measured data (circles, from Fig. 3-6) and modeled data with an assumption that T_{inc} is reset when P(t) pauses (squares) (left). Colors indicate different pulse separations, as described in Fig. 3-6. Gray dashed line corresponds to measured data with 0 s separation. With an assumption of T_{inc} fully reset to 0 when P(t) pauses, T_{inc} is always same for individual pulses regardless of the pulse interval (right).

3.4 Summary

In this chapter, we have described experimental results of MFM dynamics using accurately calibrated setups. We have also introduced the FD-NLS model through a rigorous formulation.

Under a broad range of conditions, the MFM response of an R-MFM circuit only displays a typical FE hysteretic response instead of a transient NC effect. This is also found to be consistent with the results obtained in a simple resistor-free MFM circuit. This calls into question earlier claims of NC switching observations which could perhaps be explained by improperly calibrated experimental setups or sample parasitic extraction.

We have shown a mathematical reformulation of the NLS model that lends itself to efficient and accurate computation of FE capacitor switching for arbitrary driving voltage waveforms. The new model has been implemented using a finite difference numerical solution and was verified with switching experiments with different FE films and different driving excitations. Furthermore, a new model capturing relaxation of the NLS incubation time during periods of switching inactivity has been introduced. The full FD-NLS model enables accurate circuit simulations over a broad range of time scales and the incubation time relaxation model allows simulation of sequential voltage pulse drives that are of interest for AI hardware applications.

Chapter 4 Imprint Effect in FE-HZO

4.1 Introduction

Although imprint is one of the most serious degradation effects in FE materials, its root cause is still unclear. Several potential origins of the imprint have been proposed relying on the assumption of the existence of a spontaneous depolarization E-field in the FE material at 0 V. Such a depolarization field arises whenever the intrinsic FE surface (polarization) charges are physically separated from the extrinsic compensating (screening) charges. According to theory, this physical spatial separation may be due to the presence of a non-FE layer (dead layer) at the interface between the nominally FE material and an ideally screening metal electrode [33] or to the imperfect screening of FE polarization charges at the metal surface [49]. Of course, a combination of the two effects would also result in a depolarization field. With this assertion, the proposed models can be categorized by following three different stimuli of the imprint effect: 1) redistribution of mobile charges [25, 26, 27, 28, 29, 30, 31], defect dipole polarization [32], and charge trapping and de-trapping at a non-FE interfacial layer between oxide and metal [33, 34, 35]. However, after careful experimentation during the course of this thesis none of these models can explain every observation.

In this chapter, we provide a comprehensive summary of the imprint effect and its recovery behavior through extensive electrical measurements. Additionally, we evaluate the existing models proposed in the literature by applying them to our observations.

4.2 Characterization of Imprint Behavior

This section shows electrical measurement schemes designed for imprint studies. Then, we present a detailed examination of imprint behavior, offering a comprehensive analysis and insights into the imprint phenomenon that have not been previously explored. Mainly W-electrode 10-nm FE-HZO MFM capacitors, as described in Chapter 2, have been measured using Setup 2 to characterize imprint behavior.

4.2.1 Voltage Pulse Schemes

In this section, we define voltage pulse schemes and provide detailed pulse information. Based on the information in this section, various pulse measurement schemes in the following sections will be introduced in a simple manner.

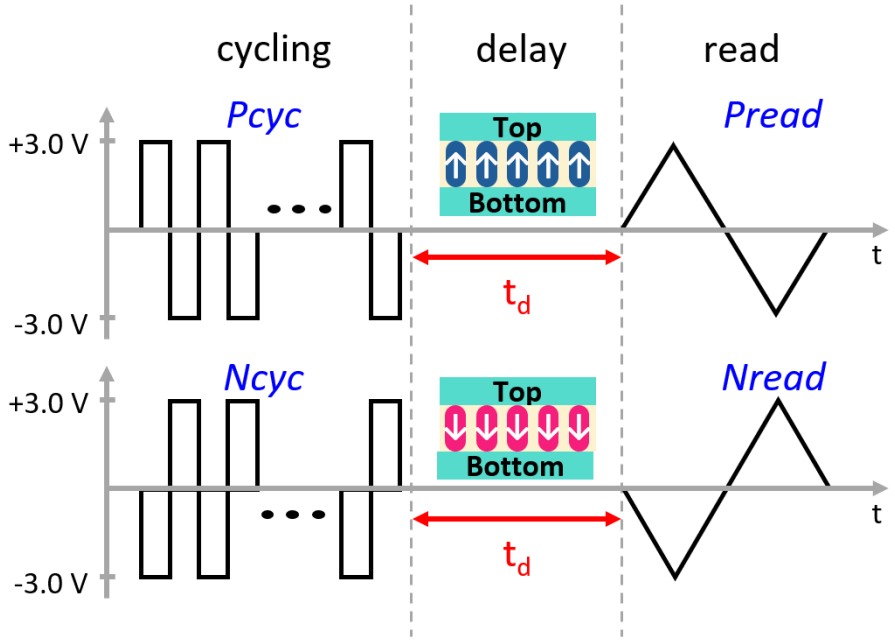

Fig. 4-1. Basic voltage pulse scheme to observe imprint effect.

Fig. 4-1 shows a ‘basic’ voltage pulse scheme to observe imprint effect, consisting of three parts, cycling, delay, and read. Throughout this thesis the voltage reference is at the bottom electrode. ‘Cycling’ is an initialization process using electric field cycling to erase the FE history of the sample. This is a pulse train of 3000 cycles of a ±3.0 V bipolar trapezoidal pulse 500 ns wide and rise/fall times of 40 ns. ‘Pcyc’ denotes that the pulse starts with a positive trapezoidal half pulse and finishes with a negative trapezoidal half pulse and finally sets the FE polarization to P_{up}=-P_r, i.e., negative. ‘Ncyc’ is inverse to ‘Pcyc’ and sets P_{down}=P_r, which is positive. ‘Delay’ (t_d) is the time duration at 0 V, or later in this chapter at a specific finite voltage, during which MFM structures experience the imprint depending on their polarization state.

After the delay period during which imprint takes place, its effect can only be observed during subsequent FE switching using a triangular bipolar waveform. This is the “read” period. The measurement of the coercive voltage (V_C) shift is a suitable measure of imprint. For this approach to be successful, it is essential to employ a read pulse capable of switching all domains. ‘Pread’ corresponds to a ±3.0 V triangular waveform at 100 kHz and starts with a positive half triangular waveform that can monitor a shift in the positive coercive voltage (V_{C+}). ‘Nread’ is for negative coercive voltage (V_{C-}) shift observations.

Therefore, Fig. 4-1 can be simply expressed by ‘Pcyc-delay-Pread’ and ‘Ncyc-delay-Nread’ if no additional details are provided. Henceforth, pulse measurement schemes will be expressed using this notation.

4.2.2 Basic Imprint Effect at Room Temperature

Fig. 4-2 shows the basic imprint effect at room temperature. To observe the dependence of FE polarization direction, two opposite pulse schemes, Pcyc-delay-Pread (blue) and Ncyc-delay-Nread (orange), were applied to a 370-μm^2 area MFM capacitor under different delay time (t_d). The data shown in Fig. 4-2 corresponds to the results from Pread in Pcyc-delay-Pread (blue) and Nread in Ncyc-delay-Nread (orange) sequences.

As t_d increases, the Q_{FE}-V_{MFM} loop continuously shifts in a certain direction depending on the stored polarization direction. The magnitude of the loop shift can be quantified by coercive voltage shift (ΔV_C), and that is found to increase linearly increased with log t_d similar to other literature [25, 31]. In our samples, a significant imprint effect is observed when $t_d > 1$ μs. ΔV_{C+} and ΔV_{C-} vs. t_d curves using Pcyc (ΔV_{C+}) and Ncyc (ΔV_{C-}) show nearly mirror characteristics, with 0.52 V and -0.49 V at t_d = 100 s respectively reflecting a slight asymmetry of the MFM structure. Furthermore, the coercive voltage shifts of the ascending and descending parts of the Q-V loops in positive or negative polarization imprints are not the same, as further illustrated by the displacement of the peak currents in the instantaneous i_C vs. V_{MFM} plot in Fig. 4-2 (right) that corresponds to the blue Q-V loop (positive polarization imprint), where clearly $|\Delta V_{C+}| > |\Delta V_{C-}|$. This observation leads to the conclusion that the domains have a preferable switching direction during the imprint. Additionally, although not clearly observable in this plot, the direction of ΔV_{C+} and ΔV_{C-} is the same, i.e., both shift to the right with increasing t_d. This suggests that, depending on the polarization, the inhibition of nucleation for FE switching at the interface between one of the metal electrodes and the FE-HZO may be serving as the underlying cause of the imprint effect,

as per the NLS theory. Furthermore, it is noted that there was no significant difference in the imprint effect whether forcing 0 V or disconnecting the probe during the delay stage.

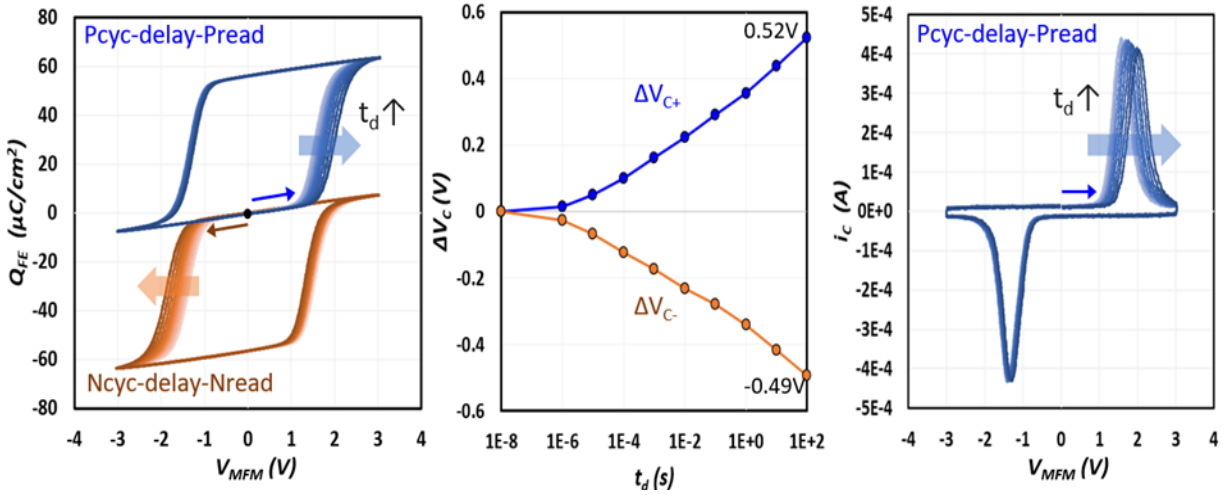

Fig. 4-2. Basic imprint behavior of a 370-μm^2 area MFM capacitor with different t_d using Pcyc-delay-Pread (blue) and Ncyc-delay-Nread (orange). Extracted Q_{FE} vs. V_{MFM} (left plot). ΔV_C vs. t_d (center plot). Measured instantaneous i_C vs. V_{MFM} (right) from Pread after Pcyc-delay.

4.2.3 Temperature Dependence

The imprint effect exhibits a temperature dependence. Fig. 4-3 shows that the imprint effect is enhanced with temperature in Pcyc-delay-Pread experiment. As shown in the left figure, ΔV_{C+} is increased as temperature increases.

On the right figure, ΔV_{C-} represents the negative coercive voltages of positively shifted charge-voltage loops in the Pcyc-delay-Pread experiment (i.e., descending parts of Pread). Interestingly, V_{C-} shift in the positive direction also increases with temperature. This similar ΔV_C tendency of V_{C+} and V_{C-} with temperature suggests that a root cause of the imprint effect may exist at both interfaces of the MFM capacitor, but the asymmetric impact may potentially stem from the stored polarization direction or the voltage most recently applied.

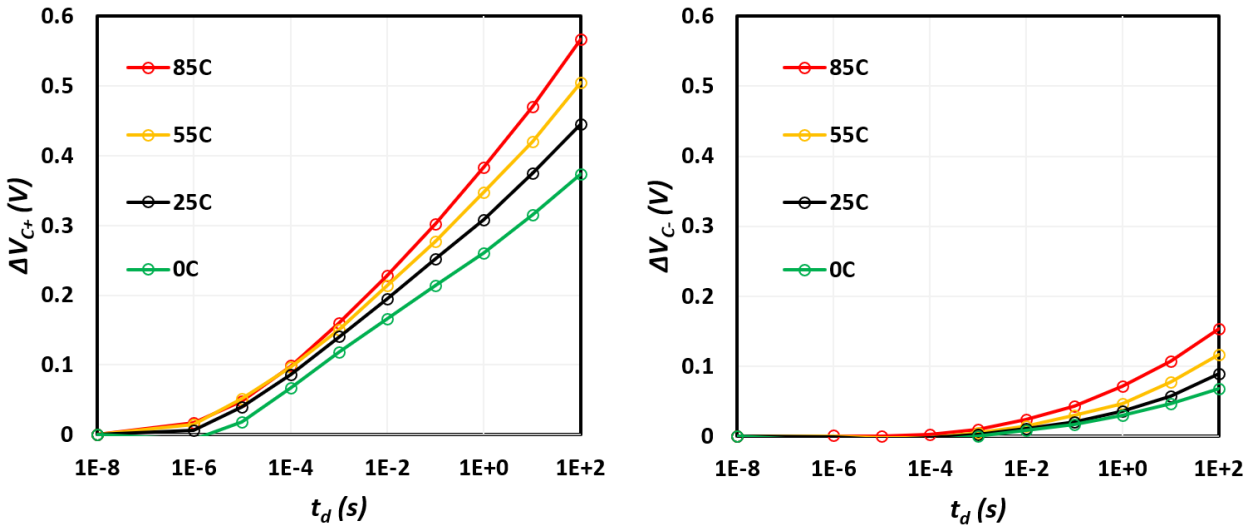

Fig. 4-3. Imprint behavior of 90-μm^2 area MFM capacitors with different t_d using Pcyc-delay-Pread at different temperatures. Extracted ΔV_{C+} vs. t_d (left) and ΔV_{C-} vs. t_d (right).

4.2.4 Remanent Polarization Dependence

As mentioned in Section 4.1, it is generally believed that the existence of an internal electric field with the sample at rest is at the root cause for imprint. According to some models [25, 28, 29], the depolarization field strength is determined by remanent polarization (P_r) of the FE material. As a result, it is believed that the imprint effect is enhanced as P_r increases. Therefore, this section presents the P_r dependence of the imprint effect.

We have carried out a basic imprint measurement, Pcyc-delay-Pread, at room temperature with three different MFM capacitors described in the insets of Fig. 4-4. As shown in the figure, the three capacitors have different P_r values, 28, 21, and 10 μC/cm^2. Identical ALD and sputter tools deposited the HZO and metal layers of all capacitors. Here, since the thicknesses of the capacitors are different, imprint is assessed through the coercive field shift (ΔE_C) instead of ΔV_C.

Fig. 4-4 (a)-(c) shows the typical imprint behavior observed in all stacks. Although P_r differs by a factor of about 3 in these devices, they all exhibit a similar imprint effect as a function of t_d, as manifested by very similar ΔE_{C+} vs. t_d shown in Fig. 4-4 (d). In contrast with the literature [25, 28, 29], no correlation is observed between the remanent polarization and the imprint effect. Hence, we may conclude that the phenomenological models that explain the imprint effect through a depolarization field generated by remanent polarization are inconsistent with our experimental results.

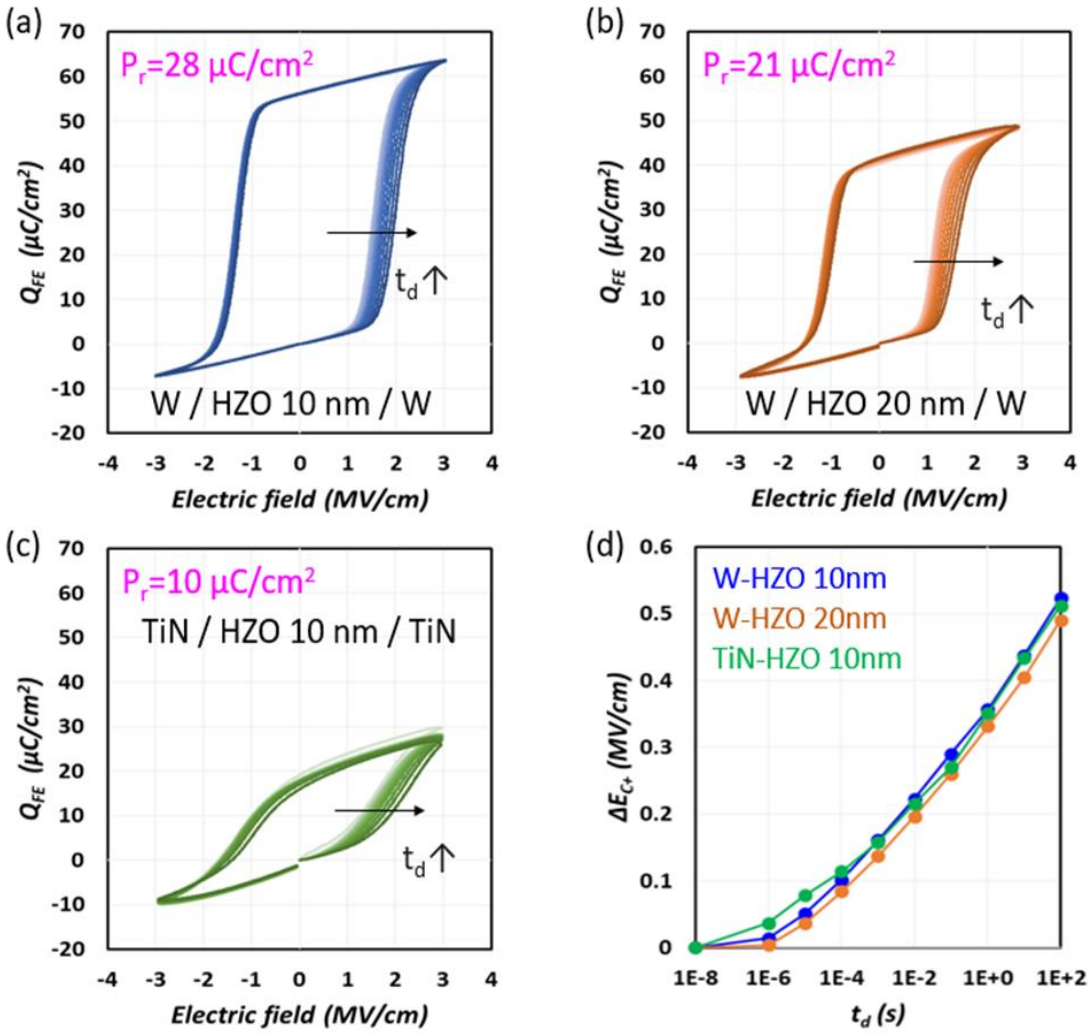

Fig. 4-4. Imprint effect of 370-μm² area MFM capacitors with different P_r. Q_{FE} vs. Electric field with t_d of (a) W-electrode 10-nm FE-HZO, (b) W-electrode 20-nm FE-HZO, and (c) TiN-electrode 10-nm FE-HZO. (d) ΔE_{C+} vs. t_d characteristics of three capacitors.

4.2.5 Frequency Dependence

Despite extensive research on the imprint behavior, the frequency dependence of the read signal has yet to be thoroughly investigated. Fig. 4-5 demonstrates the frequency dependence of Pread in the basic imprint measurement (Pcyc-delay-Pread) using a 370-μm^2 area 10-nm FE-HZO capacitor. The small frequency dispersion in the absence of imprint, i.e., loop width at t_d = 10 ns increases with frequency, originates from the nature of FE switching dynamics, as is well-known [46]. The change of $2P_r$ (vertical loop size) observed at 1 MHz is due to incomplete FE switching with ± 3 V Pread at this frequency. We confirmed that there is no actual change of $2P_r$ when high enough positive voltage was applied to change all domains completely. This will be discussed in more detail in Section 4.3.1.

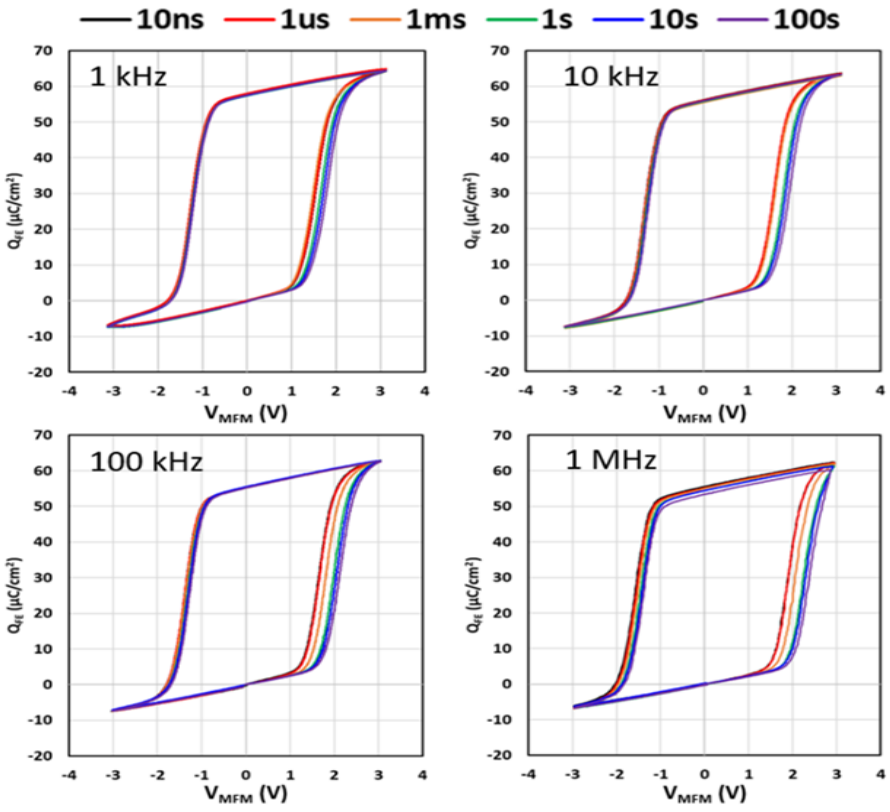

Fig. 4-5. Basic imprint measurement (Pcyc-delay-Pread) of 370-μm^2 area 10-nm FE-HZO capacitor at different t_d. Each graph corresponds to Q_{FE} vs. V_{MFM} from Pread waveforms measured at different frequencies.

At all Pread frequencies, the MFM capacitor presents a typical shift of the Q_{FE} vs. V_{MFM} loop with t_d. The frequency dependence is clearly observed in Fig. 4-6. As the frequency of Pread increases, there is a noticeable increase in ΔV_{C+} with t_d. In fact, with Pread at 1 kHz no significant V_C shift is observed with a delay of up to 1 ms. The frequency dependence of the imprint effect has a linear relationship with log *f* of Pread, as shown in ΔV_{C+} at t_d = 100 s vs. Pread frequency (Fig. 4-6, right). According to the extrapolated result, it is estimated that imprint is extinguished when Pread takes place at 1 Hz. However, validating this estimation is challenging due to the increased influence of leakage current in the measurement at very low frequencies.

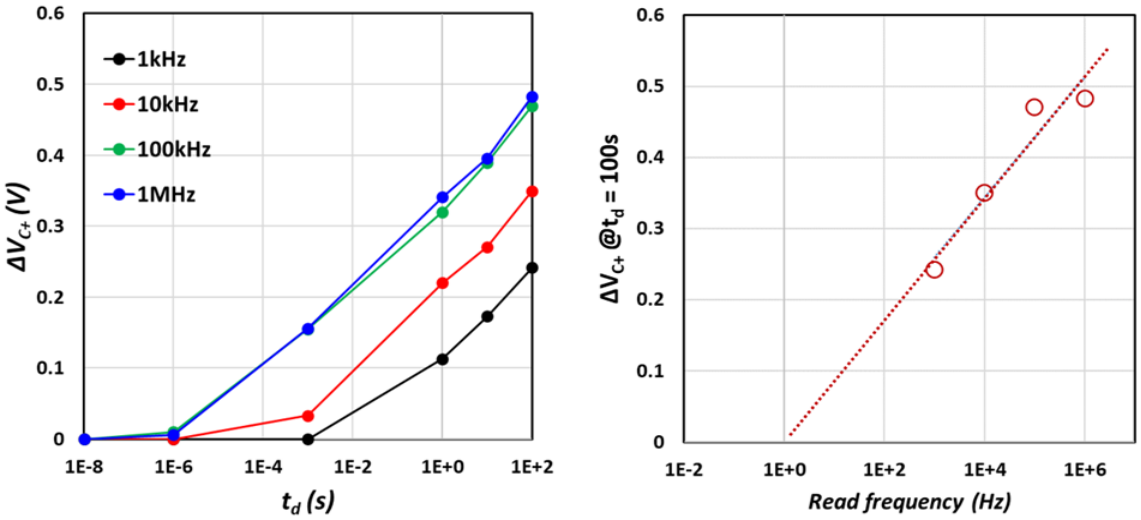

Fig. 4-6. Extracted ΔV_{C+} vs. td at different frequencies of Pread from Fig. 4-5 (left). ΔV_{C+}@t_d=100s vs. Pread frequency (right).

This result also suggests that electron trapping and de-trapping at a possible non-FE interfacial (dead) layer [21, 31] may not play a significant role in the imprint behavior. This is because all measured loops in Fig. 4-5 show the same start and end points and slopes of paraelectric and FE polarization. Theoretically, interface-trapped charges can impact not only the loop shift but also the slope of dP/dV manifested in the loop. If the trapped charge would cause the imprint effect,

there should have been an obvious difference in paraelectric and FE capacitance (slopes in the loops) between different Pread frequencies since they have different amounts of ΔV_{C+}.

4.2.6 Voltage Dependence

In previous sections, 0 V has been applied to MFM capacitors during the delay time to induce the imprint effect. This section presents the results of the imprint effect caused by a non-switching voltage pulse during the delay time, something that has not been previously investigated in the literature. Fig.4-7 displays the pulse measurement scheme for this experiment starting with Pcyc initialization. Completely reversed polarities are used for Ncyc initialization.

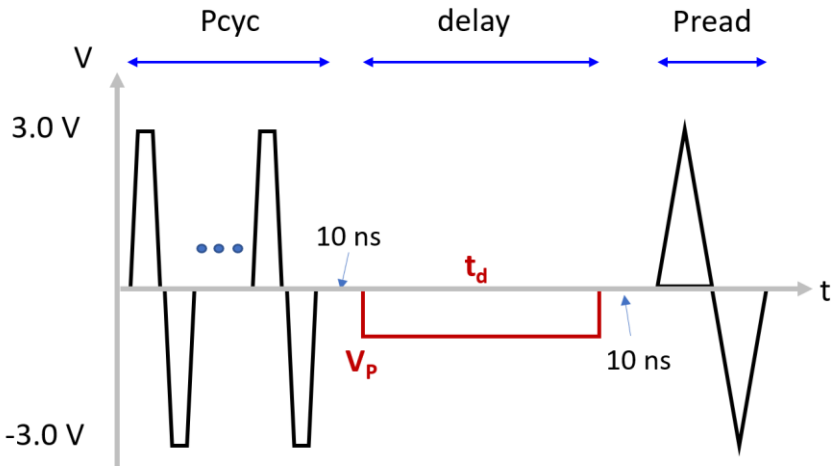

Fig. 4-7. Pcyc-initialization pulse measurement scheme of imprint effect with a non-switching voltage pulse during the delay time. Ncyc-initialization experiments have fully reversed polarity.

After a Pcyc (Ncyc) initialization, a non-FE switching trapezoidal pulse is applied with negative V_p (positive V_p) followed by Pread (Nread). Accordingly, the imprint effect caused by the voltage pulse during the delay is observed in extracted ΔV_{C+} (ΔV_{C-}) from Pread (Nread) respectively. To characterize voltage and time dependence, the applied V_p changes from 0 V to -3 V (+3 V) and t_d varies from 10 µs to 1 s.

Fig. 4-8 shows that the imprint effect ($|\Delta V_C|$) is enhanced as the absolute voltage amplitude present during the imprint delay period increases. The strong voltage dependence of ΔV_C (Fig. 4-8 right) emerges at t_d > 10 µs with a quadratic function showing a good fit error, R^2 > 0.987.

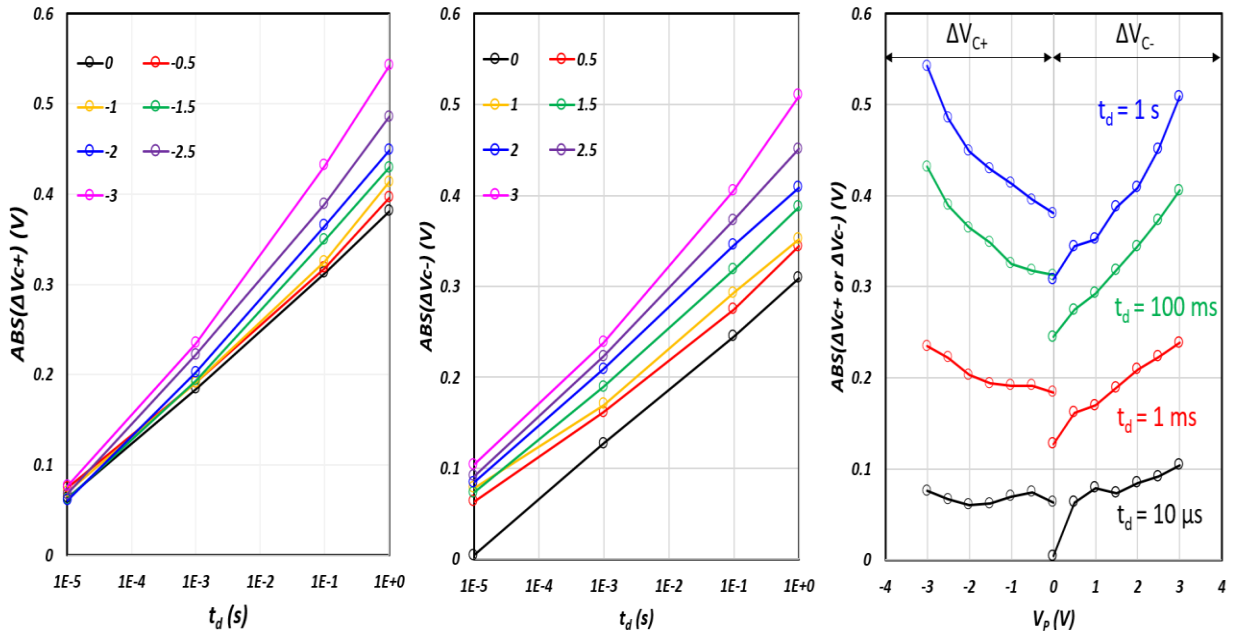

Fig. 4-8. $|\Delta V_{C+}|$ vs. t_d (left) and $|\Delta V_{C-}|$ vs. t_d (center) of 90-µm^2 area 10-nm FE-HZO capacitor after voltage pulse application with V_P (in legend) during imprint. Abs(ΔV_C) vs. V_P (right) with different t_d.

Fig. 4-9 shows the Q_{FE}-V_{MFM} loops after the 1 s imprint pulse with various voltage amplitudes, V_P, in the experiment starting with Pcyc. Similar to the basic imprint behavior, no significant coercive voltage shift is observed from the other side of the loops, i.e., V_C in the descending Q-V branch; and while V_{C+} changes with V_P, V_{C-} shows negligible change. This asymmetric behavior that is accentuated by an external electric field indicates that the imprint effect may primarily change the state of only one interface (where nucleation occurs preferentially) between metal and FE-HZO rather than at both interfaces and the entire bulk of FE-HZO.

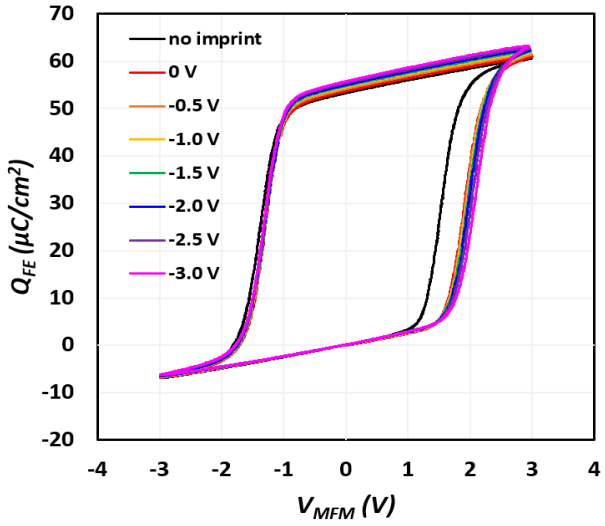

Fig. 4-9. Q_{FE} vs. V_{MFM} loops from Pread after 1 s imprint pulse with various voltage amplitudes, V_P.

We also examine the imprint effect using opposite bias slightly lower than the threshold switching voltage. In other words, positive pulse is applied after Pcyc instead of negative, but the voltage amplitude (V_P) is kept small enough to avoid any significant FE polarization switching reversal. Then, Pread is applied to observe a ΔV_{C+}.

The left figure of Fig. 4-10 shows the Q_{FE} vs. V_{MFM} loops after applying a 0.6 V trapezoidal pulse with different pulse durations, t_d. Although a small amount of switching is observed due to the 0.6 V pulse application, the loops show a typical loop shift. Remarkably, no significant difference from 0 V imprint data is observed, as shown in the right figure of Fig. 4-10.

We have observed that the imprint effect can be accelerated by applying a non-switching external electric field during t_d. This finding suggests that when an electric field is applied in the same direction as the polarization of a ferroelectric domain, it enhances the imprint effect. On the other

hand, applying an electric field in the opposite direction of the polarization has no impact on the imprint effect, indicating that it does not alter the root cause of the imprint effect.

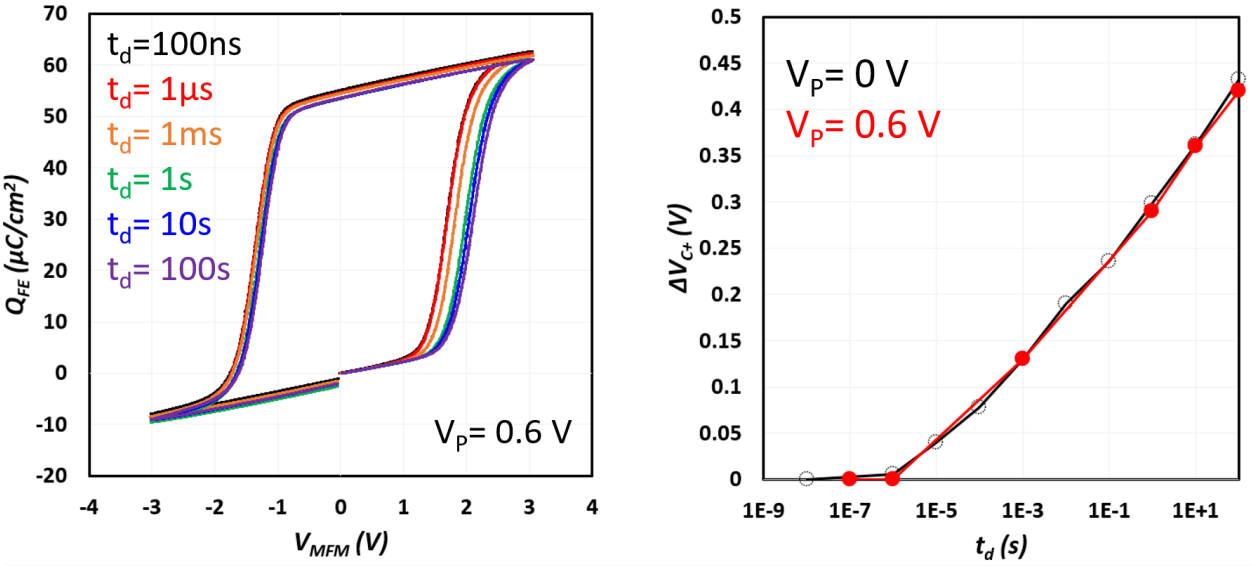

Fig. 4-10. Imprint effect of 370-µm^2 area 10-nm FE-HZO capacitor using Pcyc - +V_P pulse – Pread. Q_{FE} vs. V_{MFM} with different t_d when V_P = 0.6 V (left). Comparison of ΔV_{C+} vs. t_d between V_P = 0 V (black) and V_P = 0.6 V (red) (right).

4.2.7 Cycling Waveform Dependence

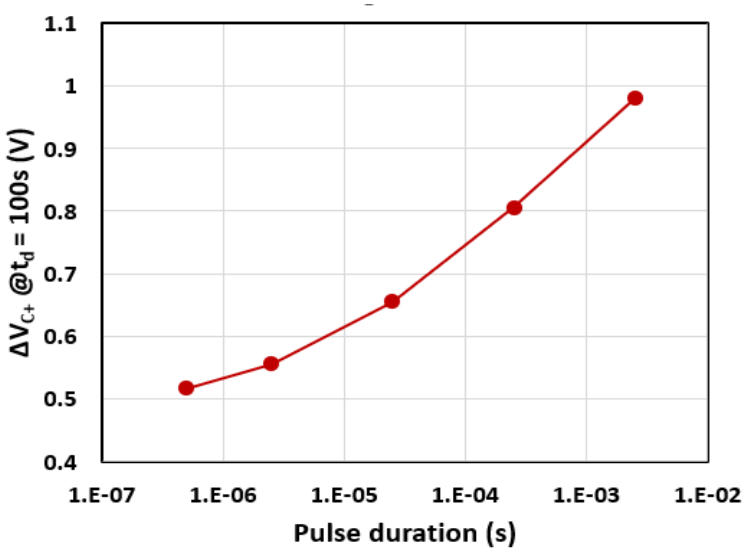

Fig. 4-11. ΔV_{C+} when t_d = 100 s vs. Pcyc duration of a 370-µm^2 area 10-nm FE-HZO capacitor.

To evaluate the impact of defect concentration on the imprint effect, basic imprint measurements, Pcyc-delay (V=0, 100 s) -Pread, have been carried out. After 5 capacitors are woken up, different Pcyc pulse waveforms with same rise/fall times but with various pulse durations, 500 ns, 2.5 µs, 25 µs, 250 µs, and 2.5 ms, are applied to the capacitors, respectively. It is believed that as the exposure time to high voltages during cycling increases, the concentration of oxygen vacancies increases until the device is broken [50].

Fig. 4-11 shows that ΔV_{C+} when t_d = 100 s increases with the high voltage duration of Pcyc. This result indirectly implies that the root cause of imprint effect may be closely related to the concentration of major defects in the FE-HZO system, such as oxygen vacancies.

4.3 Recovery of Imprinted FE-HZO Using Electric Field Cycling

The recovery of imprinted FE domains can be achieved by applying electric field cycling to MFM structures. Indeed, this is the reason for the Pcyc or Ncyc phase of in our experiments. However, very few investigations of the recovery behavior have been published. In this section, we present a comprehensive exploration of various observed recovery characteristics using an accurate pulse measurement setup (Setup 2 in Section 2.2.1). The objective is to gain insights into the underlying cause of the imprint effect.

4.3.1 Recovery Behavior with Cycling

To observe the recovery evolution of imprinted domains in FE-HZO MFM capacitor, the time-domain response of 3000 Pread was recorded, as shown in Fig. 4-12. To increase the V_C shift as much as possible (see Section 4.2.3), two MFM capacitors were annealed at 150 ℃ for 2 hours by

oven to set FE domains imprinted, after standard Pcyc at room temperature. Then, two different sets of 3000 consecutive Pread waveforms with different voltage amplitudes, ±3.0 V and +4.0 V/-3.0 V, were applied to the capacitors respectively. Here, the 3000 cycles of Pread constitute the electric field cycling that serves as the recovery process of imprint.

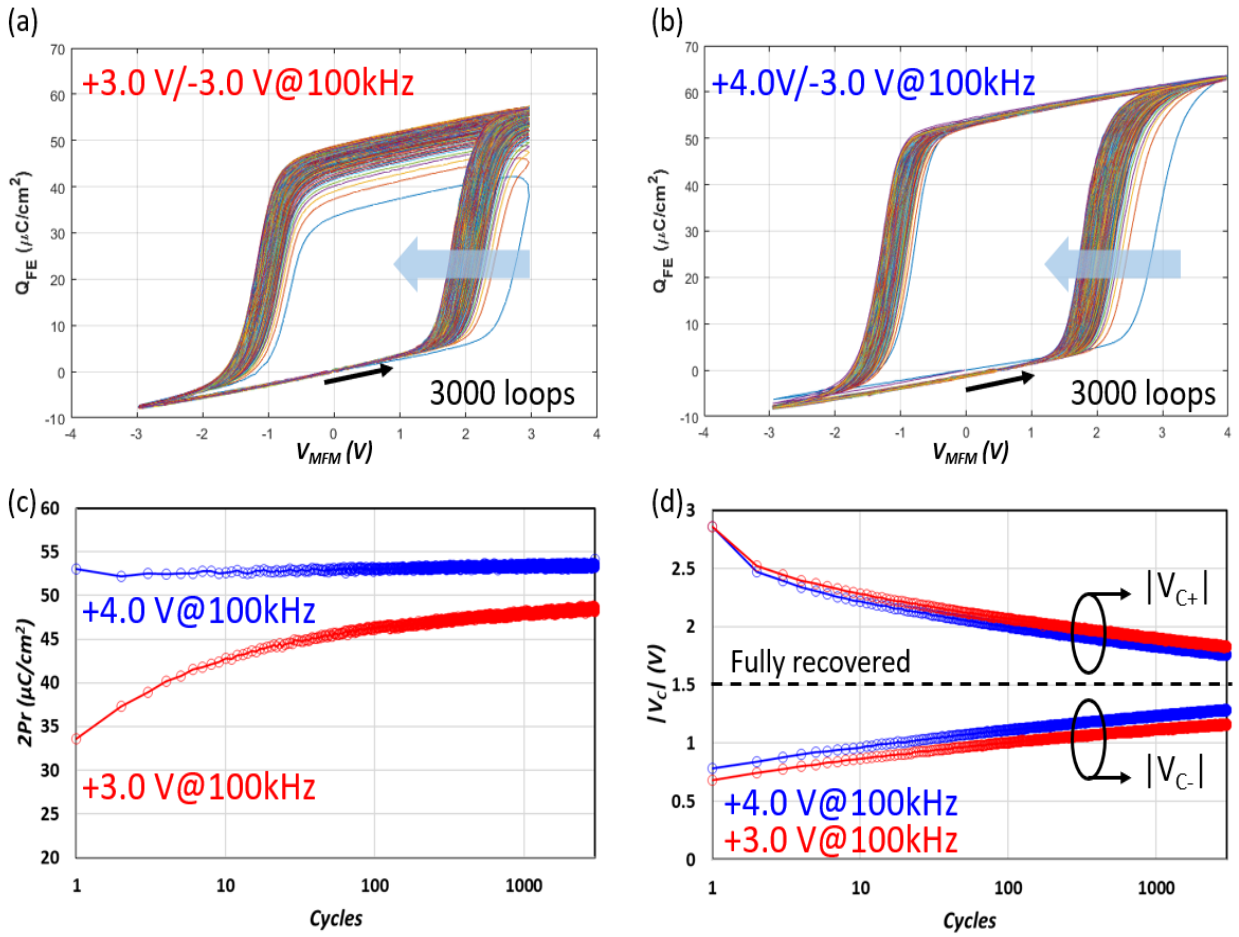

Fig. 4-12. Recovery behavior applying 3000 consecutive Pread waveforms after imprint for 2 hours at 150 °C. (a) Recovery process of 300-μm^2 area FE-HZO MFM capacitor using ±3.0 V Pread, and (b) 360-μm^2 area FE-HZO MFM capacitor using +4.0 V/-3.0 V Pread. (c) Comparison of $2P_r$ vs. recovery cycles between ±3.0 V and +4.0 V/-3.0 V Pread. (d) Evolution of coercive voltages with recovery cycles.

Fig. 4-12 (a) and (b) illustrate the typical recovery behavior observed from the annealed MFM capacitors. Due to the imprint process at elevated temperature for an extended duration (150 °C for 2 hours), both V_{C+} and V_{C-} exhibit a significant shift in the first cycle of the recovery cycles,

as expected in Section 4.2.3. The hysteresis loops gradually become symmetrical as the number of cycles increases. Notably, in the case of Pread at +4.0 V, there is no retention loss (i.e., change of $2P_r$) in contrast with the case of Pread at +3.0 V. This is simply due to excessive shift in V_C which renders the maximum of the Pread waveform insufficient to fully switch the polarization and suggests that (apparent) P_r decrease of imprinted MFM capacitors, often reported in the literature [26] may not be a fundamental effect. Fig. 4-11 (c) clearly demonstrates a constant value of $2P_r$ during the recovery cycles at +4.0 V, but not in the case of +3.0 V of Pread. This is evidence that imprint is not associated with the occurrence of an FE switching event since the stored FE polarization remains unchanged.

Fig. 4-12 (d) shows the evolution of V_C during the recovery as the number of cycles increases. In this figure, V_{C-} corresponds to the negative coercive voltage of each Q_{FE}-V_{MFM} loop in Fig. 4-12 (a) and (b). The significant $|V_C|$ recovery in the first few cycles, recovered about 50 % of total shift in the first 10 cycles, is commonly observed in both cases. Beyond that, the capacitors are recovered with the same recovery rate. This observation means the recovery rate is not accelerated by the voltage amplitude of recovery cycle unlike the voltage dependence of the imprint effect in Section 4.2.5.

4.3.2 Voltage Dependence of Imprint Recovery

This section focuses on the voltage dependence of the recovery behavior. If the rate of recovery exhibits voltage dependence, the extent of loop shift will depend on the voltage amplitude of the recovery cycles. Although the previous section did not show a significantly different recovery rate at 4.0 V compared to that at 3.0 V, we further investigated the voltage dependence of recovery by

examining it at various lower voltage amplitudes. After Pcyc – delay (0 V at room temperature, t_d=100 s), 21 cycles of Pread were applied to the imprinted MFM capacitor, as shown in Fig. 4-13. The voltage amplitude of the triangular waveforms increases from 1.0 V to 3.0 V with a 0.1 V step while ramp rate is kept constant.

From the measured V_{MFM} vs. time and i_C vs. time data, the Q_{FE} vs. V_{MFM} loops are extracted, as depicted in Fig. 4-14. The black line in the figure represents a virgin Q-V loop with no imprint. Interestingly, the imprinted domains show independent recovery behavior, as the recovery voltage amplitude increases. Since the activation field (E_a) of each domain has a distribution according to the Nucleation Limited Switching (NLS) model, only domains with smaller E_a than the applied voltage are recovering. This indicates that the imprint is strongly related to individual domain polarization states.

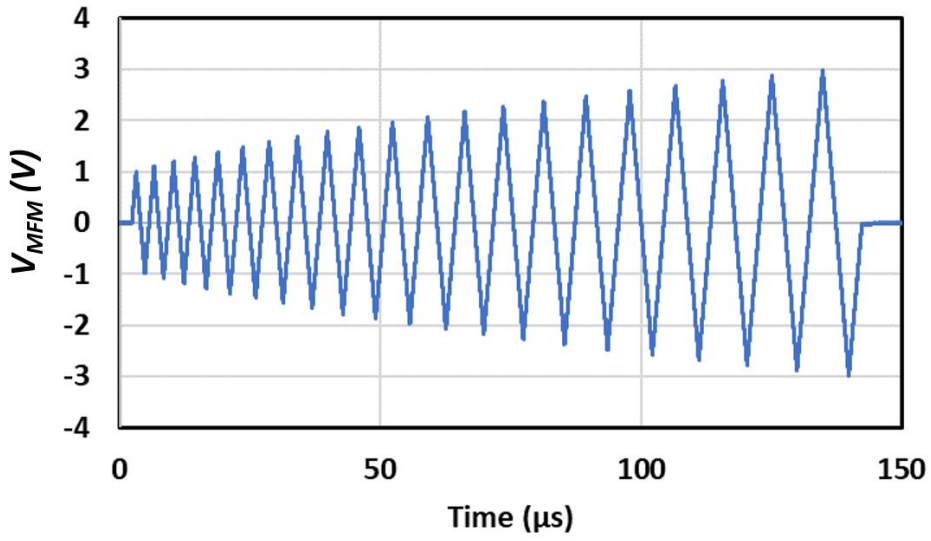

Fig. 4-13. 21 cycles of triangular waveforms to study the voltage dependence of recovery behavior.

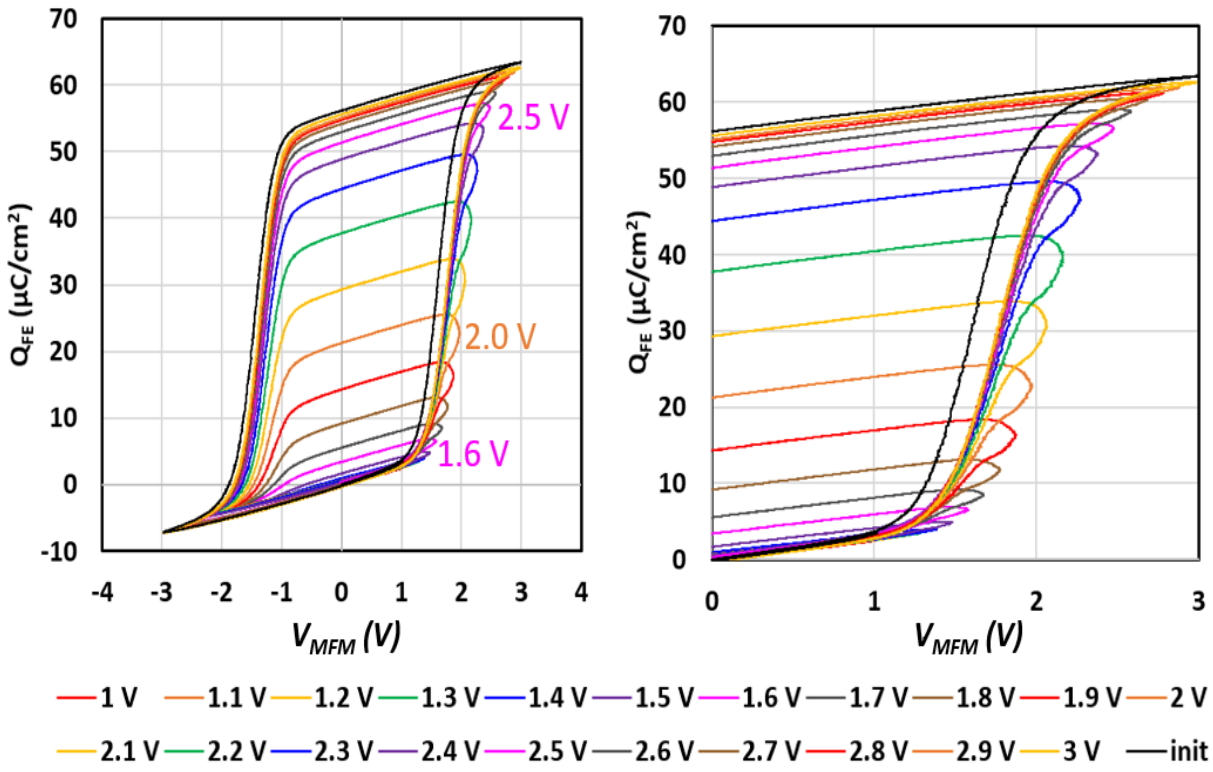

Fig. 4-14. Voltage dependence of recovery behavior of 370-μm^2 area FE-HZO MFM capacitor (left) and the magnified data of positive voltage region (right).

4.3.3 Cycling Frequency Dependence

As described in Section 4.2.6, the imprint effect becomes more prominent as the cycling time (Pcyc) increases. In this section, we examine the impact of cycling frequency on the recovery behavior. After a Pcyc-1000 s imprint delay (V_P=0V) is applied, a sequence of 3000 Pread with 3 V amplitude was employed for the recovery cycling. To assess the frequency dependence, different frequencies of recovery cycling were applied, 1 kHz, 10 kHz, 100 kHz, and 1 MHz.

Figure 4-15 illustrates that lower frequency cycling can effectively restore imprinted domains with a smaller number of cycles. Additionally, the number of cycles required for each recovery increases by approximately one order of magnitude with each corresponding increase in cycle

frequency. In other words, the total time duration of the recovery process (period × number of cycles = 0.01 s) remains almost constant. This observation indicates that there exists a required total recovery time for imprint recovery using electric field cycling that depends on the extent of imprint.

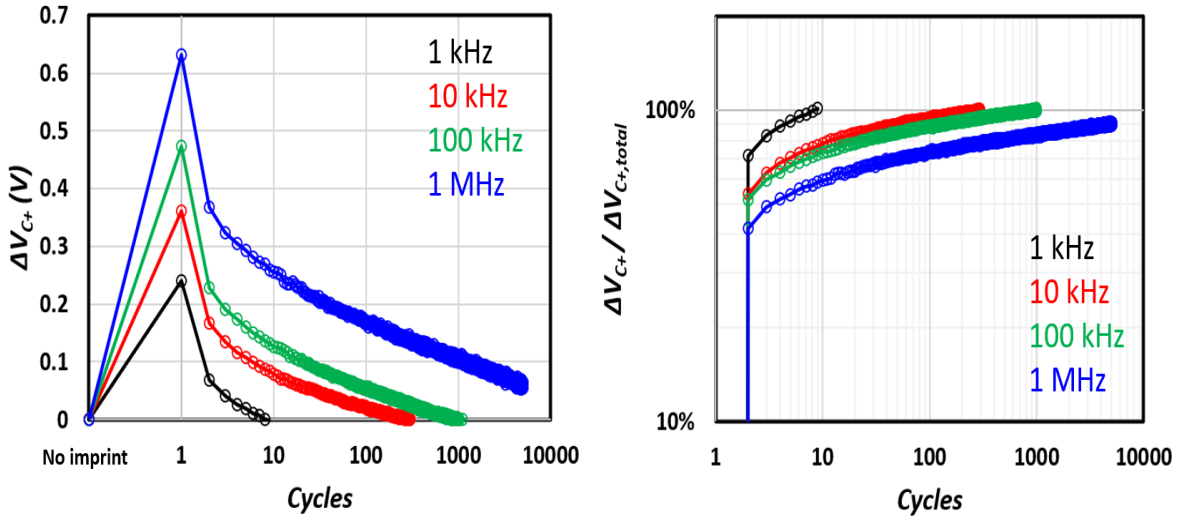

Fig. 4-15. Recovery behavior of 370-μm^2 area FE-HZO MFM capacitor using triangular waveforms at various frequency after 1000 s delay. ΔV_{C+} vs. cycles (left) and recovery rate vs. cycles (right). When ΔV_{C+} = 0 V (left) and recovery rate = 100 % (right), 1000 s imprint is recovered.

This result suggests an interesting procedure. If a single slow quasi-static Q-V loop is taken that gives ample time for all domains to track the voltage waveform, an imprint free situation can be created at any P-V state regardless of the previous history. For example, C-V measurements with slow DC ramp rate can be done under imprint free condition as long as a device is appropriately initialized. This conclusion is also consistent with the result in Section 4.2.5.

4.4 Evaluation of Imprint Models

This section discusses the two mainstream models proposed in the literature in light of our observations. While the conclusions here suggest *what is unlikely to be happening*, there needs to be more work before a conclusive suggestion about what is *likely to be happening* can be reached.

4.4.1 Mobile Defect Migration Hypothesis

Various defects are generated inside HZO layer as part of the fabrication process and also during electric field cycling. Among them, singly and doubly positive charged oxygen vacancy (V_O^+ and V_O^{++}) are regarded as an ingredient of the imprint effect. It has been proposed that the diffusion of V_O^+ and V_O^{++} due to the depolarization field is the main cause for both imprint and wake-up [50]. In this section, we show that this hypothesis is inconsistent with our observations.

This mobile Vo migration hypothesis is evaluated by the experiments depicted in Fig. 4-16. Case 'A' represents a case of no imprint. Case 'B' and 'C' include an imprint phase with and without external electric field applied. While $V_P = 0$ V for 1 ms is applied after Pcyc in Case 'B', Case 'C' has a $V_P = -3.0$ V for 1 ms of imprint period at the last half pulse of Pcyc. According to the literature [50], if there are mobile Vo^+ and Vo^{++}, the defects should move due to a depolarization E-field toward the interface around the bottom electrode during the imprint period of Case 'B', as shown in the schematic. Then, the accumulated positive charges contribute towards an electric field across the FE-HZO layer. Therefore, we would observe a positive ΔV_C shift in the hysteresis loop since the applied electric field would have to be increased in order to compensate for the charge-defect-generated field. On the other hand, with an externally applied electric field during imprint as in

case ‘C’, the defects should migrate to the interface around the top electrode. This would then lead to a negative ΔV_C shift of the charge-voltage loop.

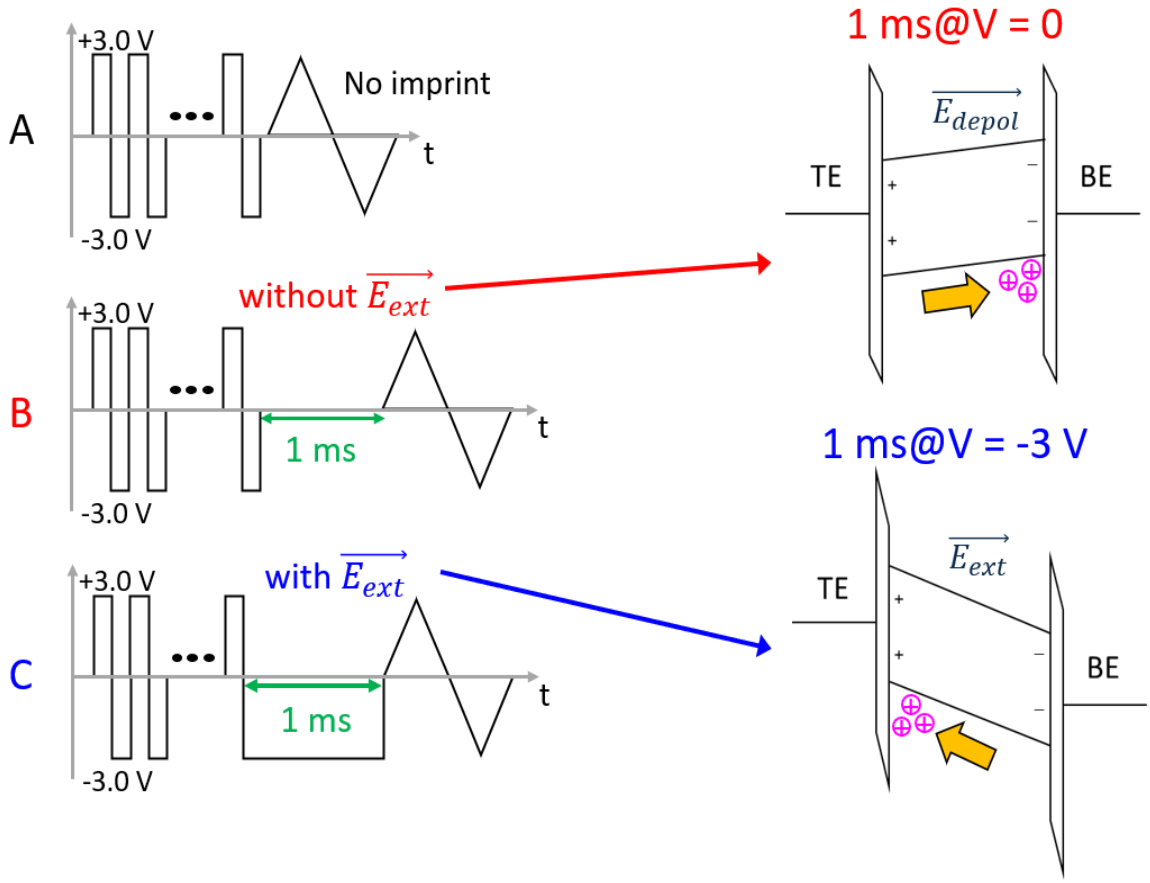

Fig. 4-16. Pulse measurement schemes for evaluation of mobile defect migration hypothesis (left). Energy band diagram at each imprint period and energy band diagrams depicting migration of positively charged defect inside FE-HZO (right).

However, as Fig. 4-17 shows, only a positive ΔV_C shift is observed in both cases ‘B’ and ‘C’ in contrast with the mobile positive charge hypothesis. Rather, the external electric field accelerates the imprint effect similar to the data in Section 4.2.5. Therefore, we conclude that the mobile charged defect migration is not consistent with our observations.

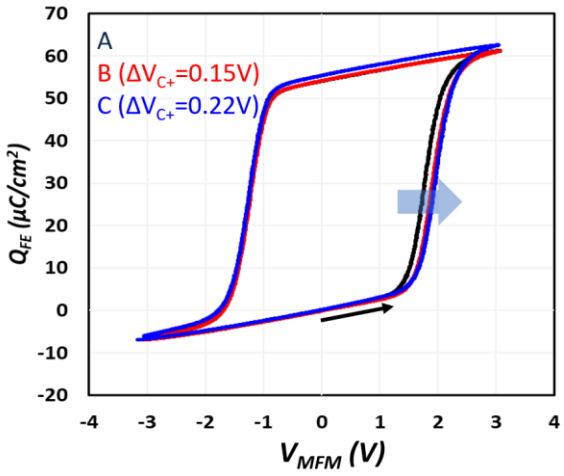

Fig. 4-17. Extracted Q_{FE} vs. V_{MFM} of 370-μm^2 area MFM capacitor from results of experiments shown in Fig. 4-16.

4.4.2 Interfacial Charge Trapping Hypothesis

Although the hypothesis of charge trapping induced imprint has been studied [33, 34, 35], there is no quantitative demonstration to verify that this hypothesis is applicable for FE-HZO films. This section investigates whether the interfacial charge trapping model is quantitatively consistent with our observations.

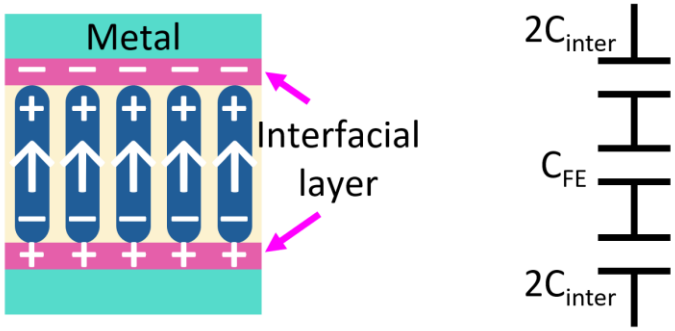

Fig. 4-18. Schematic of non-FE interfacial layers in an MFM structure with negative voltage applied to the top electrode (left), and the equivalent circuit model consisting of three series capacitors (right).

Let's assume that there exists a non-FE interfacial layer between the metal and the nominally ferroelectric, FE-HZO, layer. Then the MFM capacitor can be described by three capacitors

connected in series, as shown in Fig. 4-18. The existence of possible interfacial capacitances is supported by measurements of small-signal capacitance in FE MFM capacitors [49]. While for the PZT devices cited by Black et al. in [49], C_{inter} is between 7 and 25 μF/cm^2, in our own HZO experiments we have found consistent values of 18 μF/cm^2. This is well within the above range. Black et al. have attributed this capacitance to finite screening length in the metal itself, while others [33, 51] have attributed it to the presence of so-called dead-layers where charge could be trapped and manifest in imprint shifts of V_C. If we assume that the presence of C_{inter} is due to the latter, then indeed charge could be accumulated there due to the high field during imprint. Fig. 4-19 right shows a maximum value of ΔV_{C+} = 1.1 V (imprinted V_{C+} = 2.8 V with unimprinted V_{C+} = 1.7 V) during recovery. In order to generate a field in the FE HZO suitable for such shift in V_C, and assuming C_{inter} = 18 μF/cm^2, we calculate that trapped charge would amount to ≥ 19.8 μC/cm^2. This amount of charge while impossible to detect during the slow onset of imprint would be clearly visible during the rapid imprint recovery. But no such charge is observed in our experiments.

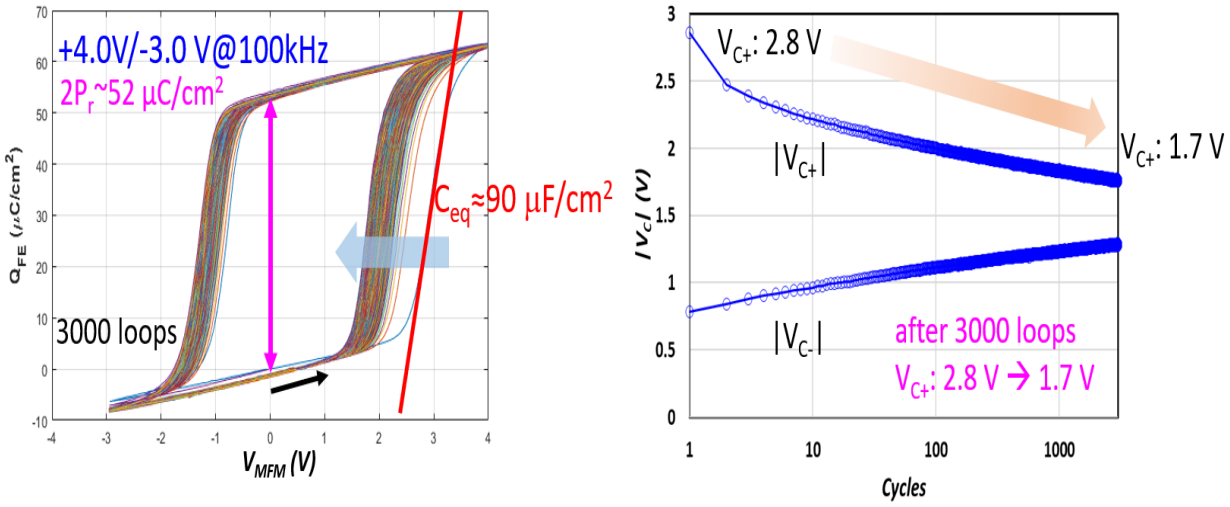

Fig. 4-19. Recovery of 360-μm^2 area 10 nm FE-HZO MFM structure. After imprint for 2 hours at 150 °C, 3000 triangular waveforms are applied to monitor the recovery behavior. Q_{FE} vs. V_{MFM} 3000 loops (left) and coercive voltage change vs. number of cycles (right).

Another way to approach the question of magnitude of the interfacial capacitances is from the highest slope, dQ/dV, of the hysteresis loop. Of course, this can also be accomplished by recording the maximum current, e.g., in Fig. 4-2. From Fig. 4-19, we see the maximum dQ/dV of the imprinted Q_{FE} vs. V_{MFM} loop as 90 μF/cm^2. This is the lower bound of the combined interfacial layer capacitance (C_{inter}), provided we assume that the dP/dV of the FE material is infinite. For more realistic dP/dV values the value of C_{inter} would be even higher. With this C_{inter} value, we can also calculate the density of the putative trapped charges necessary to produce a certain amount of coercive voltage shift, as we did above using the lower capacitance extracted from small-signal C-V measurements. Fig. 4-19 right shows a maximum value of ΔV_{C+} = 1.1 V (imprinted V_{C+} = 2.8 V with unimprinted V_{C+} = 1.7 V) during recovery. Therefore, the required minimum density of trapped charges (Q_{imp}) can be calculated by multiplying the minimum C_{inter} (90 μF/cm^2) and ΔV_{C+} (1.1 V) yielding Q_{imp} = 100 μC/cm^2. This value is almost double the $2P_r$, i.e., the total polarization density, and it is required to explain the imprint behavior using the interfacial charge trapping hypothesis. This is physically impossible. Besides, since such a charge would have to be exchanged with the external source, as discussed above, it would result in significant current of a magnitude comparable to that due to polarization switching and produce significant Q-V loop distortion. Clearly, no significant de-trapping behavior is observed during the recovery process in Fig. 4-19, nor has it been observed in any of the experiments carried out during this research work. Therefore, it appears that charge trapping into dead layers at the interface of FE and metal is an unlikely candidate to explain the bulk of the imprint effect. Before leaving the subject, we should mention here that the reason for the significantly higher C_{inter} capacitance extracted from large-signal capacitance measurement is currently unclear and subject to further investigation.

4.5 Summary

This chapter has presented comprehensive imprint behavior in various voltage pulse experiments using accurately calibrated measurement setup. The observed imprint effect is consistent with the literature showing a linear increase of ΔV_C with log t_d. However, no P_r dependence of ΔV_C is observed in our samples, which is inconsistent with some of the previously proposed models that suggest P_r-dependent depolarization field as a root cause of the imprint effect.

New findings of the imprint effect also have been demonstrated in this study. As Pread frequency increases, ΔV_C also increases, which means that a longer read voltage pulse reduces the imprint effect. Furthermore, this result implies that electron trapping and de-trapping at the non-FE interfacial layer may not play a significant role in the imprint behavior because no electron de-trapping and no capacitance change in the Q-V loops were observed in experiments at different Pread frequencies even though they showed different degrees of imprint. It was also demonstrated that the imprint effect can be accelerated by the application of a non-switching voltage pulse during the imprint phase and as well as Pcyc of a total time duration.

In addition, the recovery behavior of imprinted FE-HZO has been characterized in detail by capturing over a thousand responses of electric field cycling. A significant recovery in the first few cycles was observed followed by a similar recovery rate regardless of the voltage amplitude of the electric field cycling provided they are high enough to switch all FE domains. This observation means that the recovery rate is not accelerated by the voltage amplitude of the recovery cycle unlike the voltage dependence of the imprint effect.

By applying recovery cycles with various voltage amplitudes that yield partial polarization switching, independent domain recovery behavior with the same recovery rate has been observed. This is because only domains with smaller E_a than the electric field resulting from the applied voltage can recover according to the Nucleation Limited Switching (NLS) model. Also, by comparing recovery characteristics with different cycling frequencies, it was found that there is a required total duration for the recovery phase for imprint to fully recover.

Lastly, an evaluation of proposed existing imprint models founded on mobile defect migration hypothesis and interfacial charge trapping hypothesis was presented. Our measurement and quantitative analysis have concluded that none of these theories is consistent with the observed imprint behavior.

Chapter 5 Analysis and Modeling of Small-Signal Characteristics of FE-HZO Structures

5.1 Introduction

This chapter presents results from small-signal measurements of MFM coplanar waveguide structures over a broad range of frequencies using the experimental setup described in Section 2.3. Based on the observed impedance characteristics after the de-embedding process, we propose a small-signal equivalent circuit model that reproduces the experiments across the entire frequency range. Additionally, we provide a detailed physics-based explanation for characteristics of each circuit element in the proposed model. Lastly, we address the physical origin of a butterfly shaped C-V curve.

5.2 Impedance Characteristics after De-embedding Process

In Fig. 5-1, the de-embedded impedance (Z) data of the 24-μm^2 area MFM capacitor described in Section 2.1.2 is presented after all parasitics are carefully de-embedded as discussed in Section 2.3.2. The figure shows the extracted real part (Re(Z)) and imaginary part (|Im(Z)|) of the impedance data obtained using the three different instruments. Four DC bias points are chosen to observe how impedance characteristics change with respect to FE states. The DC bias points of -3.0 V and +3.0 V correspond to the positions of minimum capacitance in the butterfly shaped C-V curve. On the other hand, the bias points of +1.2 V and -0.8 V represent the positions of peak capacitance in the C-V curve. Even though we conducted measurements up to 50 GHz, the data is presented only up to 20 GHz because noise appears beyond 20 GHz due to limits of the VNA

equipment. The impact of the imprint effect is negligible in this case because the DC sweep frequency used, which is 50 mHz, is sufficiently slow to ignore any imprint effects, as shown in Section 4.2.3.

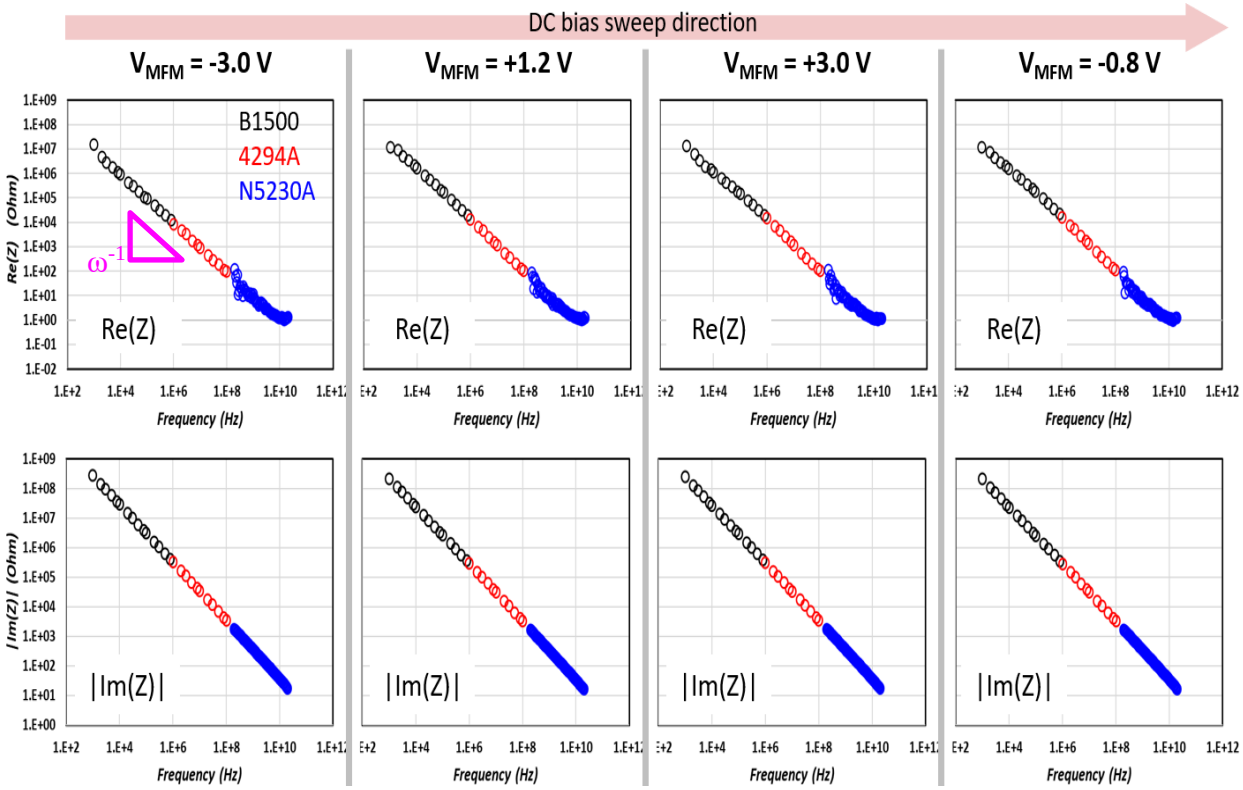

Fig. 5-1. De-embedded Re(Z) (top) and |Im(Z)| (bottom) vs. frequency data from measured Z using three instruments. Columns represent different DC bias points swept from left to right. Colors correspond to the used instruments. Magenta triangle represents a slope of ω^{-1}.

As shown in the figure, the accurate measurement stitches the data points meticulously at the frequency range boundaries of each instrument. Both frequency dependence of the Re(Z) and Im(Z) appears with a slope close to -1. This frequency dependence is maintained regardless of DC bias points.

5.3 Small-Signal Equivalent Circuit Model

Based on the measured impedance characteristics presented in the previous section, this section proposes a new equivalent circuit model. Starting with a basic parallel RC circuit model, circuit elements are mathematically modeled to describe the frequency characteristics of the measurement data. Then, we demonstrate how the model performs well with the measurements.

5.3.1 Basic RC Parallel Circuit Model

Fig. 5-2 shows a parallel RC circuit with an access resistance in series that is widely used for small-signal analysis of capacitors. In this model, all elements are frequency- and voltage-independent.

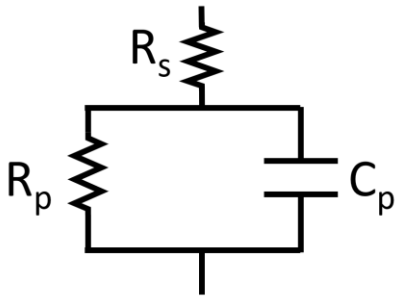

Fig. 5-2. Basic RC parallel small-signal equivalent circuit model for a capacitor. All elements are voltage- and frequency-independent.

The impedance of the circuit of Fig. 5-2 can be described in the frequency domain as follows:

$$Z(\omega) = R_S + \frac{R_P}{1 + \omega^2 C_P^2 R_P^2} - j\frac{\omega C_P R_P^2}{1 + \omega^2 C_P^2 R_P^2} \tag{5-1}$$

where ω is the angular frequency. We can apply an approximation of $1 \ll \omega^2 C_P^2 R_P^2$ to the denominators in equation (5-1) since the minimum measured value of $\omega^2 C_P^2 R_P^2$ is 352 across the entire frequency and voltage range. Then, equation (5-1) can then be simplified to:

$$Z(\omega) \cong R_S + \frac{1}{\omega^2 C_P^2 R_P} - j\frac{1}{\omega C_P} \tag{5-2}$$

As shown in equation (5-2), according to the basic RC parallel model, the real part is expected to exhibit a slope of ω^{-2} in relation to frequency, while the imaginary part should have a slope of ω^{-1}. However, the measurements of Fig. 5-1 show a frequency-dependent slope close to ω^{-1} in both Re(Z) and Im(Z). Therefore, the Im(Z) is consistent with the model whereas the Re(Z) is not. In the following section, we mathematically model this inconsistent frequency dependence of Re(Z).

5.3.2 Frequency-dependent R_p

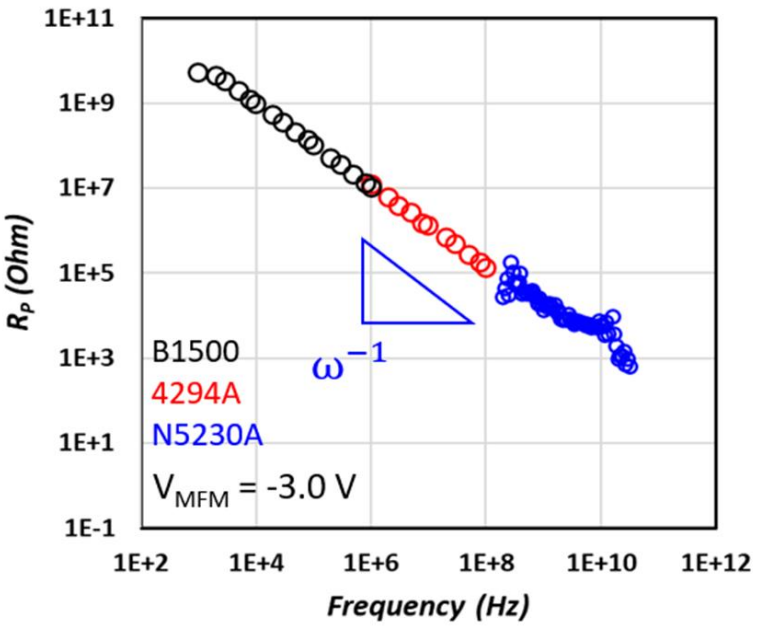

Fig. 5-3. Example of extracted R_p using equations (5-3) and (5-4) when V_{MFM} = -3.0 V. R_p has frequency dependence with a slope close to -1.

The frequency dependence of the Re(Z) can be explained by a frequency-dependent ac resistance R_p. From the measurement data, R_p is calculated by rearranging equation (5-2):

$$R_P = \frac{1}{\omega^2 C_P^2 (Re(Z) - R_S)} \tag{5-3}$$

where,

$$C_P = \frac{1}{\omega |Im(Z)|} \tag{5-4}$$

R_s of 0.5 Ω is extracted from the saturated Re(Z) beyond 10 GHz that can be observed in Fig. 5-1. Fig. 5-3 shows an example of R_p vs. frequency when V_{MFM} = -3.0 V obtained using this procedure. R_p exhibits a frequency dependence with a slope close to -1. This is also the case at all other DC bias points investigated. Therefore, we fit the extracted R_p data with a function of ω^{-s}.

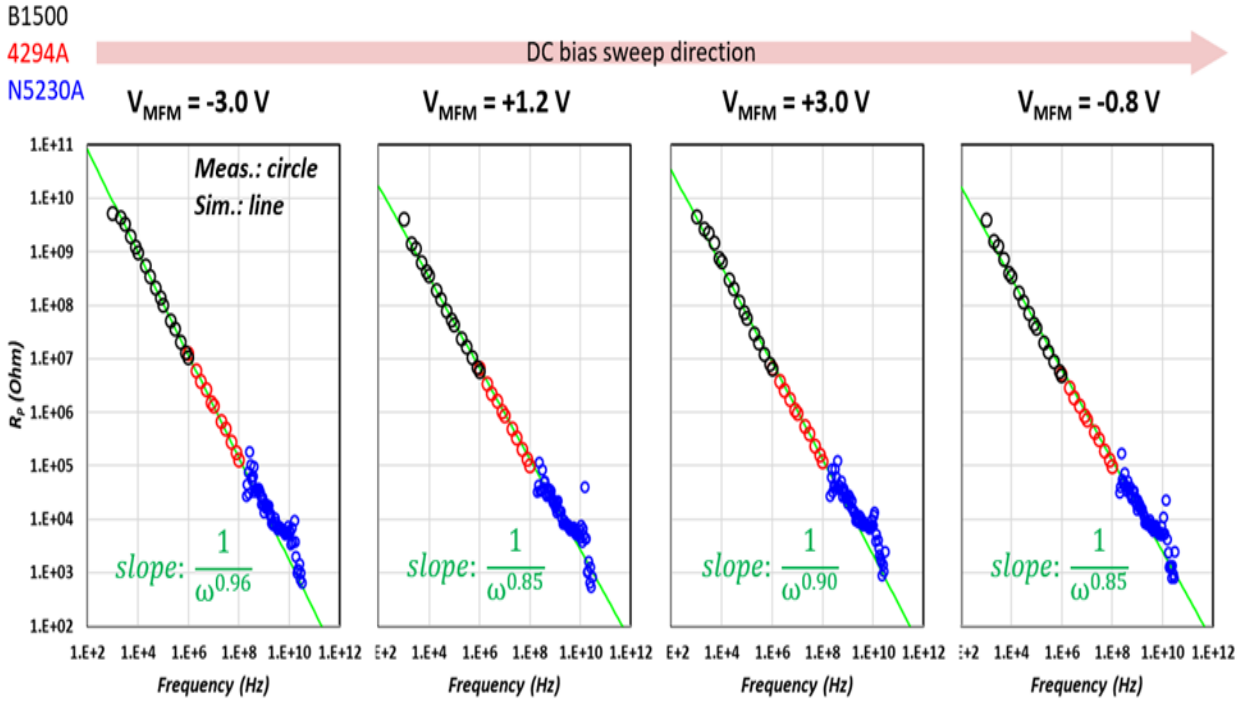

Fig. 5-4. Comparison of R_p at four DC bias points between measurement (dot) vs. model (line) as a function of frequency. Slopes are indicated in graphs for each bias point.

Fig. 5-4 shows a comparison of R_p between measurements and a model that follows a function of ω^{-s} at four bias points. The model shows an excellent match with the measurements. The fitted exponent 's' value is slightly less than 1 and depends on the DC bias point. The physics origin of the frequency dependence of R_p will be discussed in Section 5.4.1.

5.3.3 Frequency-dependent C_p

C_p of the equivalent circuit model in Fig 5-2 can be extracted from Im(Z) using equation (5-4). While it may seem that C_p remains constant because the frequency dependence in the |Im(Z)| vs. frequency graph of Fig 5-1 seems to have a slope of ω^{-1}, a small frequency dependence becomes evident after calculation using equation (5-4). This is typically observed in C-V curves measured at different frequencies (e.g., Fig. 2-6) [44, 52].

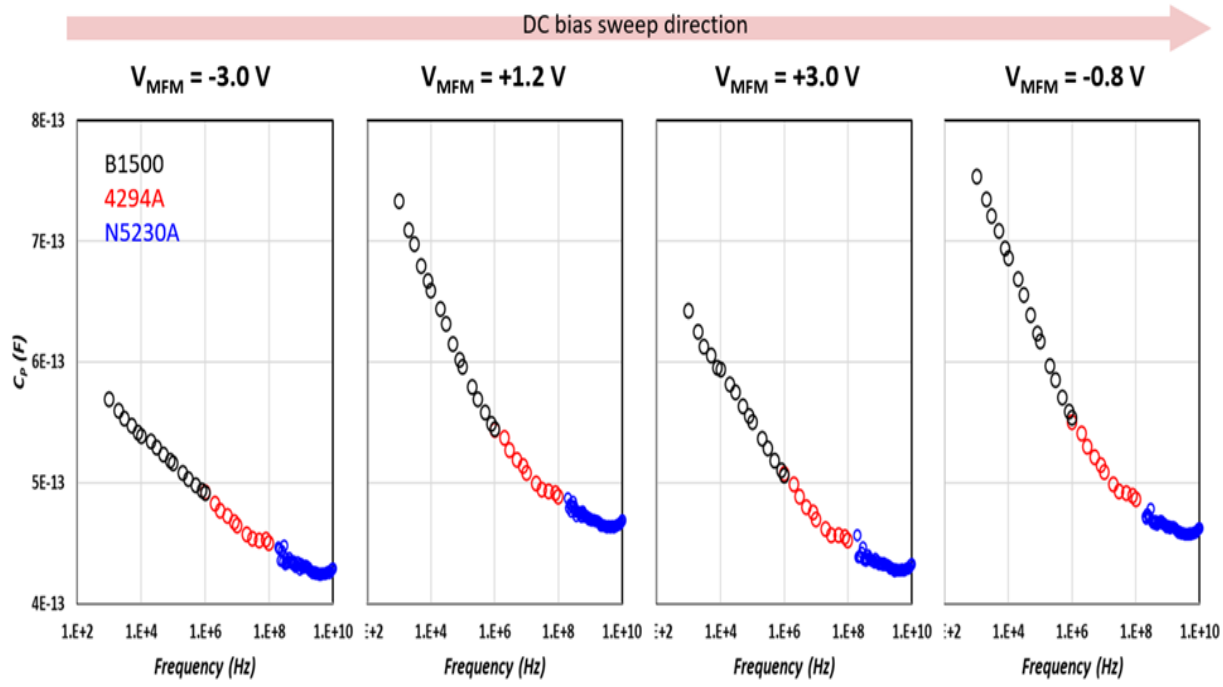

Fig. 5-5. Extracted C_p vs. frequency at different DC bias points.

Fig. 5-5 shows frequency-dependent C_p at different DC bias points. C_p logarithmically decreases with frequency and the frequency dependence disappears above 1 GHz. As described in Fig. 5-6, we mathematically model the C_p behavior by dividing it into two parallel capacitances, a frequency-independent intrinsic capacitance (C_{int}) and a frequency-dependent extrinsic capacitance (C_{ext}). The physical origin of C_{int} and C_{ext} will be discussed in Section 5.4.

The capacitance of a MFM structure is then described as follows:

$$C_p(f) = C_{int} + C_{ext}(f) = C_{int} + C_0 log(1 + \frac{f_0}{f}) \quad (5\text{-}5)$$

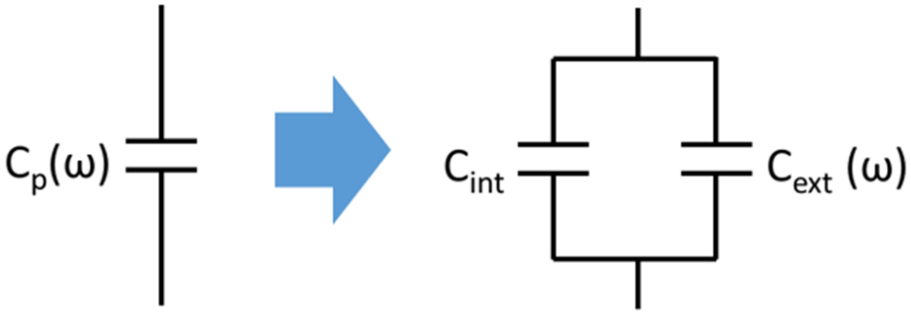

Fig. 5-6. Suggested equivalent circuit model of C_p consisting of two capacitors, C_{int} and C_{ext}. Only C_{ext} depends on frequency.

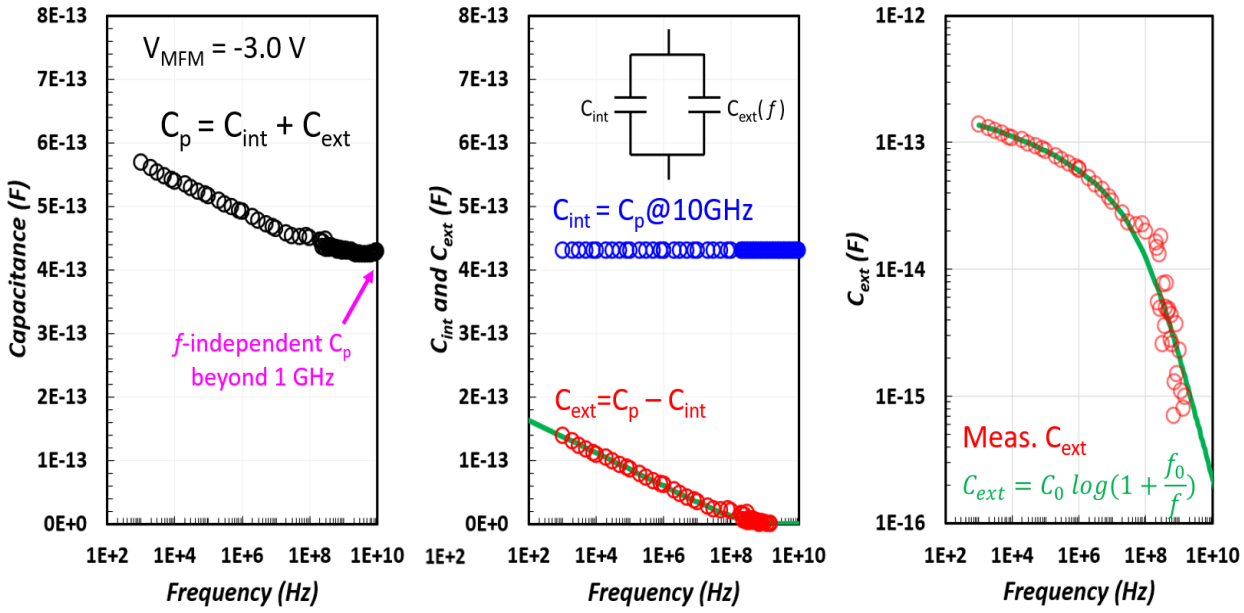

Fig. 5-7. Example of interpretation of frequency-dependent $C_p(\omega)$ at V_{MFM} = -3.0 V. Total C_p (left) is divided into C_{int} (blue in center) and C_{ext} (red in center). Comparison of C_{ext} (right) between measurement (dot) and model when C_0 = 26 fF and f_0 = 200 MHz (line).

Fig. 5-7 demonstrates the interpretation of the frequency-dependent C_p. This interpretation emerges from the observation that the overall capacitance decreases logarithmically with frequency up to 1 GHz and becomes constant beyond that frequency. Accordingly, the frequency independent C_{int} must correspond to the C_p value at 10 GHz where there is no dependency on frequency. On the other hand, $C_{ext}(f)$ is calculated by subtracting C_{int} from $C_p(f)$. C_{ext} is fitted using a decay function that incorporates a logarithmic term as shown in equation (5-5). Fig. 5-7 displays the expression for C_{ext} which captures well the measurement data.

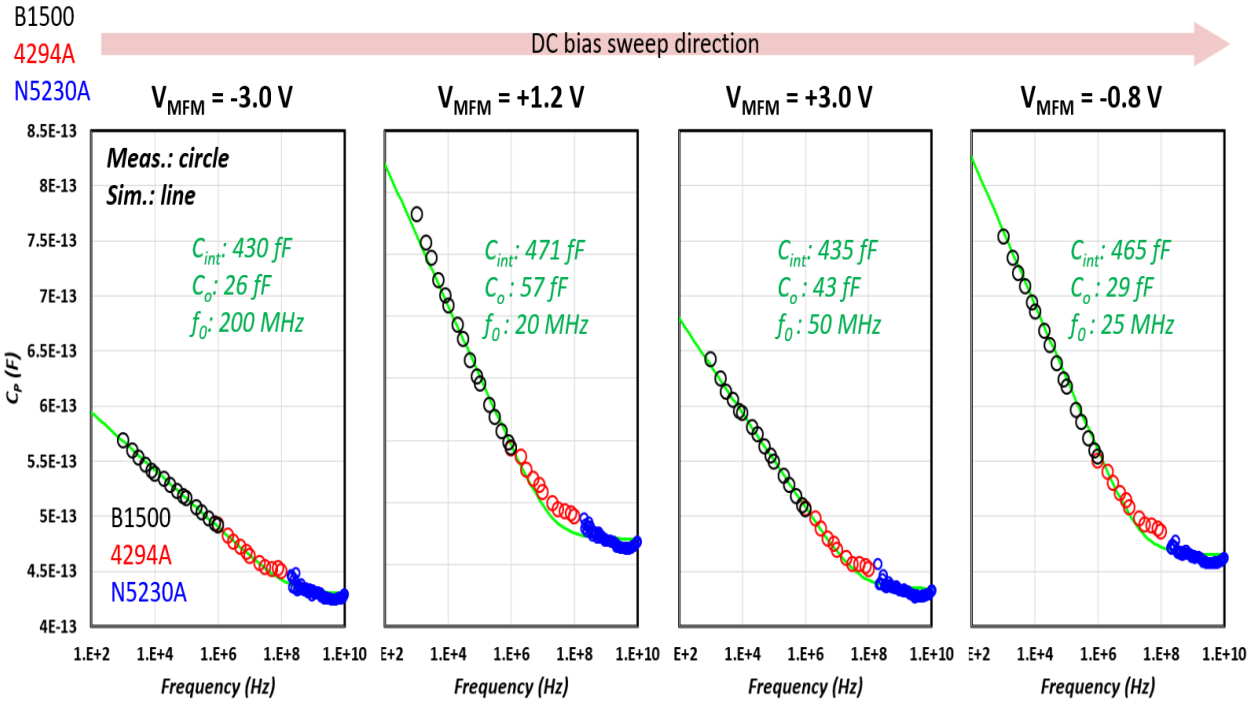

Fig. 5-8. Comparison of C_p at four DC bias points between measurement (dot) and model (line). Parameters are indicated in graphs for each bias point. The units of C and C in the labels are F.

The measured C_p data at different bias points is fitted using equation (5-5), as shown in Fig. 5-8. The parameters, C_{int}, C_o, and f_o, depend on DC bias points. The model shows reasonable match with the measurement.

5.3.4 Equivalent Circuit Model of FE-HZO MFM Capacitor

At this point the MFM capacitor can be represented by the small-signal equivalent circuit shown in Fig. 5-9. As shown in Fig. 5-9, the model is composed of a series resistance (R_s), and a parallel connection of two capacitors (C_{int} and C_{ext}) and one resistor (R_p). R_s represents the voltage- and frequency-independent W-electrode resistance with a value of 0.5 Ω. R_p corresponds to the ac resistance of the FE-HZO that exhibits a reciprocal function of frequency, ω^{-s} (with close to 1), as described in Section 5.3.2. In terms of capacitance, the model includes frequency-independent C_{int} and frequency-dependent C_{ext}, which is also described in Section 5.3.3.

It is worth noting that this model does not incorporate a so-called "constant-phase element". A constant-phase element is a mathematically expedient element typically employed in equivalent circuit models of MFM structures to fit measured data, even if the underlying physics is not well-established [38, 39]. The physics of the elements in our model will be discussed in Section 5.4.

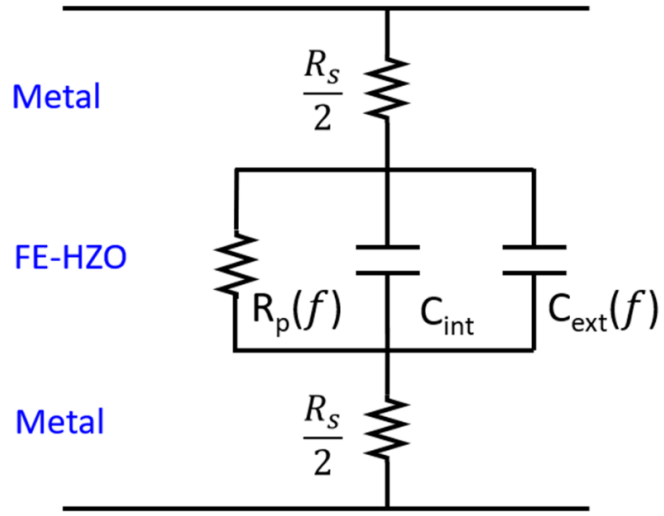

Fig. 5-9. Equivalent circuit model of FE-HZO MFM capacitor.

5.3.5 Circuit Simulation vs. Measurements

We compare the simulated data from the equivalent circuit model to the measurement data. One set of model parameters is applied to the circuit model for each individual DC bias point. To compare with the data shown in Fig. 5-1, the parameters in Table 5-1 are used for the model depending on DC bias points. Fig. 5-10 demonstrates a comparison of impedance characteristics between measurements and simulations. The equivalent circuit model exhibits a close match with the measurements across the entire frequency range at all bias points.

DC bias	R_s	R_p	C_{int}	C_{ext}
-3.0 V	0.5 Ω	$\frac{3.9 \times 10^{13}}{\omega^{0.96}}$ Ω	430 fF	$2.60 \times 10^{-14}\ log\ (1 + \frac{2\times10^{8}}{f})$ F
1.2 V	0.5 Ω	$\frac{4.0 \times 10^{12}}{\omega^{0.85}}$ Ω	471 fF	$5.70 \times 10^{-14}\ log\ (1 + \frac{2\times10^{7}}{f})$ F
3.0 V	0.5 Ω	$\frac{1.1 \times 10^{13}}{\omega^{0.90}}$ Ω	435 fF	$4.30 \times 10^{-14}\ log\ (1 + \frac{5\times10^{7}}{f})$ F
-0.8 V	0.5 Ω	$\frac{3.8 \times 10^{12}}{\omega^{0.85}}$ Ω	465 fF	$2.90 \times 10^{-14}\ log\ (1 + \frac{2.5\times10^{7}}{f})$ F

Table 5-1. Model parameters for four DC bias points.

Furthermore, Fig. 5-11 presents a detailed comparison of the data and model at V_{MFM} = -3.0 V to confirm the match. The comparison is plotted on a semi-log scale as the log-log scale of Fig. 5-10 might exaggerate the model accuracy. The model still shows an outstanding match with the data across the entire frequency range.

In this section, we have introduced a small-signal equivalent circuit model of the MFM capacitor and confirmed its accuracy by comparing to measurements. However, all model elements have been mathematically fitted to the observed data rather than being based on a physics-driven explanation. In the following section, we will elucidate the origins of frequency-dependent R_p and C_p.

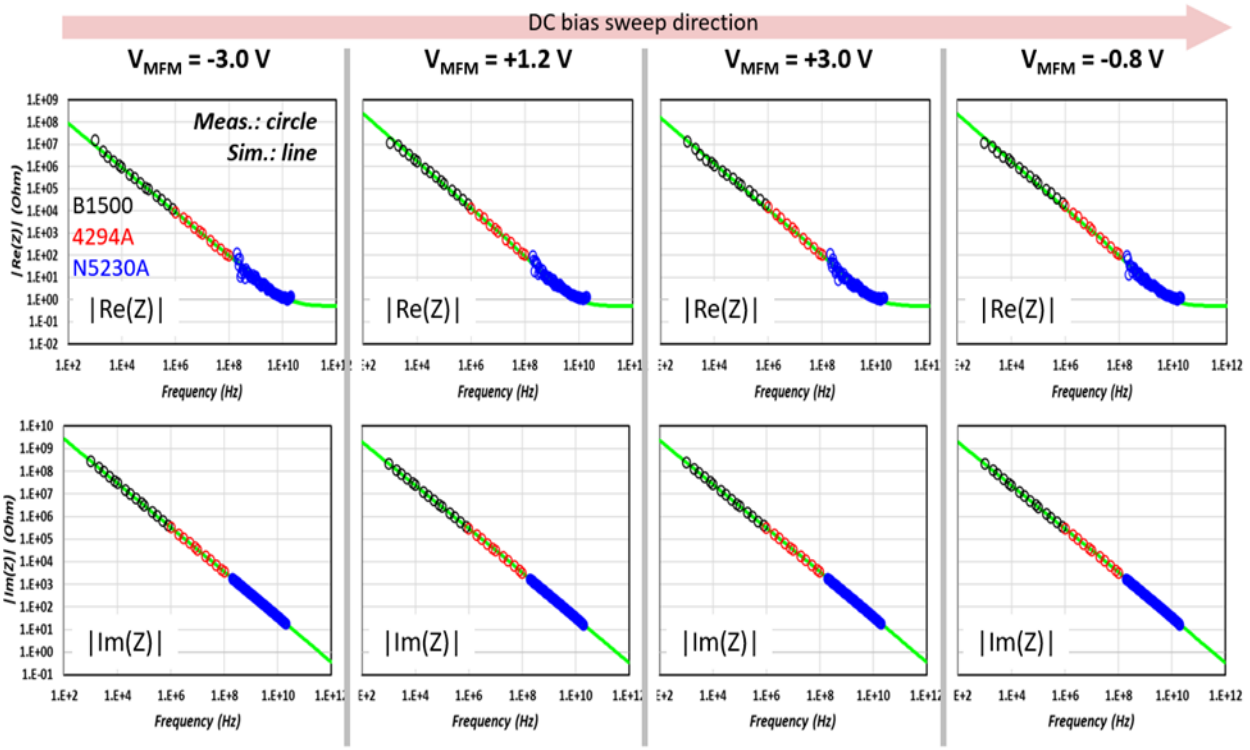

Fig. 5-10. Comparison of impedance characteristics between measurement and simulation. The data is presented in the same manner as Fig. 5-1, but the lines correspond to simulation data from the equivalent circuit model with parameters in Table 5-1.

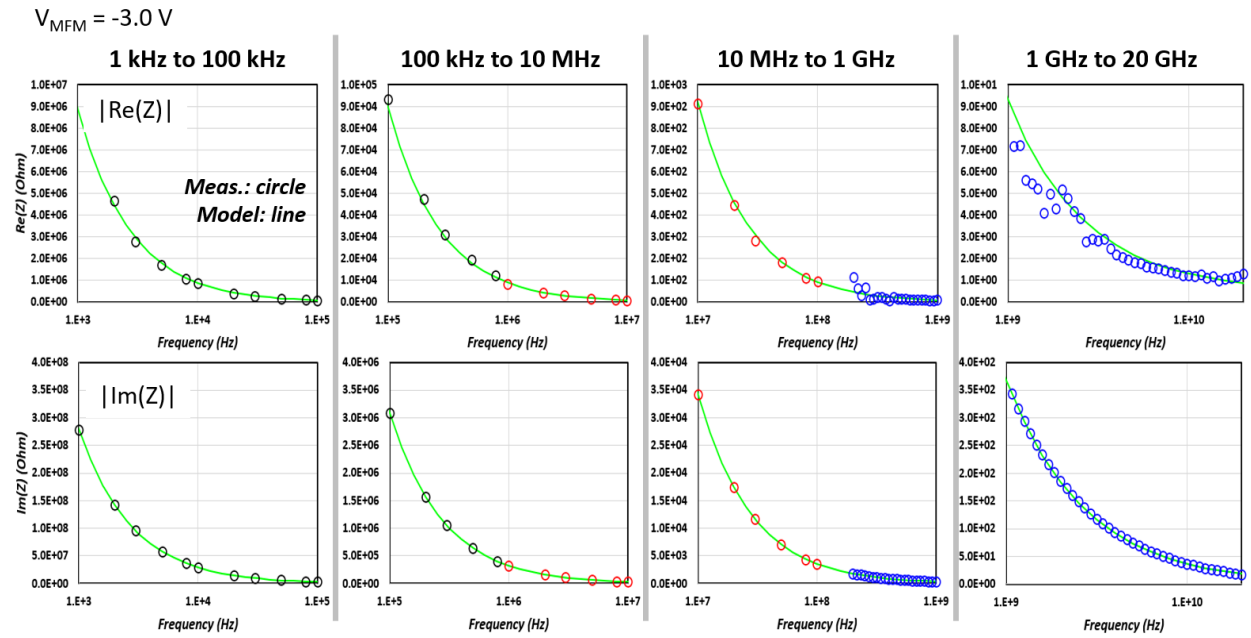

Fig. 5-11. Comparison of impedance characteristics in semi-log scale between measurement and simulation. Same data presented in Fig. 5-10 when V_{MFM} = -3.0 V. Columns represent two decades of frequency.

5.4 Physics of Model Elements

In the previous section, it has been found that a simple parallel RC circuit is inadequate to represent the measurement data accurately. As a result, frequency-dependent R_p and C_p elements have been introduced and a complete small signal model has been developed and compared against data. This section provides an explanation for the frequency dependence of R_p and C_p.

5.4.1 Physics Origin of R_p

We have experimentally observed a frequency dependence for R_p that is well fitted using a function of ω^{-s} with s close 1. This frequency dependence can be explained by the well establish theory of universal dielectric response of ac conductivity (σ_{ac}) [53].

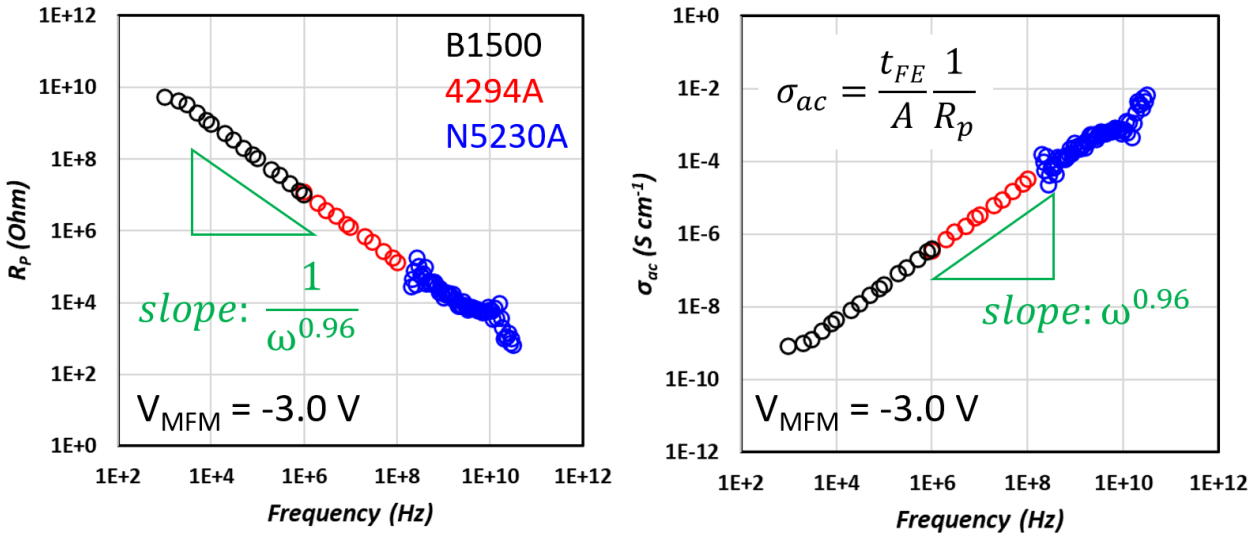

Fig. 5-12. Extracted R_p vs. frequency from Re(Z) at V_{MFM} = -3.0 V (left). Calculated σ_{ac} vs. frequency from left figure using equation indicated in legend (right)

σ_{ac} of our FE-HZO MFM was calculated from the observed R_p by:

$$\sigma_{ac} = \frac{t_{FE}}{A}\frac{1}{R_p} \tag{5-6}$$

where t_{FE} is FE thickness and A is the area of the capacitor.

Fig. 5-12 shows an example of conversion from R_p to σ_{ac} with the data measured at V_{MFM} = -3.0 V. The calculated σ_{ac} obviously has a frequency dependence with a slope of 0.96, which is the inverse slope of R_p. A frequency exponent 's' in ω^s close to 1 is observed across all DC bias points as shown in Table 5-1.

This behavior of σ_{ac} is not unique to FE-HZO and it is consistent with a universal dielectric response that has been observed in many different dielectric systems. In fact, we also have observed this frequency dependence in our MIM Al_2O_3 samples, although the data is not included here. As shown in Fig. 5-13, Jonscher revealed a remarkable universality of a power law dependence of σ_{ac} vs. frequency for a wide range of solid dielectrics with an exponent 's' less than 1 [53]. We have confirmed that our measurements fall well into a narrow range well within the realm of s-universality of [36], as indicated by the red box in Fig. 5-13. This gives us confidence on the extraction process and the interpretation of R_p.

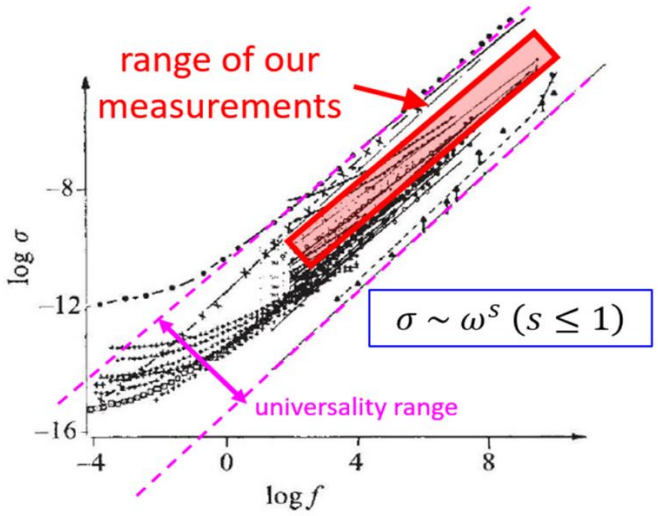

Fig. 5-13. Compilation of σ_{ac} vs. frequency for dielectric capacitors from Fig. 3 of ref. [53] showing the relatively narrow range of ac conductivity across a wide variety of dielectrics. The red box highlights the measured σ_{ac} range of our device across all DC bias points and frequencies.

To explain the dielectric response with a power exponent s ≤ 1, different ac conduction models have been proposed depending on the dielectric relaxation mechanism [54]. Each model has unique frequency and temperature dependence of the exponent 's'. Among the models, we have found that the *correlated barrier hopping (CBH) model* [55] is consistent with our small-signal measurements at different frequencies and temperatures.

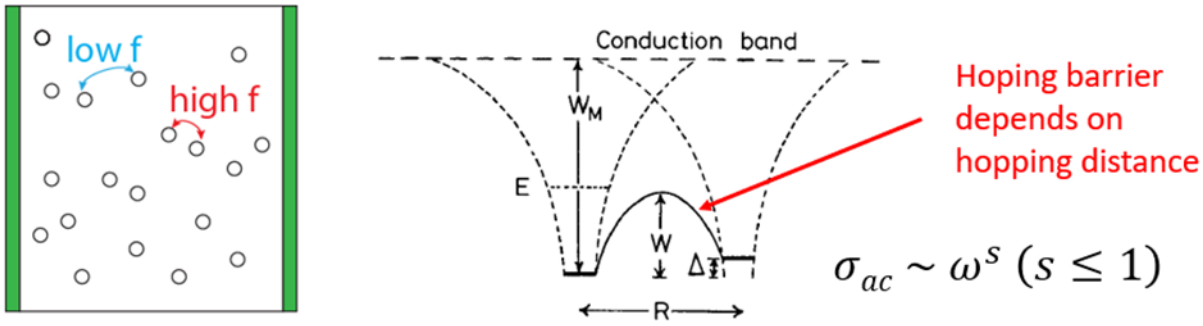

Fig. 5-14. Schematic of correlated barrier hopping (CBH) model, frequency dependence (left) and hopping mechanism (right) [55].

Fig. 5-14 represents the ac conduction mechanism of the CBH model. Basically, the model describes electron hopping by thermal activation over the barrier between two potential wells of two different trapping sites. For neighboring sites, the two wells overlap, resulting in lowering of the effective barrier from W_M to W, as depicted in Fig. 5-14. Accordingly, when an ac signal is introduced, electrons can hop back and forth between trapping sites within a distance (R). Also, the hopping barrier depends on R, i.e., the barrier becomes lower with a smaller R. This hopping motion over the barrier enables the electrons to participate in the conduction in response to ac signals.

According to the CBH model, the conduction has frequency and temperature dependence. As the frequency of ac field increases, R decreases as electrons have less time to move in response to the electric field. With a shorter hoping distance, the AC conductivity increases with a frequency dependence with a slope slightly less than 1 ($s \leq 1$). However, the frequency dependence becomes weaker as temperature increases due to higher thermal energy of electrons. The frequency dependence in the CBH model can be expressed in terms of the frequency exponent 's' as [54].

$$s = 1 - \frac{6k_B T}{W_M - k_B T \ln\left(\frac{1}{\omega\tau_0}\right)} \tag{5-7}$$

where k_B is the Boltzmann constant, T is the absolute temperature, and τ_0 is the characteristic relaxation time.

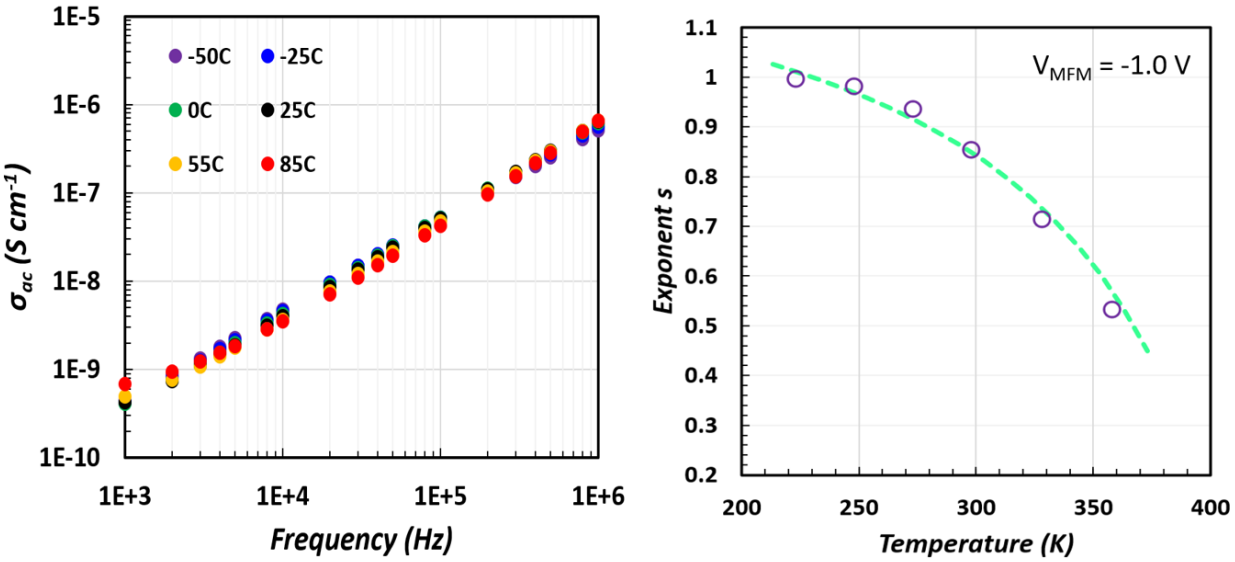

Fig. 5-15. Frequency dependence of σ_{ac} at different temperatures (left) and temperature dependence of exponent 's' (right) when V_{MFM} = -1.0 V. Exponent 's' is fitted by Eq. 5-7 with W_M = 0.95 eV, τ_0 = 1 fs (green).

Fig. 5-15 shows frequency dependence of σ_{ac} at different temperatures with a larger MFM sample (2500 μm^2). The data presented in Fig. 5-15 support the validity of the CBH model, as it

demonstrates the expected frequency dependence of the σ_{ac} with a slope close to 1 and reveals a decrease in the exponent 's' with increasing temperature that follows a law as in Eq. 5-7 (Fig. 5-15, right).

Although the data is not shown here, the increase of σ_{ac} is observed as the number of Pcyc (described in Section 4.2.1) increases, which suggests that the increase of the FE-HZO defect density due to Pcyc contributes to the enhancement of the CBH conduction.

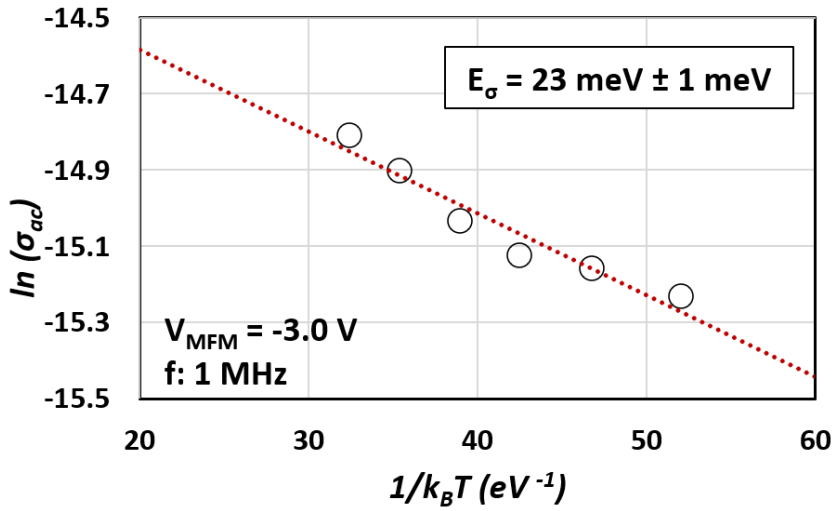

Fig. 5-16. Arrhenius plot of σ_{ac} vs. energy at 1 MHz for V_{MFM} = -3.0 V when σ_0 = 0.71 μS/cm.

To examine a core mechanism of the CBH model, the activation energy (E_σ) is extracted from the above experimental results. The temperature dependence of ac conductivity is fitted according to the Arrhenius equation [56]:

$$\sigma_{ac}(f) = \sigma_0(f)\, e^{\frac{-E_a}{k_B T}} \tag{5-8}$$

where σ_0 is the pre-exponential factor, k_B is Boltzmann constant, and T is absolute temperature. Fig. 5-16 displays the Arrhenius plot of σ_{ac} at V_{MFM} = -3.0V and E_σ of 23 meV is extracted from

the slope. The extracted E_σ is consistent with the electron hopping conduction via defect states in the HfO_2 system, which ranges from 22 to 35 meV [57, 58, 59]. This result also supports that the CBH model with an electron hopping basis is appropriate for FE-HZO dynamics rather than other conduction models based on quantum-mechanical tunneling, such as electron tunneling and polaron tunneling which would exhibit different temperature dependence [54].

The above E_a has been extracted from a σ_{ac} data set measured at 1 MHz. In Fig. 5-17, the activation energy values at two different DC bias points, V_{MFM} = -3.0 V and 1.2 V, are presented. These correspond to the minimum and maximum values of C_p. The graph shows that E_a depends on frequency and the bias point. Both frequency and bias dependence disappear at a frequency beyond about 400 kHz. This behavior might be related to the impact of dc conductivity which has a greater influence as the frequency decreases. Additionally, the opposite polarities of the E_a dependencies in the graph suggest that the observed dc conduction is closely associated with the direction of the FE polarization. These results deserve further study.

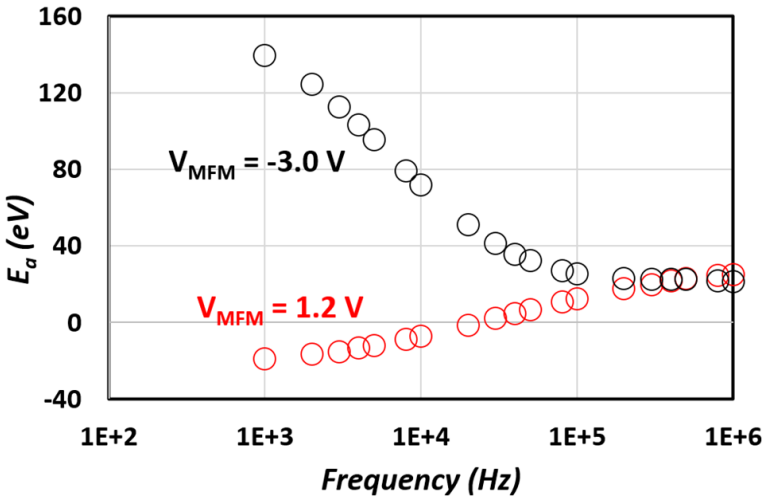

Fig. 5-17. Frequency and voltage dependence of extracted activation energy (E_a) of ac conductivity.

In this section, we have demonstrated that the frequency-dependent R_p in our equivalent circuit model is consistent with the CBH model.

5.4.2 Physics Origin of C_p

Towards understanding the physics behind the frequency dependence of C_p, we have investigated the C-V characteristics of the MFM capacitor over a broad frequency range, from 1 kHz to 10 GHz. The data are graphed in Fig. 5-18.

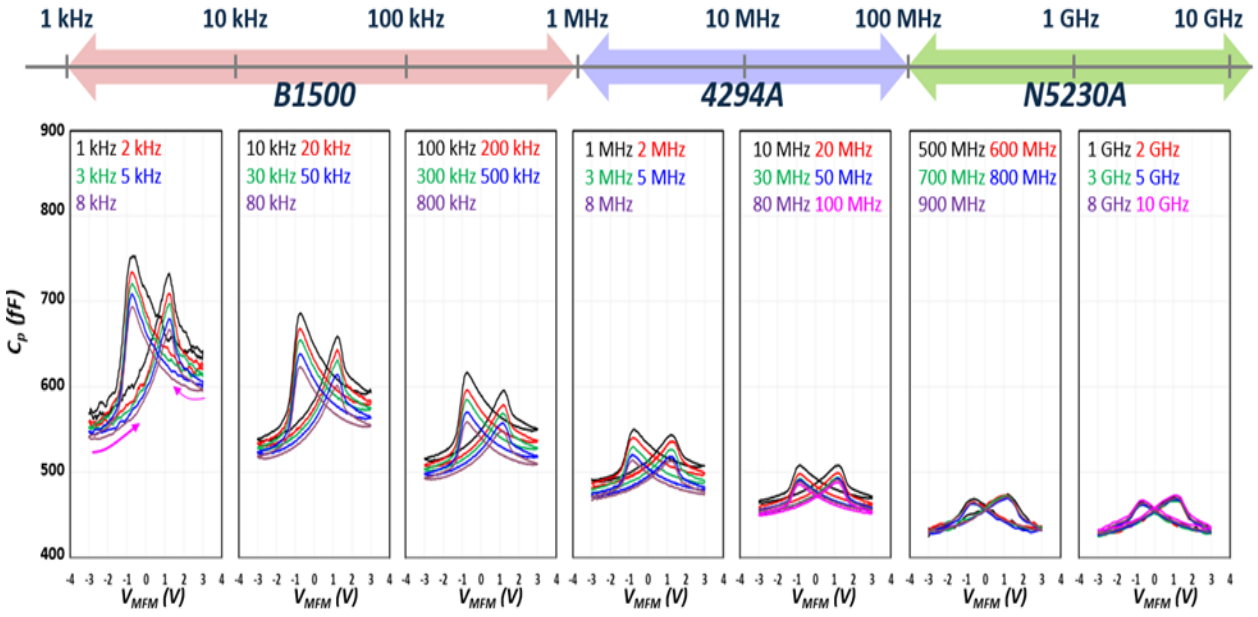

Fig. 5-18. C-V characteristics of the MFM structure in a coplanar waveguide configuration measured from 1 kHz to 10 GHz.

Fig. 5-18 clearly shows the same frequency behavior as the data in Section 5.3.3. C_p decreases logarithmically with frequency, and the frequency dependence disappears above 1 GHz. Further, the characteristic butterfly-shaped C-V curve remarkably persists into the GHz range with fixed peak capacitance positions in voltage, -0.8V and 1.2 V, across the entire frequency range. Also, the C-V curve becomes more symmetric and independent of frequency in the GHz range.

As presented in Section 5.3.3, we have modeled empirically the capacitive behavior of the MFM structure by two parallel-connected capacitors, a frequency-independent C_{int} and a frequency-dependent C_{ext}. Fig. 5-19 shows the C-V characteristics of C_{int} and C_{ext} at different frequencies extracted from C_p. As already discussed we assign the value of C_{int} as that of C_p corresponding to 10 GHz. This exhibits the characteristic butterfly shape. On the other hand, C_{ext}, obtained by subtracting C_{int} from C_p, demonstrates frequency dispersion while still maintaining a butterfly shape with C peaks occurring at fixed voltages independent of frequency.

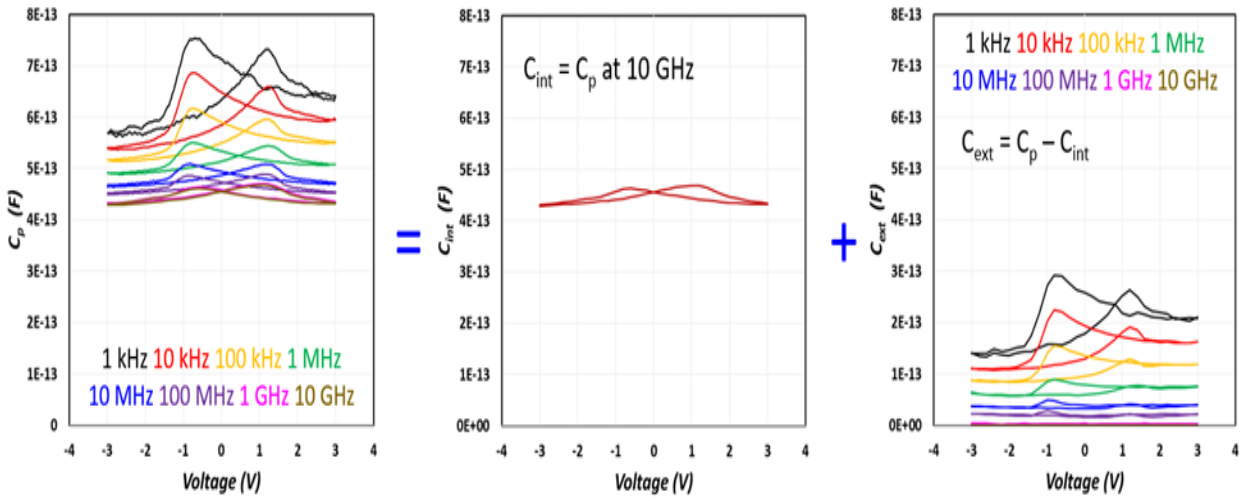

Fig. 5-19. Extraction of C_{int} (center) and C_{ext} (right) from C_p-V curves (left).

In this model, we postulate that the frequency-independent capacitance that dominates the high-frequency behavior likely represents the intrinsic nature of the FE-HZO. On the contrary, the frequency dependent behavior, C_{ext}, is of an extrinsic nature that originates in the response of defective structures. While this approach may initially appear to be solely based on mathematical fitting, the electron hopping model that was suggested to explain the frequency dispersion of ac conductivity can explain the frequency dependence of C_{ext} [60].

The frequency dependence of C_{ext} strongly resembles that of gate capacitance in HfO_2/metal-gate InGaAs MOSFETs [61]: it drops logarithmically with frequency, and it disappears around 1 GHz. In MOSFETs, this has been attributed to electron trapping in border traps in the dielectric that communicate with channel electrons through a tunneling process. As frequency gets higher, only traps that are closer to the interface are at play and C_g goes down. At high enough frequency, trapping becomes impossible. It is reasonable to expect this behavior in HZO (Fig. 5-20) prepared under similar conditions as in HfO_2/InGaAs MOSFETs. Also, this behavior is in line with the hopping mechanism.

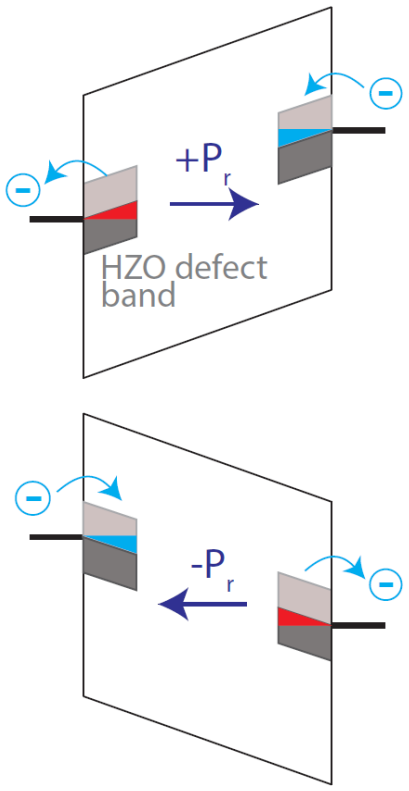

Fig. 5-20. Schematic of origin of frequency dependence of C_{ext} attributed to electron trapping in border traps in FE-HZO.

5.5 Origin of Butterfly Shape Capacitance-Voltage (C-V) Characteristics

In the previous section, we have presented the underlying physics behind the frequency-dependent R_p and C_{ext}. In this section, the voltage dependence of C_{int} is investigated so that we comprehend the origin of butterfly shape C-V characteristics.

5.5.1 Pure AC Capacitance at Different FE Polarization States

The presence of a butterfly shape in the C-V characteristics of a MFM capacitor is commonly attributed to FE domain wall (DW) vibrations [50, 62, 63]. To evaluate this hypothesis, we have carried out small-signal measurement at different FE states using a pulse generator. However, the DC bias is fixed at 0 V during the capacitance measurement to remove any DC-bias effects. This allows us to observe pure FE domain wall characteristics.

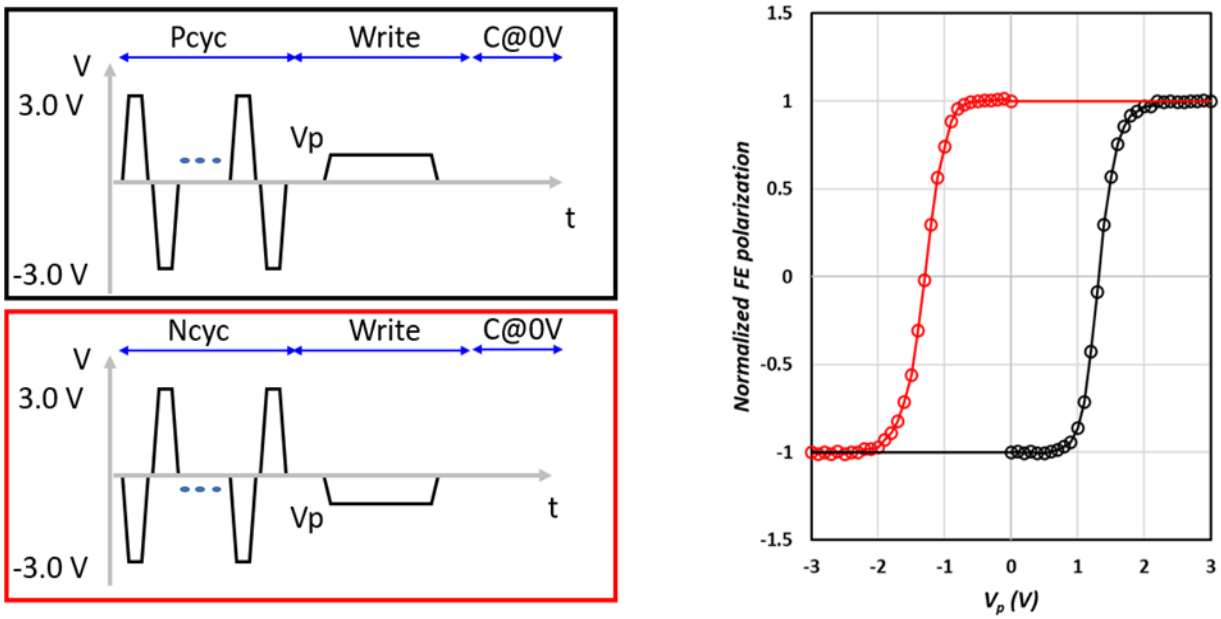

Fig. 5-21. Schematic of small-signal capacitance measurement at different FE polarization states (left). Top (after Pcyc) and bottom (after Ncyc) schemes are used to observe both FE switching direction from different presets. Measured normalized P vs. V_p according to V_p of write pulses (right).

Fig. 5-21 shows a schematic of the small-signal measurement at different FE polarization states. After Pcyc (or Ncyc), a MFM capacitor is set to a certain FE state by a write pulse, which is a trapezoidal voltage pulse with a pulse amplitude V_p and width of 1 μs with 40 ns rise/fall time. Before starting the measurement, we confirmed V_p-dependent FE polarization states by measuring a typical P-V hysteresis loop using different write pulses (right). According to the DW theory [50, 62], the measured pure ac capacitance (C_p @0V) vs. normalized FE polarization characteristics should show the same shape as the data from typical small-signal C-V characteristics across the bias range.

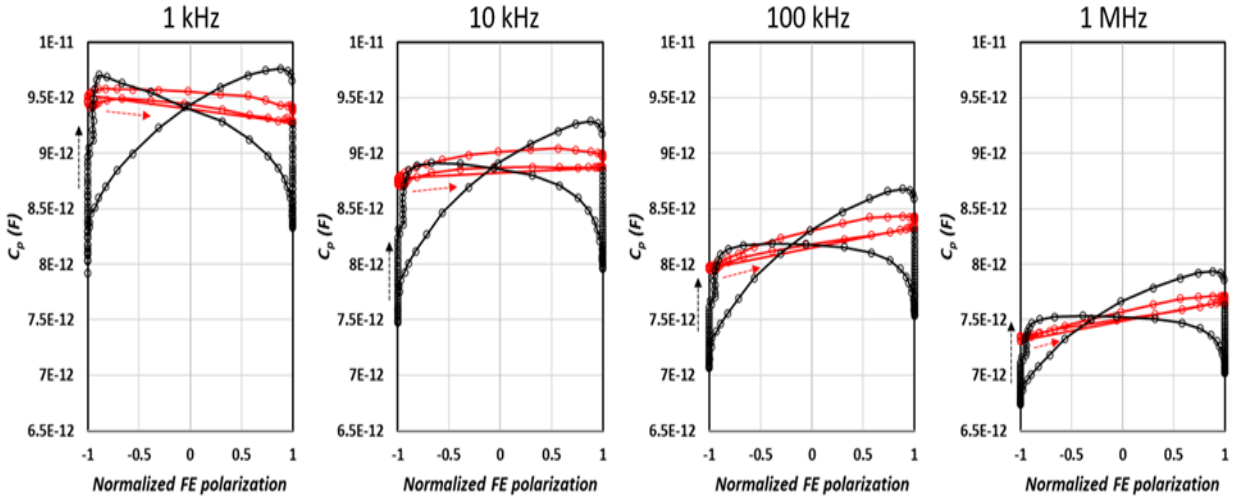

Fig. 5-22. Comparison C_p vs. normalized P between C_p@0V (red, pure ac C_p) and C_p from standard C-V measurments (black, with DC bias effects) at different frequencies.

Fig. 5-22 depicts the comparison of C_p vs. normalized FE polarization characteristics between pure ac C_p at 0 V measured as described in the previous paragraph and C_p from standard C-V characteristics at different frequencies. In contrast to the suggested DW theory, the two sets of data not only exhibit different dependencies on FE polarization but also display different C_p values. The C_p data derived from C-V curves shows two peaks in capacitance at a normalized FE polarization of 0.8, and C_p tunability ranging from 16% to 19%. On the other hand, the pure ac C_p

at 0 V has no peaks and a smaller C_p tunability ranging from 3% to 6% is obtained. Close to 0 V, all data sets tend to converge.

Since the FE domain structure at 0 V is expected to be very different with the device polarized in different states, these experiments reveal that the butterfly shape observed in the standard small-signal C-V characteristics is not likely to be a result of DW vibrations. Instead, it arises from a combination of physics related to FE switching and the effects of DC bias.

5.5.2 Modeling of Butterfly Shape C-V Curve

In the previous section, we have demonstrated that FE domain wall vibration is not related to the butterfly shaped C-V curve. We postulate that the butterfly behavior of C_{int} arises from the existence of thin interfacial layers at the metal-HZO boundaries that are in good electrical contact with the metal, i.e., two series capacitances of C_{fe} and C_{if}. In a process akin to poly-Si depletion in poly-Si gate MOSFETs, the charge in the metal plates of the MFM structure is accommodated through electron depletion or accumulation at these interfacial layers. The butterfly shape emerges if the interface capacitance is *inversely proportional to the charge at the metal plate*, as in poly-Si depletion. Correctly modeling this requires handling the contributions of upward and downward polarized domains separately and adding the respective capacitances which are in parallel, as illustrated in Fig. 5-23.

When V = -3 V, all domains have upward polarization (Fig. 5-23 left). In addition to that, the charges from the paraelectric response are added to the FE polarization with the same polarity. Accordingly, the maximum total |Q| at the metal surface is formed, leading to the maximum

thickness of the depletion layer. In other words, the total capacitance is at the minimum in the C-V curve (Fig. 5-23 right). As negative voltage decreases, the depletion layer thickness gradually reduces due to the linear decrease of absolute paraelectric charge. This behavior explains the capacitance increase with DC bias. Then, the thickness reaches the minimum point at $V = V_{SW}$ as the minimum total |Q| appears. This point corresponds to the peak capacitance in the C-V curve.

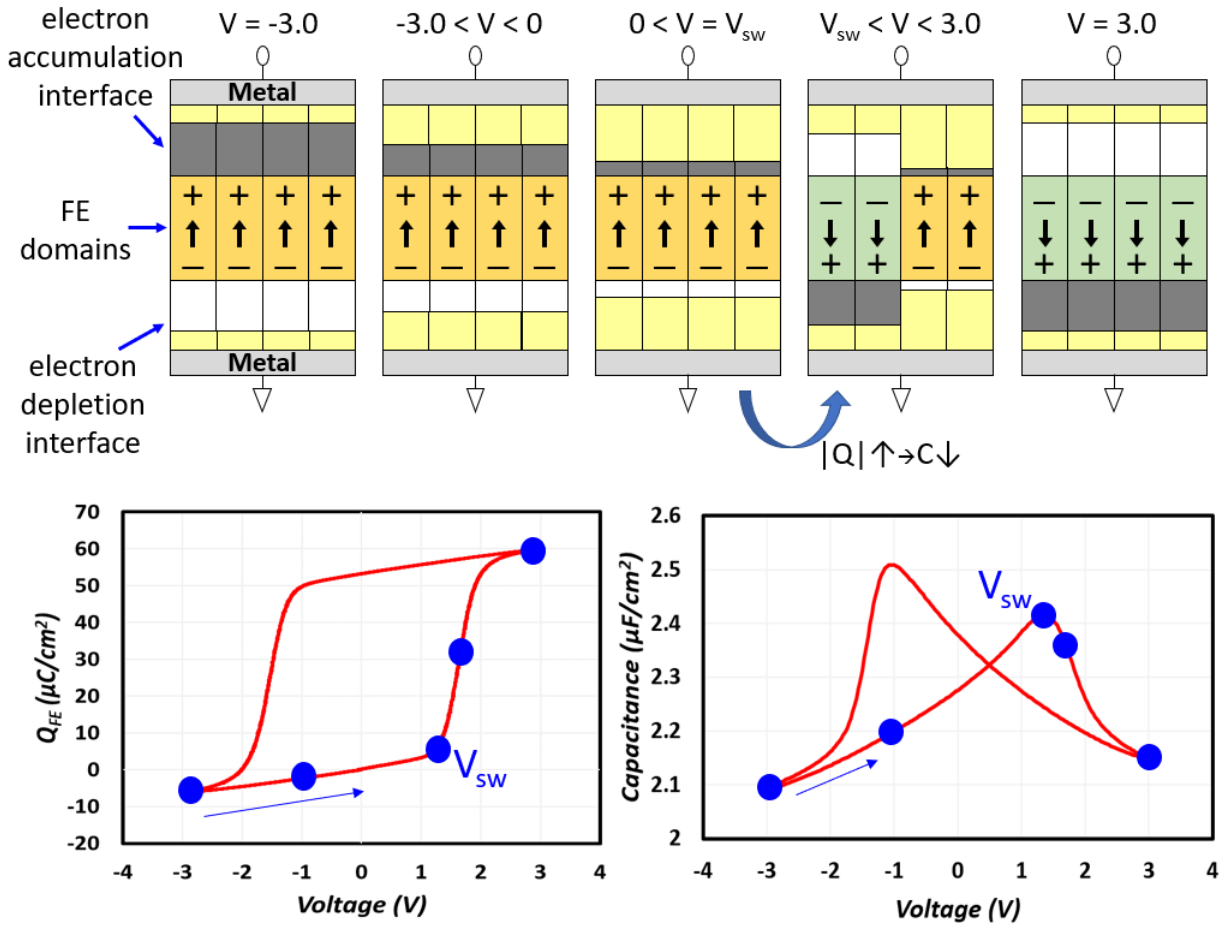

Fig. 5-23. Illustration of electron depletion and accumulation at W/HZO interface layers depending on FE domain polarization sign at a certain V corresponding to different points in Q-V loop and C-V curve.

From here on, as V increases passed V_{sw} FE domains start to switch. The absolute charge on the metal plates associated with each domain increases as the domains flip and the capacitance

associated with this domain decreases. In consequence, the overall capacitance, which is the sum of the capacitance associated with each domain, drops with voltage. Here, the slope of the capacitance reduction when $V > V_{SW}$ is steeper than that of the gradual increase when $-3\ V < V < V_{SW}$ because the FE domain switching causes a rapid change of |Q|. Finally, after all domains are flipped, this slope becomes comparable to the slope observed in negative voltage region and the capacitance reaches the minimum point when V = 3 V the higher end of our measurement range.

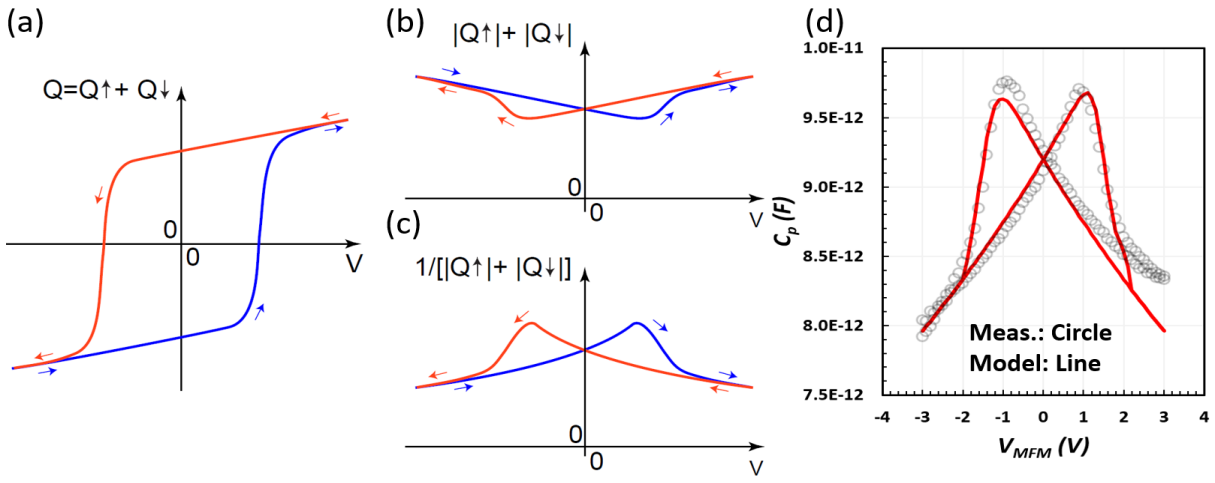

Fig. 5-24. (a)-(c) Principle of butterfly-shaped C_{int} vs. V_{MFM} curve. Charge-Voltage characteristics constructing a butterfly shape by handling the contributions of P_{up} and P_{down} domains separately. (d) Quantitative comparison of C_p vs. V_{MFM} between measurement (circle) and new butterfly model (line).

This model quantitatively describes well the butterfly shape of C_{int} in our devices, as shown in Fig. 5-24. Fig. 5-24 (a) represents the Q-V characteristics of a typical MFM structure. Fig. 5-24 (b) diagram represents the |Q|-V characteristics mapping separately up domains and down domains. Finally, Fig. 5-24 (c) represents 1/|Q|-V characteristics. Starting with the structure polarized in the downward direction (bottom left corner of Fig. 5-24 (a), blue line), as voltage increases from negative to positive values, |Q| in the plates decreases due to the dielectric (non-FE) capacitance

of HZO. As a result, 1/|Q| increases and so does the interfacial capacitance. As voltage approaches the coercive voltage and polarization switching starts, a large amount of charge is deposited on the plates, |Q| increases, 1/|Q| decreases and so does the interfacial capacitance. This process slows down when domain switching is complete and further increases in |Q| and reductions in 1/|Q| take place only through the dielectric nature of the HZO.

The model shows a great match with our measurements. Based on the measured Q_{FE}-V_{MFM} loop and interface capacitance, the butterfly-shaped C-V curve is constructed, as shown in Fig. 5-24 (d). The extracted interface capacitance of 18 μC/cm^2 from the data set of 1/C vs. HZO thickness was applied to the model as interfacial layer capacitance when depletion thickness is at minimum. This value is consistent with the range of data in [49].

The key model assumption is the existence of semiconductor-like interfacial layers in good electrical communication with the metal, hence the lack of frequency dependence. As W easily oxidizes to WO_x [64], a semiconducting metal oxide could be present at the W/HZO interface. Alternately, the interfacial layer could have as origin the finite electronic screening length of the metal which allows electric field penetration into it [49], as mentioned in Chapter 4. In both cases, our model can reproduce a butterfly-shaped C-V curve.

5.6 Summary

In this chapter, we have presented impedance vs. frequency characteristics at different DC bias points across a wide range of frequencies, from 1 kHz to 20 GHz, using accurately calibrated setups. Based on the data, we have developed a new small-signal equivalent circuit model. The

model has been built using mathematical expressions and performs well with respect to the measurements.

Then, the circuit elements, R_p and C_p, have been investigated to reveal the underlying physics of their frequency dependence. We have found that the observed frequency-dependent R_p can be explained by the CBH model after converting to σ_{ac} vs. frequency characteristics. The frequency-dependent C_p is attributed to electron trapping in border traps in the dielectric similar to the case of HfO_2/metal-gate InGaAs MOSFETs.

Furthermore, the origin of butterfly-shaped C-V characteristics of MFM capacitors have been explored. In contrast with the literature, using the pure AC capacitance measured at 0 V DC of a sample prepared at different polarization states, we have found that the shape cannot be explained by domain wall vibrations. Instead, a voltage-dependent interfacial layer capacitance model is appropriate to comprehend the voltage dependence of MFM capacitors.

Chapter 6 Conclusions and Suggestions

6.1 Conclusions

This thesis represents a comprehensive and significant contribution to the understanding of switching dynamics in FE-HZO structures. Particularly, the study is valuable in that it has analyzed FE switching dynamics in both the large- and small-signal domains.

In large-signal analysis and modeling, we meticulously characterized the MFM structures using precisely calibrated measurement setups. Notably, our results revealed that R-MFM circuits have no evidence of NC-like behavior under a broad range of conditions, contrary to what was reported in the literature. Building upon these accurate observations, we have developed the FD-NLS model by thoroughly reformulating the fundamental NLS equation. This model enables efficient FE circuit simulations with arbitrary electric field waveforms and shows excellent agreement with all experimental data, incorporating a crucial new feature - the paused incubation time relaxation model.

Additionally, the imprint effect, a serious degradation factor in FE materials, has been investigated in HZO by employing various pulse measurements. As a result, we have found discrepancies with previously proposed models, emphasizing the need for a fresh perspective on this phenomenon.

In the small-signal analysis and modeling, we have demonstrated de-embedded Z characteristics of FE-HZO MFM structures spanning from 1 kHz to 10 GHz. Furthermore, we have developed a physically meaningful equivalent circuit model that accurately describes the data across the entire frequency range and bias range. This approach has provided insights into the underlying physics

of circuit elements, which had not been previously addressed in the existing literature. In particular, we have proposed a model for the frequency dependence of capacitance and its butterfly shape which has been found to persist to the highest frequencies.

6.2 Suggestions for Future Research

In this thesis, we have thoroughly examined the dynamics of FE-HZO structures through both large-signal analysis and small-signal analysis. The models we have developed, founded on fundamental understanding, have demonstrated remarkable predictive capabilities across a wide range of conditions. However, there are further studies that are needed to deepen our comprehension of the relevant physics and strengthen the models. These include:

- Observation of large-signal FE switching dynamics in picosecond range to reach FE switching limit
- Understanding of underlying physics of paused incubation-time relaxation model in FD-NLS model
- Developing a model for imprint effect and incorporating into FD-NLS model
- Process engineering for improvement of imprint effect
- Investigation of interfacial layer between metal and oxide for C_{int} model
- AC characteristics in the GHz regime at different temperatures
- Studying impact of electrode material and HZO process conditions and quality on FE dynamics
- Connecting and constructing a unified model for large-signal and small-signal dynamics.

Bibliography

[1] J. F. Ihlefeld, "Chapter 1. Fundamentals of Ferroelectric and Piezoelectric Properties," in *Ferroelectricity in Doped Hafnium Oxide: Materials, Properties and Devices*, Elsevier Ltd., 2019, p. 2.

[2] I. Ross, "Semiconductive translating device". U.S. Patent US2791760A, 7 May 1957.

[3] D. Bondurant, "Ferroelectric RAM memory family for critical data storage," *Ferroelectrics*, vol. 112, pp. 273-282, 1990.

[4] T. S. Böscke, J. Müller, D. Bräuhaus, U. Schröder and U. Böttger, "Ferroelectricity in hafnium oxide thin films," *Applied Physics Letters*, vol. 99, no. 10, p. 102903, 2011.

[5] J. Müller, T. S. Böscke, U. Schröder, S. Mueller, D. Bräuhaus, U. Böttger, L. Frey and T. Mikolajick, "Ferroelectricity in simple binary ZrO2 and HfO2," *Nano Letters*, vol. 12, no. 8, p. 4318–4323, 2012.

[6] Z. Krivokapic, U. Rana, R. Galatage, A. Razavieh, A. Aziz, J. Liu, J. Shi, H. Kim, R. Sporer, C. Serrao, A. Busquet, P. Polakowski, J. Muller, W. Kleemeier, A. Jacob, D. Brown, A. Knorr, R. Carter and S. Banna, "14nm Ferroelectric FinFET technology with steep subthreshold slope for ultra low power applications," in *2017 IEEE International Electron Devices Meeting (IEDM)*, San Francisco, CA, USA, 2017.

[7] T. S. Böscke, J. Müller, D. Bräuhaus, U. Schröder and U. Böttger, "Ferroelectricity in hafnium oxide: CMOS compatible ferroelectric field effect transistors," in *2011 International Electron Devices Meeting*, San Fransisco, CA, USA, 2011.

[8] K. Chen, H. Chen, C. Liao, G. Siang, C. Lo, M. Liao, K. Li, S. Chang and M. Lee, "Non-Volatile Ferroelectric FETs Using 5-nm Hf0.5Zr0.5O2 With High Data Retention and Read Endurance for 1T Memory Applications," *IEEE Electron Device Letters*, vol. 40, no. 3, pp. 399-402, 2019.

[9] S. Oh, T. Kim, M. Kwak, J. Song, J. Woo, S. Jeon, I. Yoo and H. Hwang, "HfZrOx-Based Ferroelectric Synapse Device With 32 Levels of Conductance States for Neuromorphic Applications," *IEEE Electron Device Letters*, vol. 38, no. 6, pp. 732-735, 2017.

[10] M. Jerry, P. -Y. Chen, J. Zhang, P. Sharma, K. Ni, S. Yu and S. Datta, "Ferroelectric FET analog synapse for acceleration of deep neural network training," in *2017 IEEE International Electron Devices Meeting (IEDM)*, San Fransisco, CA, USA, 2017.

[11] M.-K. Kim and J.-S. Lee, "Ferroelectric analog synaptic transistors," *Nano Letters*, vol. 19, no. 3, p. 2044–2050, 2019.

[12] S. Abdulazhanov, Q. H. Le, D. K. Huynh, D. Wang, D. Lehninger, T. Kämpfe and G. Gerlach, "THz Thin Film Varactor Based on Integrated Ferroelectric HfZrO2," *ACS Appl. Electron. Mater.*, vol. 5, no. 1, pp. 189-195, 2023.

[13] T. Mikolajick, S. Slesazeck, H. Mulaosmanovic, M. H. Park, S. Fichtner, P. D. Lomenzo, M. Hoffmann and U. Schroeder, "Next generation ferroelectric materials for semiconductor process integration and their applications," *Journal of Applied Physics*, vol. 129, p. 100901, 2021.

[14] S. Hashimoto, H. Orihara and Y. Ishibashi, "Study on D-E hysteresis loop of TGS based on the Avrami-type model," *J. Phys. Soc. Jpn.*, vol. 63, no. 4, pp. 1601-1610, 1994.

[15] A. N. Kolmogorov, "On the statistical theory of the crystallization of metals," *Izvestiya Akademii Nauk Ser. Math.,* vol. 1, no. 3, pp. 355-359, 1937.

[16] M. Avrami, "Kinetics of phase change. I General theory," *J. Chem. Phys.,* vol. 7, no. 12, pp. 1103-1112, 1939.

[17] A. K. Tagantsev, I. Stolichnov, J. S. C. N. Setter and M. Tsukada, "Non-Kolmogorov–Avrami switching kinetics in ferroelectric thin films," *Phys. Rev. B Condens. Matter.,* vol. 66, no. 21, Dec 2002.

[18] P. Buragohain, C. Richter, T. Schenk, H. Lu, T. Mikolajick, U. Schroeder and A. Gruverman, "Nanoscopic studies of domain structure dynamics in ferroelectric La:HfO2 capacitors," *Appl. Phys. Lett.,* vol. 112, no. 22, p. 222901, May 2018.

[19] S. Zhukov, Y. A. Genenko, O. Hirsch, J. Glaum, T. Granzow and H. v. Seggern, "Dynamics of polarization reversal in virgin and fatigued ferroelectric ceramics by inhomogeneous field mechanism," *Phys. Rev. B Condens. Matter,* vol. 82, no. 1, July 2010.

[20] J. Y. Jo, H. S. Han, J.-G. Yoon, T. K. Song, S.-H. Kim and T. W. Noh, "Domain switching kinetics in disordered ferroelectric thin films," *Phys. Rev. Lett.,* vol. 99, no. 26, Dec. 2007.

[21] C. Alessandri, P. Pandey, A. Abusleme and A. Seabaugh, "Switching dynamics of ferroelectric Zr-doped HfO 2," *IEEE Electron Device Lett.,* vol. 39, no. 11, pp. 1780-1783, Nov. 2018.

[22] Z. Liu, H. Jiang, B. Ordway and T. P. Ma, "Unveiling the apparent ‘negative capacitance’ effects resulting from pulse measurements of ferroelectric-dielectric bilayer capacitors," *IEEE Electron Device Lett.,* vol. 41, no. 10, pp. 1492-1495, Oct. 2020.

[23] C. -T. Tung, G. Pahwa, S. Salahuddin and C. Hu, "A Compact Model of Polycrystalline Ferroelectric Capacitor," *IEEE Transactions on Electron Devices,* vol. 68, no. 10, pp. 5311-5314, Oct. 2021.

[24] C. Alessandri, A. P. Pandey, Abusleme and A. Seabaugh, "Monte–Carlo simulation of switching dynamics in polycrystalline ferroelectric capacitors," *IEEE Trans. Electron Devices,* vol. 66, no. 8, pp. 3527-3534, 2019.

[25] P. Buragohain, A. Erickson, P. Kariuki, T. Mittmann, C. Richter, P. D. Lomenzo, H. Lu, T. Schenk, T. Mikolajick, U. Schroeder and A. Gruverman, "Fluid Imprint and Inertial Switching in Ferroelectric La:HfO2 Capacitors," *ACS Appl. Mater. Interfaces,* vol. 11, pp. 35115-35121, 2019.

[26] K. Takada, S. Takarae, K. Shimamoto, N. Fujimura and T. Yoshimura, "Time-dependent imprint in Hf0.5Zr0.5O2 ferroelectric thin films," *Adv. Electron. Mater.,* vol. 7, p. 2100151, 2021.

[27] C. Zacharaki, P. Tsipas, S. Chaitoglou, L. Bégon-Lours, M. Halter and A. Dimoulas, "Reliability aspects of ferroelectric TiN/Hf0.5Zr0.5O2/Ge capacitors grown by plasma assisted atomic oxygen deposition," *Appl. Phys. Lett.,* vol. 117, p. 212905, 2020.

[28] A. G. Chernikova and A. M. Markeev, "Dynamic imprint recovery as an origin of the pulse width dependence of retention in Hf0.5Zr0.5O2-based capacitors," *Appl. Phys. Lett.,* vol. 119, p. 032904, 2021.

[29] A. K. Tagantsev, I. Stolichnov, N. Setter and J. S. Cross, "Nature of nonlinear imprint in ferroelectric films and long-term prediction of polarization loss in ferroelectric memories," *Journal of Applied Physics,* vol. 96, pp. 6616-6623, 2004.

[30] P. Yuan, G.-Q. Mao, Y. Cheng, K.-H. Xue, Y. Zheng, Y. Yang, P. Jiang, Y. Xu, Y. Wang, Y. Wang, Y. Ding, Y. Chen, Z. Dang, L. Tai, T. Gong, Q. Luo, X. Miao and Q. Liu, "Microscopic mechanism of imprint in hafnium oxide-based ferroelectrics," *Nano Research,* vol. 15, pp. 3667-3674, 2022.

[31] F. P. G. Fengler, M. Hoffmann, S. Slesazeck, T. Mikolajick and U. Schroeder, "On the relationship between field cycling and imprint in ferroelectric Hf 0.5 Zr 0.5 O_2," *J. Appl. Phys.,* vol. 123, no. 20, 2018.

[32] G. Arlt and H. Neumann, "Internal bias in ferroelectric ceramics: Origin and time dependence," *Ferroelectrics,* vol. 87, no. 1, pp. 109-120, 1988.

[33] M. Grossmann, O. Lohse, D. Bolten, U. Boettger and R. Waser, "The interface screening model as origin of imprint in PbZrxTi1−xO3 thin films. II. Numerical simulation and verification," *Journal of Applied Physics,* vol. 92, no. 5, pp. 2688-2696, 2002.

[34] Y. Higashi, B. Kaczer, A. S. Verhulst, B. J. O'Sullivan, N. Ronchi, S. R. C. McMitchell, K. Banerjee, L. D. Piazza, M. Suzuki, D. Linten and J. V. Houdt, "Investigation of Imprint in FE-HfO_2 and Its Recovery," *IEEE Transactions on Electron Devices,* vol. 67, no. 11, pp. 4911-4917, 2020.

[35] A. K. Tagantsev and G. Gerra, "Interface-induced phenomena in polarization response of ferroelectric thin films," *Journal of Applied Physics ,* vol. 100, p. 051607, 2006.

[36] M. Aldrigo, M. Dragoman, S. Iordanescu, F. Nastase, S. Vulpe, A. Dinescsu and D. Vasilache, "Low-Voltage Permittivity Control of Coplanar Lines Based on Hafnium Oxide Ferroelectrics Grown on Silicon," *IEEE Access,* vol. 7, pp. 136686-136693, 2019.

[37] S. Han, C. Lee, H. Shin, J. Lee and H. Cha, "Investigation of frequency-dependent permittivity tenability of P(VDF−TrFE) metal-ferroelectric-metal capacitor," *Results Phys.* , vol. 12, p. 469–470, 2019.

[38] M. Shao, T. Lu, Z. Wang, H. Liu, R. Zhao, X. Liu, X. Zhao, R. Liang, Y. Yang and T.-L. Ren, "Interfacial Regulation of Dielectric Properties in Ferroelectric Hf0.5Zr0.5O2 Thin Films," *IEEE Journal of the Electron Devices Society,* vol. 9, pp. 1093-1097, 2021.

[39] E. D. Grimley, T. Schenk, X. Sang, M. Pešić, U. Schroeder, T. Mikolajick and J. M. LeBeau, "Structural Changes Underlying Field-Cycling Phenomena in Ferroelectric HfO2 Thin Films," *Advanced Electronic Materials,* vol. 2, no. 9, p. 1600173, 2016.

[40] S. Oh, T. Kim, M. Kwak, J. Song, J. Woo, S. Jeon, I. K. Yoo and H. Hwang, "HfZrOx-Based Ferroelectric Synapse Device With 32 Levels of Conductance States for Neuromorphic Applications," *IEEE Electron Device Letters,* vol. 38, no. 6, pp. 732-735, June 2017.

[41] A. I. Khan, "Negative capacitance in a ferroelectric capacitor," *Nature Materials,* vol. 14, no. 2, pp. 182-186, 2015.

[42] M. Hoffmann, M. Pešić, K. Chatterjee, A. I. Khan, S. Salahuddin, S. Slesazeck, U. Schroeder and M. Thomas, "Direct Observation of Negative Capacitance in Polycrystalline Ferroelectric HfO2," *Advanced Functional Materials,* vol. 14, no. 2, pp. 182-186, 2015.

[43] P. Sharma, J. Zhang, K. Ni and S. Datta, "Time-Resolved Measurement of Negative Capacitance," *," in IEEE Electron Device Letters,* vol. 39, no. 2, pp. 272-275, 2018.

[44] M. Kobayashi, N. Ueyama, K. Jang and T. Hiramoto, "Experimental study on polarization-limited operation speed of negative capacitance FET with ferroelectric HfO2," in *2016*

IEEE International Electron Devices Meeting (IEDM), San Francisco, CA, USA, 2016, pp. 12.3.1-12.3.4.

[45] K. Jang, N. Ueyama, M. Kobayashi and T. Hiramoto, "Experimental Observation and Simulation Model for Transient Characteristics of Negative-Capacitance in Ferroelectric HfZrO2 Capacitor," *IEEE Journal of the Electron Devices Society*, vol. 6, pp. 346-353, 2018.

[46] Y. Li, J. Li, R. Liang, R. Zhao, B. Xiong, H. Liu, H. Tian, Y. Yang and T.-L. Ren, "Switching dynamics of ferroelectric HfO2-ZrO2 with various ZrO2 contents," *Appl. Phys. Lett.*, vol. 114, no. 14, p. 142902, April 2019.

[47] H. Orihara, S. Hashimoto and Y. Ishibashi, "A theory of DE hysteresis loop based on the Avrami model," *J. Phys. Soc. Jpn.*, vol. 63, no. 3, pp. 1031-1035, 1994.

[48] H. Mulaosmanovic, et and al., "Investigation of accumulative switching in ferroelectric FETs: Enabling universal modeling of the switching behavior," *IEEE Trans. Electron Devices*, vol. 67, no. 12, pp. 5804-5809, Dec 2020.

[49] C. T. Black and Jeffrey J. Welser, "Electric-Field Penetration Into Metals: Consequences for High-Dielectric-Constant Capacitors," *IEEE TRANSACTIONS ON ELECTRON DEVICES*, vol. 46, no. 4, pp. 776-780, 1999.

[50] F. P. G. Fengler, M. Pešić, S. Starschich, T. Schneller, C. Künneth, U. Böttger, H. Mulaosmanovic, T. Schenk, M. H. Park, R. Nigon, P. Muralt, T. Mikolajick and U. Schroeder, "Domain Pinning: Comparison of Hafnia and PZT Based Ferroelectrics," *Advanced Electronic Materials*, vol. 3, no. 4, p. 1600505, 2017.

[51] U. Boettger, D. Braeuhaus and R. Waser, "The influence of non-ferroelectric interface layers and inclusions on the imprint behavior of ferroelectric thin film capacitors," in *2007 Sixteenth IEEE International Symposium on the Applications of Ferroelectrics*, Nara, Japan, 2007.

[52] S. Abdulazhanov, Q. Le, D. Huynh, D. Wang, M. Lederer, R. Olivo, K. Mertens, J. Emara, T. Kämpfe and G. Gerlach, "RF-Characterization of HZO Thin Film Varactors," *Crystals*, vol. 11, p. 980, 2021.

[53] A. K. Jonscher, "The 'universal' dielectric response," *Nature*, vol. 267, pp. 673-679, June 1977.

[54] S. R. Elliott, "A.c. conduction in amorphous chalcogenide and pnictide semiconductors," *Advances in Physics*, vol. 36, no. 2, pp. 135-218, 1987.

[55] S. R. Elliott, "A theory of a.c. conduction in chalcogenide glasses," *Philosophical Magazine*, vol. 36, no. 6, pp. 1291-1304, 1977.

[56] S. Kumar and K. Varma, "Structural and dielectric properties of Bi4Ti2Nb0.5Fe0.5O12 ceramics," *Solid State Communications*, vol. 146, no. 3-4, pp. 137-142, 2008.

[57] L. Larcher, F. M. Puglisi, P. Pavan, A. Padovani, L. Vandelli and G. Bersuker, "A Compact Model of Program Window in HfOx RRAM Devices for Conductive Filament Characteristics Analysis," *IEEE Transactions on Electron Devices*, vol. 61, no. 8, pp. 2668-2673, 2014.

[58] H. Nakamura and Y. Asai, "Competitive effects of oxygen vacancy formation and interfacial oxidation on an ultra-thin HfO2-based resistive switching memory: beyond

filament and charge hopping models," *Phys. Chem. Chem. Phys.*, vol. 18, pp. 8820-8826, 2016.

[59] D. J. J. Loy, P. A. Dananjaya, S. Chakrabarti, K. H. Tan, S. C. W. Chow, E. H. Toh and W. S. Lew, "Oxygen Vacancy Density Dependence with a Hopping Conduction Mechanism in Multilevel Switching Behavior of HfO2-Based Resistive Random Access Memory Devices," *ACS Appl. Electron. Mater.*, vol. 2, pp. 3160-3170, 2020.

[60] A. K. Jonscher, "Dielectric relaxation in solids," *J. Phys. D: Appl. Phys.*, vol. 32, pp. R57-R70, 1999.

[61] X. Cai, A. Vardi, J. Grajal and J. A. d. Alamo, "A New Technique for Mobility Extraction in MOSFETs in the Presence of Prominent Gate Oxide Trapping: Application to InGaAs MOSFETs," *IEEE Transactions on Electron Devices*, vol. 67, no. 8, pp. 3075-3081, 2020.

[62] M. Pešić, F. P. G. Fengler, L. Larcher, A. Padovani, T. Schenk, E. D. Grimley, X. Sang, J. M. LeBeau, S. Slesazeck, U. Schroeder and T. Mikolajick, "Physical Mechanisms behind the Field-Cycling Behavior of HfO2-Based Ferroelectric Capacitors," *Advanced Functional Materials*, vol. 26, no. 25, pp. 4601-4612, 2016.

[63] S. Deng, Z. Jiang, S. Dutta, H. Ye, W. Chakraborty, S. Kurinec, S. Datta and K. Ni, "Examination of the Interplay Between Polarization Switching and Charge Trapping in Ferroelectric FET," in *2020 IEEE International Electron Devices Meeting (IEDM)*, San Francisco, CA, USA,, 2020.

[64] A. Kashir, H. Kim, S. Oh and H. Hwang, "Large Remnant Polarization in a Wake-Up Free Hf0.5Zr0.5O2 Ferroelectric Film through Bulk and Interface Engineering," *ACS Applied Electronic Materials*, vol. 3, no. 2, pp. 629-638, 2021.

[65] T. Kim, J. A. del Alamo and D. A. Antoniadis, "Dynamics of HfZrO2 ferroelectric structures: Experiments and models," in *2020 IEEE International Electron Devices Meeting (IEDM)*, Sanfransisco, CA, USA, Dec. 2020, pp. 21.4.1-21.4.4.

[66] Y. Zheng, Y. Zheng, Z. Gao, J.-H. Yuan, Y. Cheng, Q. Zhong, T. Xin, Y. Wang, C. Liu, Y. Huang, R. Huang, X. Miao, K.-H. Xue and H. Lyu, "Atomic-scale characterization of defects generation during fatigue in ferroelectric Hf0.5Zr0.5O2 films: vacancy generation and lattice dislocation," in *IEEE International Electron Devices Meeting (IEDM)*, San Francisco, CA, USA, 2021.

[67] W. Hamouda, A. Pancotti and C. Lubin, "Physical chemistry of the TiN/Hf0.5Zr0.5O2," *Journal of Applied Physics*, vol. 127, p. 064105, 2020.

[68] W. Hu, Y. Liu, R. L. Withers, T. J. Frankcombe, L. Norén, A. Snashall, M. Kitchin, P. Smith, B. Gong, H. Chen, J. Schiemer, F. Brink and J. Wong-Leung, "Electron-pinned defect-dipoles for high-performance colossal permittivity materials," *Nature Materials*, vol. 12, pp. 821-826, 2013.

Appendix A

The NLS equations can be solved numerically by various algorithms. Following are the key elements of the algorithm that we implmented here to solve the core NLS model equations via finite difference method.

FD-NLS $P(t_i)$ Solution Algorithm

Initialize P_g vector of size of vector η : $P_g(:, t_1) = P(t = 0)$

Solve for P at time $t=t_i$.

$$s_i = sign[E(t_i) - E_{off}]$$

$$\tau_i = \tau_0 e^{\left(\frac{\eta E_a}{|E(t_i) - E_{off}|}\right)^{\alpha}}$$

$$\tau_{gs,i} = \frac{\tau_i^{\beta}}{\beta T_{inc,i-1}^{\beta-1}}$$

$$P_g(\eta, t_i) = P_g(\eta, t_{i-1}) + s_i P_s \frac{1}{1 + \frac{\tau_{gs,i}}{dt_i}}$$

$$P(t_i) = \int_0^{\infty} P_g(\eta, t_i) f(\eta) d\eta$$

Update T_{inc}: To be used in the next time increment

$T_{inc,i} = T_{inc,i-1} + (t_i - t_{i-1})$

if $|P(t_i) - P(t_{i-1})|/P_S < \epsilon$: identify paused P

if $|P(t_{i-1}) - P(t_{i-2})|/P_S > \epsilon$: identify first pause

$t_p = t_i$

$T_{inc,pause} = T_{inc,i-1}$

end if

$T_{inc,i} = \gamma(t_i - t_p) T_{inc,pause}$: Relax T_{inc} if paused P

end if

End of calculation for $t=t_i$. Increment $i=i+1$ and repeat

The numetical solution for equation (3-9) for $P_g(\eta,t)$, i.e., the 4th equation above, is via the backward Euler method. Also, ϵ is an empirical small scalar, e.g. 10^{-12} that defines the threshold of normalized paused-polarization change. Defining paused-polarization this way avoids subtle but incorrectly different solutions between pulses with V_{min}=0 and $|V_{min}|$=vanishingly-small. The discrete solution of eqs (3-12), (3-13), and (3-14) is rather obvious and not shown explicitly.

Note that the incubation time in the above algorithm is updated after $P(t_i)$, the polarization density at the *ith* time increment is calculated, and therefore it lags by one time step in the calculation of $\tau_{gs,i}$. This can be ameliorated with a different discretization method, but for small enough time increments the difference in negligible.

This algorithm was implemented in a simple finite-difference circuit solver, written in Matlab, in order to simulate the simple circuits involved in FE capacitor characterization experiments (e.g. [65]). At this point, we have not implemented the algorithm in any standard circuit simulator.

Appendix B

In principle, fitting the NLS model parameters to a particular FE capacitor structure requires a set of measurements of polarization reversal vs. time of sample capacitors subjected to voltage steps from 0 to $\pm|V_0+\Delta V|$ with increasing ΔV, where the + sign is for $-P_S$, and – for $+P_S$ pre-polling as shown in [19] and [21]. Then, first, the probability density function, $f(\eta)$, is determined paralleling the methodology described in those papers, from the $P(t)$ vs. log(t) data which extracts the so-called *master curve,* $\Phi(E/E_{max})$,

$$\Phi\left(\frac{E}{E_{max}}\right) = \frac{d\Delta P}{dE}\frac{E}{2P_s} \quad \text{(B1)}$$

where E is the applied electric field, $|V_0+\Delta V|/t_{FE}$, with t_{FE} the film thickness, and E_{max} is the value of E where the r.h.s. of equation (B1) is maximal at any given time, t. In our particular implementation of the NLS model, with the random variable η randomizing E_a we have $\eta \approx E/E_{max}$. An analytical probability density function, PDF, $f(\eta)$ is then fitted to the experimental master curve $\Phi(E/E_{max})$. Different PDFs can be chosen at this point. For example, in [21] the authors fitted the data very well with a PDF form of Beta function. As in [19] we have also found a Gaussian function fitting some experiments well, and in some other cases a high modulus Weibull function appears to work well. Whatever function is chosen for $f(\eta)$ the next step is the optimization of the NLS model parameters, τ_0, α, β, E_a, E_{off}. This can be done by fitting the above $P(t)$ vs. E data via any standard optimization method. Since the experimental data all come from single-step voltage drives the parameters, τ_p, *and* k_p are irrelevant at this point. Finally, those two parameters can be fitted with variable duty-cycle pulse drives, as described later in this Section. However, there can be cases where the appropriate multiple-voltage/multi-duty-cycle data, described above, are not

available. In those cases, we have found it still possible to arrive at a unique set of $f(\eta)$ and the other NLS parameters with experienced patient hand optimization using standard triangular-waveform P-V experiments at multiple frequencies. While the overall parameter set may not be as accurate as could be with the formal optimization, key conclusions about the dynamics of the particular FE film can still be safely drawn.